CONTRIBUTION TO THE STUDY OF NONSTATIONARY AERODYNAMIC FORCES IN PROBLEMS OF INTEREST FOR MICRO-AIR VEHICLES

ANTONIO MARTÍN ALCÁNTARA

UNIVERSIDAD
DE MÁLAGA

AUTOR: Antonio Martín Alcántara

iD   http://orcid.org/0000-0002-0311-1510

Esta Tesis Doctoral está depositada en el Repositorio Institucional de la Universidad de
Málaga (RIUMA): riuma.uma.es

CONTRIBUTION TO THE STUDY OF NONSTATIONARY AERODYNAMIC FORCES IN PROBLEMS OF INTEREST FOR MICRO-AIR VEHICLES

ANTONIO MARTÍN ALCÁNTARA

UNIVERSIDAD
DE MÁLAGA

PhD Thesis

PhD Program: Mechatronic Engineering
Dpto. de Ingeniería Mecánica, Térmica y de Fluidos
Escuela Técnica Superior de Ingeniería Industrial

Universidad de Málaga

SUPERVISORS:
Ramón Fernández Feria
Enrique Sanmiguel Rojas

Málaga, 2016

UNIVERSIDAD
DE MÁLAGA

Los profesores Dr. Ramón Fernández Feria y Dr. Enrique Sanmiguel Rojas, Catedrático de Universidad en el Dpto. de Ingeniería Mecánica, Térmica y de Fluidos de la Universidad de Málaga, y Profesor Titular de Universidad del Dpto. de Ingeniería Mecánica y Minera de la Universidad de Jaén, respectivamente.

CERTIFICAN:

Que D. Antonio Martín Alcántara, alumno de doctorado de la Universidad de Málaga, ha realizado bajo su dirección la presente tesis doctoral titulada *Contribution to the study of nonstationary aerodynamic forces in problems of interest for Micro-Air Vehicles*, cumpliendo todos los requisitos necesarios para optar al grado Doctor Internacional, por lo que ambos AUTORIZAN SU LECTURA Y DEFENSA PÚBLICA.

Dr. Ramón Fernández Feria

Dr. Enrique Sanmiguel Rojas

A la memoria de mis padres.

To the memory of my parents.

Difficulties strengthen the mind,
as labor does the body.

Las dificultades fortalecen la mente,
así como el trabajo lo hace con el cuerpo.

— **Lucius Annæus Seneca**
[c. 4 BC, Corduba, Spain – AD 65, Rome]

AGRADECIMIENTOS

Esta es sin duda la parte más difícil de la tesis. Significa mirar atrás antes de poner fin a esta estapa y al cambio que conlleva. Significa también darse cuenta de que sin la ayuda de muchas personas este documento no se habría podido llevar a cabo, y no sólo por razones científicas, sino por cuestiones personales, y esto último es imposible plasmarlo en ningún documento. Por ello, sólo puedo expresar en estas líneas mi gratitud a las personas clave que, de una forma u otra, son también parte de esta tesis.

En primer lugar me gustaría mostrar mi más profundo agradecimiento a mis directores de tesis, los profesores Ramón Fernández Feria y Enrique Sanmiguel Rojas. Ellos han sido de alguna manera una parte más de mi familia durante estos años. Les agradezco su confianza depositada a la hora de dirigir esta tesis, todos los conocimientos que me han transmitido, su paciencia, su dedicación incondicional y su calidad humana. De Enrique me quedo con todos esos cafés en Córdoba y con su dedicación para discutir problemas incluso en unas simples servilletas de papel (todavía conservo más de una). Te deseo todo lo mejor en tu nueva etapa. De Ramón me quedo con su enorme paciencia y su dedicación. Espero haber aprendido algo de los desarrollos teóricos que siempre hace parecer tan fáciles. Guardo muy buenos recuerdos de nues-tros ratos en Málaga. Sólo puedo decir que he trabajado en el "mejor equipo" y que sin su ayuda habría sido imposible llevar a cabo este trabajo.

Agradezco también a los profesores del grupo de Mecánica de Fluidos de la Universidad de Málaga su cercanía, ayuda y calidad humana desde antes incluso del comienzo de la tesis. Gracias a Carlos, Luis, Joaquín y José Francisco.

Agradezco a mi madre toda la atención, esfuerzo y cariño que invirtió en que llegara hasta aquí. Su memoria siempre me ha dado fuerzas para seguir adelante y su fortaleza humana ha sido y es un ejemplo a seguir para mí.

Quiero agradecer también a Estela su cariño y su apoyo durante estos años. Ella ha vivido de cerca mi pasión por lo que hacía en todo momento, y eso ha significado sacrificar muchos momentos especiales para ambos. La ilusión por la nueva etapa que juntos comenzamos ha sido definitiva para concluir esta tesis.

A mi hermana Pilar por ser tan servicial y apoyarme en estos años donde mi tiempo ha sido tan limitado y todo tan diferente.

A mis tíos Esteban y Ana por todo su cariño, su apoyo y su ánimo siempre que lo he necesitado.

A mis abuelos Andrés y Pilar que, además de abuelos, han sido unos padres para mí.

I would also like to thank the Prof. Robert Dudley for the short-term stay I could spend at UC Berkely. It has been an unforgettable experience in my life. Thank you and your family for all your help and your time when I was there, and for the great moments, including our last Jupiter and BBQ. Gracias al Dr. Víctor Ortega por todo lo aprendido trabajando con él en UC Berkeley, además de por el trato tan cálido que recibí tanto por su parte como por la de su familia y amigos mexicanos, ¡fue todo bien padre! No tengo palabras para vuestra amabilidad y buenos momentos juntos. I also thank all the people I met at the Animal Flight Laboratory for making me feel at home, specially, Sofía, Leeann, Ashley, Erik and Marc. I hope you keep alive Fridays afternoon. I wish you all the best in your lifes.

A la Universidad de Málaga por haberme permitido llevar a cabo las simulaciones en el Centro de Supercomputación Picasso. En particular quiero agradecer el soporte técnico prestado por Rafael Larrosa Jiménez y Darío Guerrero Fenández. Su atención y paciencia ha sido inmejorable.

Al Ministerio de Economía y Competitividad (Proyecto DPI2013-40479-P) y a la Junta de Andalucía (Proyecto P10-TEP-5702) por la financiación recibida durante el desarrollo de esta tesis.

Por último, quiero agradecer igualmente a todos aquellos que de alguna manera me han ayudado en este camino y que, por descuido o falta de espacio, no aparecen en estas líneas.

GRACIAS.

ABSTRACT

The main aim of this dissertation is the quantitative characterization of the contributions of individual fluid elements (vortices) to aerodynamic forces, explaining and quantifying the mechanisms by which both drag and lift are generated. For this purpose, a vorticity forces formulation was used to the two problems addressed in this thesis. Thus, a novel physical point of view of the flow dynamics is provided which is expected to be useful for the Micro-Air Vehicles (MAVs) design.

Firstly, the well-known *Magnus effect* problem is studied. In this problem, the two-dimensional flow past a spinning cylinder is investigated numerically using a vorticity forces formulation with the aim of analyzing quantitatively the flow structures, and their evolutions, that contribute to the lift and drag forces on the cylinder. The Reynolds number considered, based on the cylinder diameter and steady free stream speed, is $Re = 200$, while the non-dimensional rotation rate (ratio of the surface speed and free stream speed) selected was $\alpha = 1$ and 3. For $\alpha = 1$ the wake behind the cylinder for the fully developed flow is oscillatory due to vortex shedding, and so are the lift and drag forces. For $\alpha = 3$ the fully developed flow is steady with constant (high) lift and (low) drag. Each of these cases is considered in two different transient problems, one with angular acceleration of the cylinder and constant speed, and the other one with translating acceleration of the cylinder and constant rotation. We characterize quantitatively the contributions of individual fluid elements (vortices) to aerodynamic forces, explaining and quantifying the mechanisms by which the lift is generated in each case. In particular, for high rotation (when $\alpha = 3$), we explain the relation between the mechanisms of vortex shedding suppression and those by which the lift is enhanced and the drag is almost suppressed when the fully developed flow is reached.

On the other hand, the thrust efficiency of a two-dimensional flapping airfoil is studied computationally for a low Reynolds number via the same vortex force decomposition as the one cited previously. The auxiliary potentials that separate the total vortex force into lift and drag (or thrust) are obtained analytically by using an elliptic airfoil. With these auxiliary potentials, the added-mass components of the lift and drag (or thrust) coefficients are also obtained analytically for any heaving motion of the airfoil and for any value of the mean angle of attack α. The contributions of the leading- and trailing-edge vortices to the thrust during their down- and up-stroke evolutions, are computed quantitatively with this formulation for different dimensionless frequencies and heave amplitudes (St_c and St_a) and for several values of α. Very different types of flows, periodic, quasi-periodic, and chaotic, described as St_c, St_a, and α, are varied. The optimum values of these parameters for maximum thrust efficiency are obtained and explained in terms of the interactions between the vortices and the forces exerted by them on the airfoil. As in previous numerical and experimental studies on flapping flight at low Reynolds numbers, the optimum thrust efficiency is reached for intermediate frequencies (St_c slightly smaller than one) and a heave amplitude corresponding to an advance ratio close to unity. The optimal mean angle of attack found is zero. The

corresponding flow is periodic, but it becomes chaotic and with smaller average thrust efficiency as $|\alpha|$ becomes slightly different from zero.

Finally, some conclusions and some future work related to the MAVs design based on the vortex force decomposition to study some other interesting flight mechanisms are outlined.

RESUMEN

El principal objetivo de este trabajo es la caracterización cuantitativa de las contribuciones de los elementos fluidos individuales (vórtices) a las fuerzas aerodinámicas, explicando y cuantificando los mecanismos por los cuales se genera tanto la resistencia como la sustentación. Para ello, se ha hecho uso de una formulación de fuerzas aerodinámicas basada en la vorticidad para abordar problemas concretos, ofreciendo un punto de vista físico novedoso al estudio de la dinámica del flujo. Dicha aportación pretende ser de aplicación en el diseño de micro-vehículos aéreos.

En primer lugar se estudia el conocido *Efecto Magnus*. En este problema se investiga, numéricamente, el flujo alrededor de un cilindro que gira mediante una formulación de fuerzas basada en vorticidad. El objetivo de ello es poder analizar, cuantitativamente, las estructuras del flujo y sus evoluciones, las cuales contribuyen a las fuerzas de sustentación y resistencia en el cilindro. El número de Reynolds que se ha considerado en este problema, basado en el diámetro del cilindro y la velocidad de la corriente de entrada, es $Re = 200$, mientras que los valores del parámetro de giro (relación entre la velocidad en la superficie del cilindro y la velocidad de la corriente de entrada) que se han seleccionado son $\alpha = 1$ y 3. Para $\alpha = 1$, cuando el flujo se ha desarrollado por completo, la estela tras el cilindro, y con ella la evolución temporal de las fuerzas de sustentación y resistencia, se vuelven oscilatorias debido al desprendimiento de vórtices tras el cilindro. Sin embargo, para $\alpha = 3$, el flujo en estado permanente es estacionario con valores constantes de la sustentación y la resistencia. En particular, en este caso se genera una sustentación elevada y una baja resistencia aerodinámica. Cada uno de estos casos se ha estudiado en dos problemas transitorios diferentes, uno con aceleración angular del cilindro y velocidad translación constante, y la otra con aceleración lineal del cilindro y velocidad de giro constante. Las constribuciones de los vórtices a las fuerzas aerodinámicas se han caracterizado cuantitativamente, explicando y cuantificando los mecanismos por los cuales se genera sustentación en cada caso. En particular, para rotación alta (cuando $\alpha = 3$), se explica la relación entre los mecanismos de supresión del desprendimiento de vórtices y aquellos por los cuales se produce una mejora de la sustentación y casi se llega a eliminar la resistencia, cuando el flujo se ha desarrollado por completo.

Por otra parte, también se ha estudiado computacionalmente la eficiencia en la propulsión de un ala batiente bidimensional a bajo número de Reynolds, mediante la misma descomposición de fuerzas en términos de la vorticidad. Se ha utilizado un ala elíptica para poder obtener analíticamente los potenciales auxiliares que descomponen la fuerza total generada por los vórtices en sustentación y resistencia (o propulsión). Gracias a dichos potenciales auxiliares también se han obtenido analíticamente la parte de masa añadida de los coeficientes de sustentación y resistencia (o propulsión), para cualquier tipo de movimiento del ala y para cualquier valor del ángulo de ataque medio α. Además, para diferentes frecuencias y amplitudes adimensionales del movimiento (St_a y St_c), así como para varios valores de α, se han calculado computacionalmente

las contribuciones a la propulsión que generan los vórtices de los bordes de entrada y de salida, durante las diferentes batidas hacia arriba y hacia abajo del ala. Gracias a este estudio, se han identificado tres tipos de flujos muy diferentes: periódicos, quasi-periódicos, y caóticos para diferentes valores de St_c, St_a y α. De esta manera, y para maximizar la eficiencia en la propulsión, se han obtenido y explicado en términos de interacciones entre vórtices y de las fuerzas que éstos ejercen sobre el ala, los valores óptimos de St_c, St_a y α. Al igual que en estudios numéricos y experimentales anteriores de alas batientes a bajos números de Reynolds, se ha encontrado la eficiencia de propulsión óptima para frecuencias intermedias (St_c ligeramente menor que uno), y para una amplitud de batida correspondiente a una relación de avance cercana a la unidad. El valor óptimo del ángulo de ataque medio que se ha encontrado es cero. El tipo de flujo correspondiente a este ángulo de ataque es periódico, y a medida que $|\alpha|$ varía ligeramente de cero se vuelve caótico y con una menor eficiencia en la propulsión media.

Por último, se exponen las conclusiones de esta tesis doctoral y se plantean trabajos futuros relacionados con el diseño de micro-vehículos aéreos y con el estudio de otros mecanismos de vuelo interesantes mediante la técnica de descomposición de fuerzas basada en la vorticidad.

PUBLICATIONS

Most of the contents of this thesis have been published in the following JCR-indexed publications:

- A. Martín-Alcántara, E. Sanmiguel-Rojas and R. Fernandez-Feria. "On the development of lift and drag in a rotating and translating cylinder". In: Journal of Fluids and Structures 54 (2015) pp. 868–885

- A. Martín-Alcántara, R. Fernandez-Feria and E. Sanmiguel-Rojas. "Vortex flow structures and interactions for the optimum thrust efficiency of a heaving airfoil at different mean angles of attack". In: Physics of Fluids 27, 073602 (2015)

CONTENTS

LIST OF TABLES

LISTINGS

INTRODUCTION

1.1 MOTIVATION AND OBJECTIVES

The unsteady aerodynamics of oscillating airfoils at the low Reynolds number range of interest for small flying animals (mostly insects) has been widely studied theoretically, numerically and experimentally. The main motivation of many of these studies is the understanding of the flow mechanisms by which the lift is greatly enhanced in relation to the predictions of the quasi-steady aerodynamic theory, and the mechanisms by which thrust or propulsion is generated. Traditionally, these studies were aimed to the understanding of the biomechanics of insect (and small birds and mammals) flight (see e.g. Maxworthy, 1981; Dudley, 2000; Sane, 2003 and Wang, 2005). But the interest in the unsteady aerodynamics of flapping flight has significantly grown in the recent years in relation to the design of Micro-Aerial Vehicles (MAVs), taking advantage of the accumulated knowledge on animal flight (Ellington, 1999; Mueller, 2001; Pines and Bohorquez, 2006; Ansari et al., 2009 and Jones and Platzer, 2009).

Therefore, different kinds of spatial patterns of vortices have been identified in several forms of propulsion by aquatic animals (see Wu, 1961; Lighthill, 1969; Lighthill, 1970 and Lighthill, 1975). In addition, in many of the proposed thrust mechanisms, the leading-edge vortex generated during the wing-beat plays an important role. It is well known that the high lift coefficients characterizing most insects flight are due to the low-pressure regions inside the leading-edge vortex generated temporarily, after a sudden change in the effective local angle of attack during flapping (Lighthill, 1975; Maxworthy, 1979; Dickinson and Götz, 1993; Ellington et al., 1996; Liu et al., 1998; Sane and Dickinson, 2001; Minotti, 2002; Maxworthy, 2007; Shyy and Liu, 2007 and Pitt and Babinsky, 2013). To optimize this effect, most insects fly at the limit of dynamic stall to generate a prominent leading-edge vortex. The relevance of the leading-edge vortex for high efficiency thrust and propulsion by a pure heaving motion was first acknowledged and studied in relation to simple models for fish swimming (Streitlien et al., 1996; Anderson et al., 1998 and Triantafyllou et al., 2000).

On the other hand, the origins of MAVs date back to about 1997 (Ansari et al., 2006). Since then, although smaller scales of the existing and conventional vehicles are proved to be valid in outdoor scenarios, they suffer from efficiency and from effectiveness in indoor flight. For instance, an aircraft model lacks of manoeuvrability in closed spaces and it needs large distances to take off and land. However, a rotorcraft or a multi-rotorcraft succeeds in agility but it results to be noisy and inefficient. On the contrary, insect-like flapping vehicles are much more efficient and agile than the previous models but equipping them with a long-life power supply is a challenge. In developing a MAV, the main aim is to predict quantitatively the behaviour of the physical phenomena occurring during the flight, being able of manoeuvring when needed in order to keep a stable flight. Therefore, it is required to have a fully knowledge on the flow dynamics

appearing in this kind of flight. The works studied in this thesis enlighten the study of the flow mechanisms as well as the vortical interactions inherent to flapping flight, in order to be useful e.g. when flapping-like MAV needs to flight in an optimum thrust-mode or to develop a given lift.

To this end, two bidimensional problems are studied computationally in the present thesis by using the open source code OpenFOAM® via the formulation of Chang (1992). OpenFOAM® is based on the C++ programming language, so it offers the flexibility and efficiency of an Object-Oriented language in programming. As an essential contribution, as well as an example of the OpenFOAM® versatility, it is worth to remark that the computation of the different contributions of the formulation of Chang (1992) have been properly implemented within this software by using `functionObjects` (see e.g. Stroustrup, 2013, OpenCFD, 2014 and Marić et al., 2014). In this manner, it is possible to have access to every contribution in any time instant as the magnitudes are computed during the `runTime` of the simulation, having a negligible computational cost since 2D grids have been used in this thesis.

The first problem is addressed in Chapter 4 and it is based on the study of the *Magnus Effect*, a classic problem in Fluid Mechanics. It serves as a preamble to set up the laminar incompressible code coupled along numerically with the formulation of Chang (1992). In this problem two unsteady effects are studied: (i) an accelerating cylinder starting from rest to a given velocity with constant angular velocity, and (ii) a constant inlet flow around a spinning cylinder accelerating from rest to a given angular velocity.

The second problem (Chapter 5) is based on the investigation of the optimum thrust efficiency for a two-dimensional, laminar and incompressible flow around an elliptic foil performing a sinusoidal flapping motion. A wide range of characteristic frequencies and amplitudes related to the motion are studied in order to finally generate a map of the flight efficiency. In addition, three different flow dynamics are identified: periodic, quasi-periodic, and chaotic or aperiodic. It is demonstrated to be dependent on both the wing-beat amplitude and frequency.

Finally, the core of this dissertation is the analysis of the aerodynamics forces for unsteady problems at relative low-Reynolds numbers by using the vortex force decomposition originally developed by Chang (1992). This formulation provides the quantitative contribution of each vortex flow structure to the force coefficients at any instant of time (see Lee et al., 2012 and Martín-Alcántara et al., 2015). In this manner, it is possible to explain better all the mechanisms by which lift and thrust are generated in order to be applied to the MAVs design.

1.2 THESIS OUTLINE

This document is organized as follows.

First of all, Chapter 2 introduces the vortex force decomposition developed by Chang (1992). It is initially done in a generic form to be then characterized for each of the problems studied in this thesis.

Chapter 3 serves as a numerical introduction to the OpenFOAM® basics as well as to the Finite Volume Method and the way in which is implemented in this open-source toolbox.

Chapter 4 provides an analysis on the *Magnus Effect*. Some conclusions on the lift generation and on the unsteadiness or steadiness regimes in the vortex shedding are drawn from the point of view of the vortex force decomposition.

Chapter 5 presents a parametric study on the influence of the amplitudes, frequencies and angles of attack on the thrust efficiency of a two-dimensional wing in forward flapping flight. The optimum parameters are selected and a sensitivity study on the different flow regimes is provided.

Finally, to conclude, Chapter 6 gathers all the contributions provided in this document as well as some suggestions for future works related with the thesis.

CONTRIBUTION OF FLUID ELEMENTS TO THE LIFT AND DRAG COEFFICIENTS: A PROJECTION METHOD

2.1 INTRODUCTION

The present chapter is devoted to introduce the formulation developed by Chang (1992). The use of this formulation allows to understand how the onset of vortices in the flow contributes to the aerodynamic forces through the vorticity in the flow field. This analysis has been firstly applied in this thesis to the well-known *Magnus Effect* problem (see Chapter 4), and then to a problem based on a two-dimensional flow past a heaving foil (see Chapter 5).

Two auxiliary potential functions need to be introduced to obtain the contribution to the force coefficients: one of them associated to the drag coefficient and the other one to the lift. After some manipulations involving the auxiliary potentials, the force coefficients are separated into four parts: one due to an added-mass term (see Yih, 1977), one due to the motion of the body, another one due to the vorticity within the flow field, and the other due to the surface vorticity. The third one is the most relevant to identify flow structures contributing to the lift and to the drag.

Finally, for the sake of clarity, a generic description of the vortex force decomposition will be first introduced in Sec. 2.2 to be later characterized in Subsecs. 2.2.1 and 2.2.2, according to the problems studied in Chapters 4 and 5, respectively.

2.2 MATHEMATICAL FORMULATION

The non-dimensional Navier–Stokes equations governing an incompressible viscous flow can be written as:

$$\nabla \cdot \mathbf{v} = 0, \tag{2.1}$$

$$q\frac{\partial \mathbf{v}}{\partial t} + \mathbf{v} \cdot \nabla \mathbf{v} = -\nabla p + \frac{1}{\text{Re}}\nabla^2 \mathbf{v}, \tag{2.2}$$

where $\mathbf{v}$ is the non-dimensional velocity, p is the non-dimensional relative pressure (scaled with ρU_0^2, being ρ the fluid density and U_0 the freestream speed). A unsteady acceleration parameter $q = l/(U_0 t_c)$ and the Reynolds number $Re = \rho U_0 l/\mu$ are introduced for a given chord-based length l, acceleration time t_c and fluid viscosity μ.

Then, to write the lift and drag forces only in terms of velocity and vorticity (without the intervention of the pressure field), one makes use of auxiliary potentials satisfying Laplace's equations with appropriate boundary conditions (Chang, 1992; Lee et al., 2012). The solution is required to vanish at infinity, where the fluid is at rest (see

Fig. 2.1 for a sketch of the general geometry). Then, the auxiliary harmonic function, e.g in the case of the lift coefficient, must satisfy

$$\nabla^2 \phi = 0 \quad \text{in } V, \tag{2.3}$$

$$|\mathbf{x}| \to \infty, \quad \phi \to 0, \quad \mathbf{n} \cdot \nabla \phi = -\mathbf{n} \cdot \mathbf{e}_y \quad \text{on } S. \tag{2.4}$$
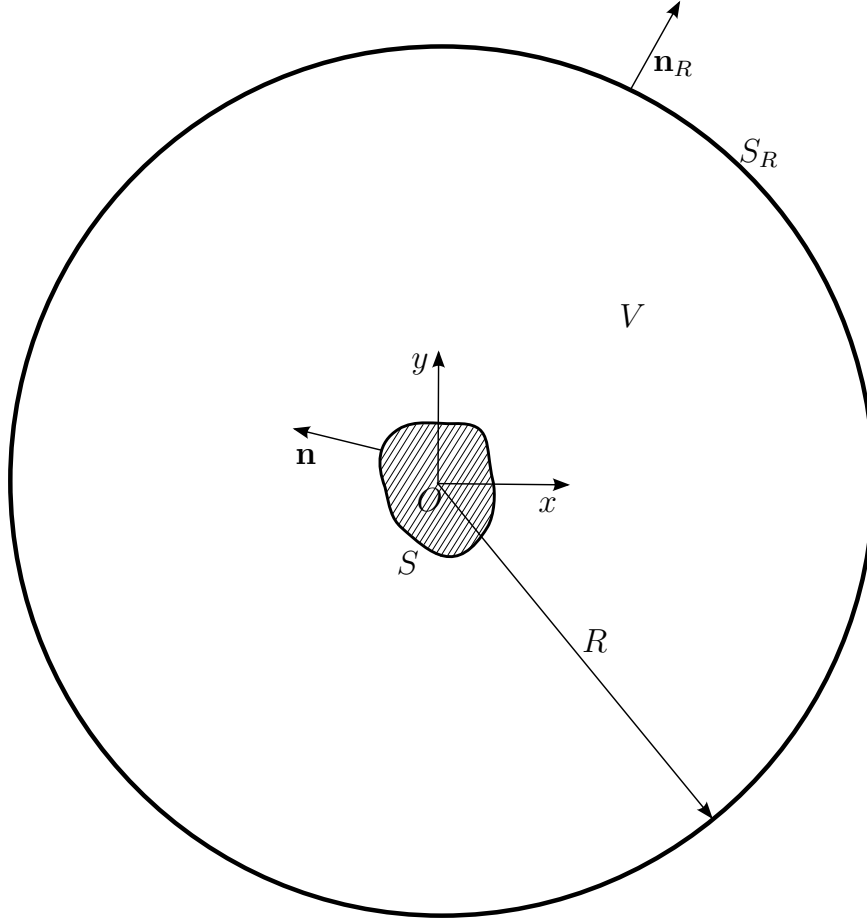
Figure 2.1: Definition sketch for fluid extending to infinity and at rest there.

Making the scalar product of the momentum equation (2.2) with $\nabla \phi$ and integrating over the volume V (area in this case), which for operational purposes is limited by the body surface S (curve) and an outer surface S_R given by $|\mathbf{x}| = R \to \infty$; after some vector operations and the application of the Gauss theorem as well as the definition of ϕ in (2.3) and (2.4), one obtains (note that $\mathbf{n}$ is the outward unit vector normal to S as seen from the body, while in Gauss theorem the outward unit vector to S as seen from V, $-\mathbf{n}$, is used instead)

$$
\begin{aligned}
&- 2q \int_S \phi \frac{\partial}{\partial t} \mathbf{v} \cdot \mathbf{n} \, ds + \int_S v^2 \mathbf{n} \cdot \mathbf{e}_y \, ds - 2 \int_V (\mathbf{v} \wedge \boldsymbol{\omega}) \cdot \nabla \phi \, dV \\
&= -2 \int_S p\mathbf{n} \cdot \mathbf{e}_y \, ds + \frac{2}{\text{Re}} \int_S (\mathbf{n} \wedge \boldsymbol{\omega}) \cdot \nabla \phi \, ds,
\end{aligned}
\tag{2.5}
$$

where the second and last terms of (2.2) have been rewritten using the mathematical identities $\mathbf{v} \cdot \nabla \mathbf{v} = \nabla v^2/2 - \mathbf{v} \wedge \boldsymbol{\omega}$ and $\nabla^2 \mathbf{v} = -\nabla \wedge \boldsymbol{\omega}$ (when $\nabla \cdot \mathbf{v} = 0$). Note that the integrals over the surface S_R vanish because the solution to (2.3) and (2.4) satisfies $|\nabla \phi| \sim 1/|\mathbf{x}|^2 \to 0$ as $|\mathbf{x}| \to \infty$. Thus, it is found that the $y-$component of the pressure force over S in terms of some surface and volume integrals of the velocity and vorticity fields, so that the lift coefficient is given by

$$
\begin{aligned}
C_L &\equiv -2 \int_S p\mathbf{n} \cdot \mathbf{e}_y \, \mathrm{d}s + \frac{2}{\mathrm{Re}} \int_S (\boldsymbol{\omega} \wedge \mathbf{n}) \cdot \mathbf{e}_y \, \mathrm{d}s \\
&= -2q \int_S \phi \frac{\partial}{\partial t} \mathbf{v} \cdot \mathbf{n} \, \mathrm{d}s + \int_S v^2 \mathbf{n} \cdot \mathbf{e}_y \, \mathrm{d}s - 2 \int_V (\mathbf{v} \wedge \boldsymbol{\omega}) \cdot \nabla \phi \, \mathrm{d}V \\
&+ \frac{2}{\mathrm{Re}} \int_S (\mathbf{n} \wedge \boldsymbol{\omega}) \cdot \nabla \phi \, \mathrm{d}s \equiv C_{La} + C_{Lm} + C_{Lv} + C_{Ls},
\end{aligned}
\tag{2.6}
$$

where the pressure field is absent. Note that the last surface term C_{Ls} has a contribution from the pressure forces and another one from the viscous forces, while the remaining terms come from the pressure forces. The term involving a volume integral, C_{Lv}, which is the most relevant one in the present study, is related to the projection of Lamb's vector $\boldsymbol{\omega} \wedge \mathbf{v}$ on the direction of $\nabla \phi$. The other two terms, C_{La} and C_{Lm}, are added-mass (e.g., Yih, 1977) and rotational contributions to the lift force, respectively.

Alternatively, defining the function $\overline{\phi}$ satisfying

$$
\nabla^2 \overline{\phi} = 0 \quad \text{in } V,
\tag{2.7}
$$

$$
|x| \to \infty, \quad \overline{\phi} \to 0, \quad \mathbf{n} \cdot \nabla \overline{\phi} = -\mathbf{n} \cdot \mathbf{e}_x \quad \text{on } S,
\tag{2.8}
$$

one may write the non-dimensional drag ($x-$component) force as

$$
\begin{aligned}
C_D &\equiv -2 \int_S p\mathbf{n} \cdot \mathbf{e}_x \, \mathrm{d}s + \frac{2}{\mathrm{Re}} \int_S (\boldsymbol{\omega} \wedge \mathbf{n}) \cdot \mathbf{e}_y \, \mathrm{d}s \\
&= -2q \int_S \overline{\phi} \frac{\partial}{\partial t} \mathbf{v} \cdot \mathbf{n} \, \mathrm{d}s + \int_S v^2 \mathbf{n} \cdot \mathbf{e}_x \, \mathrm{d}s - 2 \int_V (\mathbf{v} \wedge \boldsymbol{\omega}) \cdot \nabla \overline{\phi} \, \mathrm{d}V \\
&+ \frac{2}{\mathrm{Re}} \int_S (\mathbf{n} \wedge \boldsymbol{\omega}) \cdot \nabla \overline{\phi} \, \mathrm{d}s \equiv C_{Da} + C_{Dm} + C_{Dv} + C_{Ds}.
\end{aligned}
\tag{2.9}
$$

A detailed characterization of the vortex force decomposition is shown next in Subsects. 2.2.1 and 2.2.2. The reader can find in Chapters 4 and 5 a more complete description of this formulation fitting the problems studied in these Chapters.

2.2.1 *Detailed formulation of the problem studied in Chapter 4*

The two-dimensional unsteady incompressible flow around a rotating cylinder is considered. Unsteady accelerating effects are also considered. The Navier–Stokes equations (2.1) and (2.2) governing this problem can be written in a relative frame fixed to the body as

$$
\nabla \cdot \mathbf{v} = 0,
\tag{2.10}
$$

$$
q \frac{\partial}{\partial t}(\mathbf{v} - U\mathbf{e}_x) + \mathbf{v} \cdot \nabla \mathbf{v} = -\nabla p + \frac{2}{\mathrm{Re}} \nabla^2 \mathbf{v},
\tag{2.11}
$$

being $U\mathbf{e}_x = U(t)\mathbf{e}_x$ the non-dimensional accelerating velocity in the freestream direction. Notice that, in this case, the characteristic length is defined to be the radius a of the cylinder whereas the Reynolds number is based on the on the cylinder's diameter $2a$, i.e. $q = a/(U_0 t_c)$ and $Re = \rho U_0 l/\mu$.

Thus, the non-dimensional force (scaled with $1/2\rho v^2 2a = \rho v^2 a$) that the fluid exerts on the cylinder surface $r \equiv |\mathbf{x}| = 1$ can be written as the sum of the pressure and viscous friction forces as

$$\mathbf{F} = -\int_{r=1} p\mathbf{n} \ \mathrm{d}s + \frac{2}{Re}\int_{r=1}(\boldsymbol{\omega} \wedge \mathbf{n}) \ \mathrm{d}s, \tag{2.12}$$

where $\mathbf{n}$ is the outwards unit vector normal to the cylinder surface ($\mathbf{n} = \mathbf{e}_r$) and $\boldsymbol{\omega} = \nabla \wedge \mathbf{v}$ is the non-dimensional vorticity. Since we are considering a two-dimensional flow, $\mathbf{v} = v_r\mathbf{e}_r + v_\theta\mathbf{e}_\theta$ in cylindrical polar coordinates, the vorticity is perpendicular to the flow, $\boldsymbol{\omega} = \omega\mathbf{e}_z \equiv (1/r)[\partial(rv_\theta)/\partial r - \partial v_r/\partial\theta]\mathbf{e}_z$, where $\mathbf{e}_z$ is the unit vector perpendicular to the plane of the flow, and $\boldsymbol{\omega} \wedge \mathbf{n} = \omega\mathbf{e}_\theta$. Thus, the $x-$ and $y-$components of $\mathbf{F}$, i.e. the drag and lift coefficients, respectively, can be written as

$$C_D = -\int_0^{2\pi} p_1\cos\theta \ \mathrm{d}\theta - \frac{2}{Re}\int_0^{2\pi}\omega_1\sin\theta \ \mathrm{d}\theta, \tag{2.13}$$

$$C_L = -\int_0^{2\pi} p_1\sin\theta \ \mathrm{d}\theta + \frac{2}{Re}\int_0^{2\pi}\omega_1\cos\theta \ \mathrm{d}\theta, \tag{2.14}$$

where $p_1(\theta, t) \equiv p|_{r=1}(\theta, t)$ and $\omega_1(\theta, t) \equiv \omega|_{r=1}(\theta, t)$.

We shall obtain the drag and the lift coefficients using the formulation developed by Chang (1992) that allows for a quantitative identification of the contributions of the different vortex flow structures to these forces (see Lee et al., 2012). This formulation is based on the use of auxiliary potentials, one for the lift and the other one for the drag, that transform the surface integrals in (2.13) and (2.14), containing the pressure, into volume and surface integrals incorporating the velocity and vorticity fields [see (2.9)]. In the case of the lift force, the auxiliary function ϕ for the present problem is given by (2.3) and (2.4) with the analytical solution $\phi = (\sin\theta)/r$. Substituting into the general expression for the lift (2.6) and taking into account that S is now the circumference $|\mathbf{x}| = 1$, with $\mathbf{n} = \mathbf{e}_r$, and the volume V corresponds to $r \geq 1$, one obtains that $C_{La} = C_{Lm} = 0$ (i.e., there is no contribution to the lift force from the velocity and acceleration of the cylinder), and the lift coefficient is given by

$$C_L = C_{Lv} + C_{Ls} = \int_1^\infty \int_0^{2\pi} \delta_{Lv}r \ \mathrm{d}\theta + \frac{4}{Re}\int_0^{2\pi}\omega_1\cos\theta \ \mathrm{d}\theta, \tag{2.15}$$

with

$$\delta_{Lv} = \frac{v_\theta \ \omega\sin\theta + v_r \ \omega\cos\theta}{r^2}. \tag{2.16}$$

Note that the friction force [second term in (2.14)] is just half of the surface integral C_{Ls} in the lift coefficient (2.15), while the other half of that surface integral, together with the volumetric integral C_{Lv}, comes from the pressure force term in (2.14). The quantity δ_{Lv} can be interpreted as a kind of volumetric density of lift force, decay-

ing quadratically with the distance to the origin (and to the cylinder). It will be one of the main quantities to be computed below as a measure of the contribution of the different parts and structures of the flow to the lift force on the cylinder at each instant.

Similarly, the auxiliary function $\overline{\phi}$ for the drag satisfying (2.7) and (2.8) has the analytical solution $\overline{\phi} = (\cos\theta)/r$. The contributions to the drag coefficient (2.9) are similar to those described above for C_L, except for the fact that now there is an additional contribution to C_{Da} associated with the non-dimensional acceleration of the cylinder $\mathrm{d}U = \mathrm{d}t$:

$$
\begin{aligned}
C_D &= C_{Da} + C_{Dv} + C_{Ds} \\
&= \pi q \frac{\mathrm{d}U}{\mathrm{d}t} + \int_1^\infty \int_0^{2\pi} \delta_{Dv} r \, \mathrm{d}\theta \, \mathrm{d}r - \frac{4}{\mathrm{Re}} \int_0^{2\pi} \omega_1 \sin\theta \, \mathrm{d}\theta,
\end{aligned}
\tag{2.17}
$$

with

$$
\delta_{Dv} = \frac{v_\theta \, \omega \cos\theta - v_r \, \omega \sin\theta}{r^2}.
\tag{2.18}
$$

As before, the friction force [second term in (2.13)] is just half of the surface integral C_{Ds} in the drag coefficient (2.17), while the other half of that surface integral plus the volumetric integral C_{Dv} and the acceleration term C_{Da} comes from the pressure force term in (2.13). The quantity δ_{Dv} is a density of drag force, decaying also quadratically with r. Note that the term C_{Da} only appears in the case (ii), and that an accelerating cylinder in a fluid at rest, i.e. the case considered here, is not equivalent to a cylinder at rest within an accelerating freestream.

It is worth noticing that for a potential flow with circulation $\Gamma = 2\pi a^2 \Omega_0$, i.e. for a flow with a non-dimensional velocity field given by $v_r = \cos\theta(1 - 1/r^2)$ and $v_\theta = -\sin\theta(1 + 1/r^2)$, all the terms of C_D are obviously zero, and the only non-vanishing term in C_L is C_{Lm} [see (2.6)], which does not appear in (2.5) for the viscous flow. In fact, on substituting the potential velocity field into (2.6) yields

$$
C_L = C_{Lm} = \int_0^{2\pi} \frac{v_\theta^2|_{r=1}}{2} \sin\theta \, \mathrm{d}\theta = 4\pi a,
\tag{2.19}
$$

which is the Kutta–Joukowski lift formula for the given circulation. This expression is not of interest here because of the relatively small value of Re considered in this work.

2.2.2 *Detailed formulation of the problem studied in Chapter 5*

The two-dimensional unsteady and incompressible flow of a uniform current over an oscillating ellipse is investigated numerically. In this case, the ellipse, which represents a wing element with chord length c and thickness e, forms an angle α with the current of constant speed U and performs a sinusoidal heaving motion perpendicular to the current with amplitude h_0 and frequency f, given by

$$
h(t) = h_0 \sin(2\pi f t),
\tag{2.20}
$$

and by the following parameters:

$$\text{Re} = \frac{\rho U c}{\mu}, \quad St_a = \frac{h_0 f}{U}, \quad St_c = \frac{cf}{U}. \tag{2.21}$$

Then, taking into account (2.1) and (2.2), and that there is no accelerating term in this case, the Navier–Stokes equations governing this problem are given by

$$\nabla \cdot \mathbf{v} = 0, \tag{2.22}$$

$$\frac{\partial \mathbf{v}}{\partial t} + \mathbf{v} \cdot \nabla \mathbf{v} = -\nabla p + \frac{1}{\text{Re}} \nabla^2 \mathbf{v}. \tag{2.23}$$

In the same manner, (2.6) and (2.9) were solved so the drag and lift coefficients, in terms of the formulation of Chang (1992), can be written for this problem as

$$
\begin{aligned}
C_L &= -2 \int_S \phi \frac{\partial \mathbf{v}}{\partial t} \cdot \mathbf{n} \, ds + \int_S v^2 \mathbf{n} \cdot \mathbf{e}_y \, ds - 2 \int_V (\mathbf{v} \wedge \boldsymbol{\omega}) \cdot \nabla \phi \, dV \\
&+ \frac{2}{\text{Re}} \int_S (\boldsymbol{\omega} \wedge \mathbf{n}) \cdot (\nabla \phi + \mathbf{e}_y) \, ds \equiv C_{La} + C_{Lm} + C_{Lv} + C_{Ls},
\end{aligned} \tag{2.24}
$$

and

$$
\begin{aligned}
C_D &= -2 \int_S \overline{\phi} \frac{\partial \mathbf{v}}{\partial t} \cdot \mathbf{n} \, ds + \int_S v^2 \mathbf{n} \cdot \mathbf{e}_x \, ds - 2 \int_V (\mathbf{v} \wedge \boldsymbol{\omega}) \cdot \nabla \overline{\phi} \, dV \\
&+ \frac{2}{\text{Re}} \int_S (\boldsymbol{\omega} \wedge \mathbf{n}) \cdot (\nabla \overline{\phi} + \mathbf{e}_x) \, ds \equiv C_{Da} + C_{Dm} + C_{Dv} + C_{Ds},
\end{aligned} \tag{2.25}
$$

given, respectively, by (2.3)–(2.4), and (2.7)–(2.8).

As in Subsect 2.2.1, the "drag density" δ_{Dv} is here also introduced. It is defined as the integrand of C_{Dv} in (2.25), i.e.,

$$C_{Dv} = \int_V \delta_{Dv} \, dV, \quad \delta_{Dv} \equiv 2(\boldsymbol{\omega} \wedge \mathbf{v}) \cdot \nabla \overline{\phi}, \tag{2.26}$$

where δ_{Dv} is negative in the points where the flow contributes to the thrust of the airfoil and positive in the points that contribute to the drag. Note that δ_{Dv} is twice the projection of Lamb's vector $\boldsymbol{\omega} \wedge \mathbf{v}$, which is responsible for this vortex force (Saffman, 1992), on the gradient of the auxiliary potential $\overline{\phi}$. This ensures that δ_{Dv} decays rapidly as we move away from the airfoil, because, according to (2.7) and (2.8), far from the (moving) 2D body, $\nabla \overline{\phi}$ decays quadratically with the distance to it, as can be seen in Hsieh et al. (2010). In the present 2D flow, δ_{Dv} can be written as

$$\delta_{Dv} = -2\omega v \frac{\partial \overline{\phi}}{\partial x} + 2\omega u \frac{\partial \overline{\phi}}{\partial y}, \tag{2.27}$$

since $\mathbf{v} = u\mathbf{e}_x + v\mathbf{e}_y$ and $\boldsymbol{\omega} = \omega \mathbf{e}_z$.

On the other hand, in the case of an elliptic surface S, Laplace's equation in (2.3)–(2.4) and in (2.7)–(2.8), can be solved analytically by separation of variables using elliptic coordinates (see Morse and Feshbach, 1953), in a reference frame moving with

the ellipse. For an ellipse with its main axis of length unity in the $x-$axis (i.e., $\alpha = 0$), the elliptic coordinates (ξ, η) are related to (x, y) through

$$x = \frac{1}{2}\sqrt{1 - \epsilon^2}\cosh\xi\cos\eta, \quad y = \frac{1}{2}\sqrt{1 - \epsilon^2}\sinh\xi\sin\eta, \tag{2.28}$$

where ϵ is the minor axis length in the $y-$axis, and the ellipse S is given by $\xi = \xi_0 \ln[(1 + \epsilon)/(1 - \epsilon)]/2$, and $0 \leq \eta \leq 2\pi$. In these coordinates, the solutions to problems (2.3)–(2.4), and (2.7)–(2.8) can be written, respectively, as

$$\phi = \frac{1}{2}\sqrt{\frac{1 + \epsilon}{1 - \epsilon}}e^{-\xi}\sin\eta, \quad \overline{\phi} = \frac{\epsilon}{2}\sqrt{\frac{1 + \epsilon}{1 - \epsilon}}e^{-\xi}\cos\eta, \tag{2.29}$$

which on the ellipse are

$$\phi = \phi_0 = \frac{1}{2}\sin\eta, \quad \overline{\phi} = \overline{\phi}_0 = \frac{\epsilon}{2}\cos\eta. \tag{2.30}$$

For an ellipse at an angle $-\alpha$ with the $x-$axis, like in Fig. 5.1, one only has to rotate the coordinate axes in boundary conditions (2.4) and (2.8) on the surface of the ellipse to get

$$\phi = \frac{1}{2}\sqrt{\frac{1 + \epsilon}{1 - \epsilon}}e^{-\xi}(\cos\alpha\sin\eta - \epsilon\sin\alpha\cos\eta),$$

$$\overline{\phi} = \frac{1}{2}\sqrt{\frac{1 + \epsilon}{1 - \epsilon}}e^{-\xi}(\sin\alpha\sin\eta + \epsilon\cos\alpha\cos\eta), \tag{2.31}$$

$$\phi_0 = \frac{1}{2}(\cos\alpha\sin\eta - \epsilon\sin\alpha\cos\eta), \quad \overline{\phi}_0 = \frac{1}{2}(\sin\alpha\sin\eta + \epsilon\cos\alpha\cos\eta), \tag{2.32}$$

where (ξ, η) are the elliptic coordinates of the "rotated" ellipse.

For any surface S moving with a velocity V that does not vary along the surface (it may depend on time like in the present sinusoidal heaving motion), the "m" (or rotational) components of C_D and C_L in (2.9) and (2.6) vanish, respectively, i.e.

$$C_{Dm} = \oint_S v^2\mathbf{n}\cdot\mathbf{e}_x\,\mathrm{d}s = V^2(t)\oint_S \mathbf{n}\cdot\mathbf{e}_x\,\mathrm{d}s = 0, \tag{2.33}$$

and similarly for C_{Lm}, where the circle in the integral symbol has been included to emphasize that S is a closed surface. On the other hand, the "a" components in the case of an ellipse can be obtained analytically using auxiliary potentials (2.32) on the ellipse,

$$C_{Da} = -2\int_S \overline{\phi}\frac{\partial\mathbf{v}}{\partial t}\cdot\mathrm{d}s = -2\frac{\mathrm{d}\mathbf{V}}{\mathrm{d}t}\cdot\int_0^{2\pi}\overline{\phi}_0\mathbf{e}_\xi h_\eta\,\mathrm{d}\eta$$

$$= -\frac{\pi}{2}\left[(1 - \epsilon^2)\sin\alpha\cos\alpha\frac{\mathrm{d}V_y}{\mathrm{d}t} + (\sin^2\alpha + \epsilon^2\cos^2\alpha)\frac{\mathrm{d}V_x}{\mathrm{d}t}\right], \tag{2.34}$$

where use has been made of $\mathbf{n} = \mathbf{e}_\xi = \sqrt{1 - \epsilon^2}(\sinh\xi_0\cos\eta\,\mathbf{i} + \cosh\xi_0\sin\eta\,\mathbf{j})/(2h_\xi)$ over the ellipse $\xi = \xi_0$, with $\mathbf{i}$ and $\mathbf{j}$ the unit vectors along the axes of the ellipse, and

$h_\eta = h_\xi$. Note that the components of $\mathbf{V}$ on the (x, y) axes have been projected on $\mathbf{i}$ and $\mathbf{j}$. Similarly for C_{La},

$$
\begin{aligned}
C_{La} &= -2 \int_S \phi \frac{\partial \mathbf{v}}{t} \cdot \mathbf{n} \, \mathrm{d}s = -2 \frac{\mathrm{d}\mathbf{V}}{\mathrm{d}t} \cdot \int_0^{2\pi} \phi_0 \mathbf{e}_\xi h_\eta \, \mathrm{d}\eta \\
&= -\frac{\pi}{2} \left[(\cos^2 \alpha + \epsilon^2 \sin^2 \alpha) \frac{\mathrm{d}V_y}{\mathrm{d}t} + (1 - \epsilon^2) \sin \alpha \cos \alpha \frac{\mathrm{d}V_y}{\mathrm{d}t} \right].
\end{aligned}
\tag{2.35}
$$

Clearly, these are *added-mass* terms of the hydrodynamic forces (Yih, 1977).

In the present vertical heaving motion $(V_x = 0)$, one has

$$
C_{Da} = -\frac{\pi}{2}(1 - \epsilon^2) \sin \alpha \cos \alpha \frac{\mathrm{d}V_y}{\mathrm{d}t}, \quad C_{La} = -\frac{\pi}{2}(\cos^2 \alpha + \epsilon^2 \sin^2 \alpha) \frac{\mathrm{d}V_y}{\mathrm{d}t}, \tag{2.36}
$$

that for a horizontal ellipse $(\alpha = 0)$ yields

$$
C_{Da} = 0, \quad C_{La} = -\frac{\pi}{2} \frac{\mathrm{d}V_y}{\mathrm{d}t}. \tag{2.37}
$$
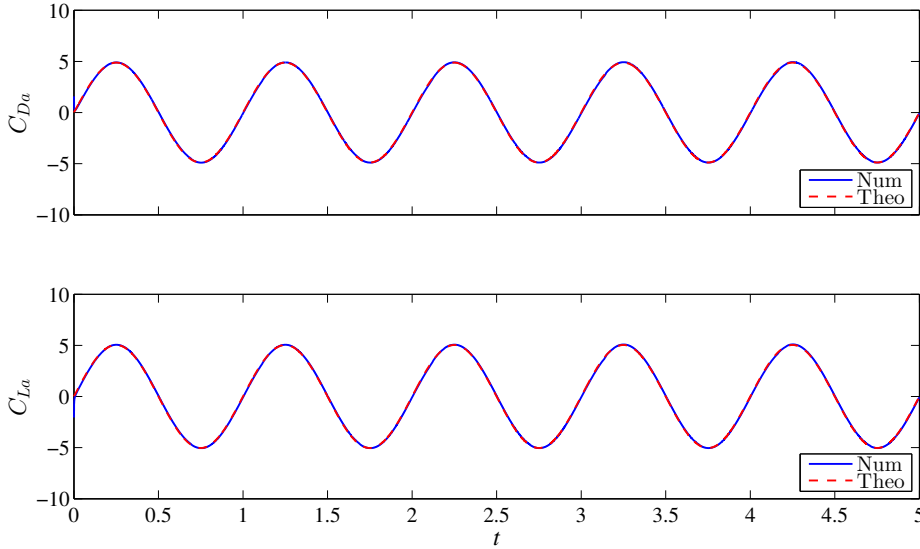
Figure 2.2: Comparison of C_{Da} and C_{La} obtained numerically with (2.39) and (2.40) for an oscillating ellipse with $\epsilon = 1/8$, $\alpha = 45°$, $St_a = 0.16$, $St_c = 1$ and $Re = 500$.

Finally, for the heaving motion described in (2.20),

$$
V_y = \frac{\mathrm{d}H}{\mathrm{d}t} = 2\pi St_a \cos(2\pi St_c t), \tag{2.38}
$$

it is found that

$$
C_{Da} = 2\pi^3 St_a St_c (1 - \epsilon^2) \sin \alpha \cos \alpha \sin(2\pi St_c t), \tag{2.39}
$$

$$
C_{La} = 2\pi^3 St_a St_c (\cos^2 \alpha + \epsilon^2 \sin^2 \alpha) \sin(2\pi St_c t). \tag{2.40}
$$

We checked in several and quite different cases that the numerical results for C_{Da} and C_{La} coincide exactly with these analytical expressions (e.g., Fig. 2.2). Note that these analytical results for C_{Da} and C_{La} are independent of the Reynolds number.

2.3   CONCLUDING REMARKS

In this chapter the formulation developed by Chang (1992) is briefly described and applied to the two particular 2D problems considered in Chapters 4 and 5. This force decomposition enables us to determine the contributions to drag or lift coefficients by fluid elements through the vorticity field.

Some comments on the implementation of this formulation within the OpenFOAM® framework are made in the next Chapter.

OpenFOAM® AND THE FINITE VOLUME METHOD

3.1 INTRODUCTION

This chapter is devoted to give a brief overview of the computational toolbox Open-FOAM® (Open source Field Operation And Manipulation). The OpenFOAM® package is foremost a C++ library based on the Finite Volume Method (see Ferziger and Perić, 2001), used primarily to create executables, known as applications. The applications fall into two categories: solvers, that are each designed to solve a specific problem in continuum mechanics; and utilities, that are developed to perform tasks that involve data manipulation.

One of the advantages of using OpenFOAM® lies on the Open-Source General Public License (GPL) which means that OpenFOAM® can be freely handled and modified when needed by the user. Besides, the development of new solvers and utilities is a straightforward task for an user with a minimal C++ and Object Oriented Programming (OOP) background, which involves terms such as *abstraction, inheritance* and *polymorphism* (see Stroustrup, 2013). As a result, the OpenFOAM® community has widely grown in the past few years as well as the documentation on the use and development of this package.

On the other hand, a disadvantage of using OpenFOAM® is the larger amount of effort required in learning how it works when compared to many other CFD commercial codes. Despite the fact that CFD commecial codes are easier to use and learn, they can be considered as a black-box since the code written in them is not accessible or freely modified by the user.

Finally, both the Finite Volume Method and the PISO algorithm (Issa, 1985) are introduced in the next sections of this chapter in the way they are implemented in OpenFOAM®.

3.2 THE FINITE VOLUME METHOD IN OpenFOAM®

As any discretization method, the aim of the Finite Volume Method (FVM) is to discretize a set of partial diferential equations into an algebraic system. In this case, the physical properties that define an incompressible, iso-thermal fluid flow governed by Navier–Stokes equations (see Weller et al., 1998),

$$\nabla \mathbf{U} = 0, \tag{3.1}$$

$$\frac{\partial \mathbf{U}}{\partial t} + \nabla \cdot (\mathbf{U}\mathbf{U}) - \nabla \cdot 2\nu \mathbf{D} = -\frac{1}{\rho}\nabla p, \tag{3.2}$$

where $\mathbf{U}$ is the velocity field, p the pressure and $D = 1/2(\nabla\mathbf{U} + \nabla\mathbf{U}^T)$. Due to the nonlinearity in (3.1) and (3.2), the fluid flow problems with analytical solutions are really scarce in Fluid Mechanics (e.g., the *Couette flow* or the *Hagen–Poiseuille* solution), hence the most of them can only be solved by using computational methods. It means that (3.1) and (3.2) need to be discretized in a system of algebraic equations able of being solved. The solution technique used in OpenFOAM® is the Finite Volume Method (see e.g. Ferziger and Perić, 2001) consisting of two parts: domain and equations discretization. Both steps are briefly described in the following sections, 3.2.1 and 3.2.2.

3.2.1 *Domain discretization*
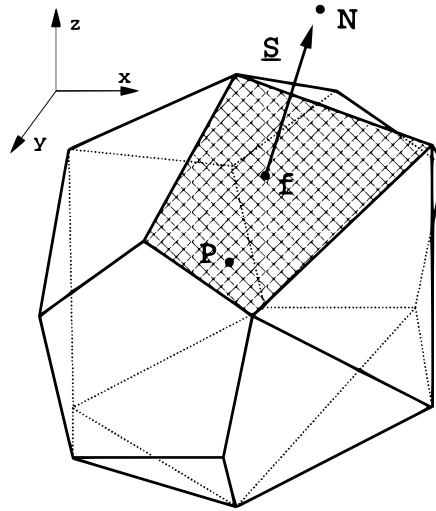
Figure 3.1: Control volume (Source: Jasak, 1996).

The domain discretization process for the Finite Volume Method (FVM) requires a given computational domain split into several control volumes (cells), e.g. see Fig. 3.1. This process is directly related to the meshing task which can be performed within the OpenFOAM® environment or by using a third-party software compatible. Note that in Fig. 3.1 the owner and a neighbour cell centres are labelled with $\mathbf{P}$ and $\mathbf{N}$, whereas $\mathbf{S}$ is the face area vector of the shaded face $\mathbf{f}$. Different kind of spatial discretizations depending on the different finite volume mesh topologies can be found: structured, block-structured and unstructured. The mesh topology may have a significant impact on the efficiency and accuracy of the solution as well as on the parallelization aspect.

Once the mesh is build, (3.1) and (3.2) are integrated over the control volumes to be solved. The divergence terms in (3.2) are computed by using the Gauss' theorem which converts them into flux terms integrated over cell surfaces. This manipulation makes easier the process as the problem is simplified to find difference approximations for the fluxes on the cell-surfaces, known the cell-center values (Weller et al., 1998).

3.2.2 *Equation discretization*

Once performed the domain discretization, the Navier–Stokes equations (3.1) and (3.2) can be discretized in OpenFOAM® by using a large number of numerical methods.

The OpenFOAM® toolbox converts the Navier–Stokes equations into a set of algebraic equations which can be written generically as

$$\mathbf{A}\boldsymbol{\Psi} = \mathbf{B},\tag{3.3}$$

being $\mathbf{A}$ the discretization matrix which holds the matrix coefficients, $\boldsymbol{\Psi}$ the vector of variables, and $\mathbf{B}$ the discretization source term including the boundary boundary conditions. The matrix $\mathbf{A}$ needs to be inverted in order to solve (3.3). Matrix inversions can be considered as a bottleneck when dealing with numerical methods as it is the most time consuming step when solving a given problem. This obstacle is solved in OpenFOAM® by using sparse block matrices, in particular $\mathbf{A}$ is build to be a lower-diagonal-upper matrix (see `lduMatrix` and `fvMatrix` classes within OpenFOAM®).

The nonlinear terms in (3.2) are first linearized and then solved iteratively until the convergence criteria are reached. The iterative process is done in an efficient manner as a result of the previous sparse matrix approach. A large list of numerical methods are implemented in the OpenFOAM® framework to treat properly the solution of the different terms in (3.1) and (3.2). But it is out of the scope of this thesis a deep review on the different numerical methods implemented in OpenFOAM® (see, e.g., OpenCFD, 2014, Marić et al., 2014). In any case, the numerical details used to solve each problem are collected in Chapters 4 and 5.

3.3 THE `icoFoam` SOLVER AND THE PISO ALGORITHM

As stated in the previous section, OpenFOAM® performs a linearization in order to compute the nonlinear convective term in (3.2). Hence, according to Jasak (1996), $\nabla \cdot (\mathbf{U}\mathbf{U})$ can be expressed as

$$\begin{aligned}
\nabla \cdot (\mathbf{U}\mathbf{U}) &= \sum_f S \cdot (\mathbf{U})_f (\mathbf{U})_f \\
&= \sum_f F(\mathbf{U})_f \\
&= a_P \mathbf{U}_P + \sum_N a_N \mathbf{U}_N,
\end{aligned}\tag{3.4}$$

where F, a_N, a_P are the fluxes of momentum through the faces, the matrix coefficient corresponding to the neighbour N, and the central coefficient, respectively. Note as well that the subscript f is related to the cell faces whereas N to the neighbours and P to the centroid of the cell. It is noteworthy that the fluxes F must satisfy the continuity equation (3.1).

The operator $\mathbf{H}(\mathbf{U})$ is introduced for the representation of the "temporal part" and the "source terms",

$$\mathbf{H}(\mathbf{U}) = -\sum_N a_N \mathbf{U}_N + \frac{\mathbf{U}^{n-1}}{\Delta t}. \tag{3.5}$$

Further information on the assembling of $\mathbf{H}(\mathbf{U})$ and mathematical manipulations of the momentum equations can be found in Jasak (1996).

1: **procedure** Predictor Step
2:     $\dfrac{\mathbf{U}^{n(*)} - \mathbf{U}^{n-1}}{\Delta t} + \nabla \cdot (\phi \mathbf{U}^{n(*)}) + \nabla \cdot (\nu \nabla \mathbf{U}^{n(*)}) = -\nabla p^{n-1}$
3: **end procedure**

4: **for** PISO loop **do**

5:     **procedure** First Corrector Step: solve the Poisson problem
6:         $\nabla \cdot [\nabla p^{n(*)}] = \nabla \cdot \mathbf{H}\left(\mathbf{U}^{n(*)}; \mathbf{U}^{n-1}\right)$
7:     **end procedure**

8:     **procedure** Second Corrector Step: explicit correction
9:         $\mathbf{U}^{n(**)} = \mathbf{U}^n(*) - \dfrac{1}{a_P}\nabla p$
10:     **end procedure**

11:     **if** convergence criteria reached **then**
12:         $\mathbf{U}^n = \mathbf{U}^{n(*)}$
13:         $p^n = p^{n(*)}$
14:         **break**
15:     **else**
16:         $\mathbf{U}^{n(*)} = \mathbf{U}^{n(**)}$
17:         **go to** 4
18:     **end if**
19: **end for**

Algorithm 1: PISO algorithm in OpenFOAM®.

On the other hand, since unsteady computations have been performed in the problems studied in this thesis, the predictor-corrector PISO method (Issa, 1985) is the choice of OpenFOAM® to deal with the pressure-velocity coupling in (3.1) and (3.2) when a temporal advancement is present. The algorithm is shown in Alg. 1 in the way it is implemented in OpenFOAM®, and can be summarized as follows:

- The momentum equation is solved first. As the pressure value of the present step is unknown, the value of the previous step is used instead. The solution of this step gives a new predicted velocity field.

- The operator $\mathbf{H}$ is assembled with the previous velocity estimate and the Poisson equation is solved. This step provides a new guess of the pressure field.

- The velocity field is corrected by using the previous pressure guess. From this step onwards the previous values of p and $\mathbf{U}$ are set as the $n-$th solutions if

the convergence criteria are satisfied. Otherwise, the algorithm returns to the previous step.

```cpp
// --- PISO loop

for (int corr=0; corr<nCorr; corr++)
{
    volScalarField rAU(1.0/UEqn.A());

    volVectorField HbyA("HbyA", U);
    HbyA = rAU*UEqn.H();
    surfaceScalarField phiHbyA
    (
        "phiHbyA",
        (fvc::interpolate(HbyA) & mesh.Sf())
        + fvc::interpolate(rAU)*fvc::ddtCorr(U, phi)
    );

    adjustPhi(phiHbyA, U, p);

    for (int nonOrth=0; nonOrth<=nNonOrthCorr; nonOrth++)
    {
        fvScalarMatrix pEqn
        (
            fvm::laplacian(rAU, p) == fvc::div(phiHbyA)
        );

        pEqn.setReference(pRefCell, pRefValue);
        pEqn.solve();

        if (nonOrth == nNonOrthCorr)
        {
            phi = phiHbyA - pEqn.flux();
        }
    }

    #include "continuityErrs.H"

    U = HbyA - rAU*fvc::grad(p);
    U.correctBoundaryConditions();
}
```

Listing 3.1: Code snippet of the PISO method in `icoFoam`.

Finally, as an example, the code snippet in List. 3.1 includes the PISO algorithm coded as in the `icoFoam` solver, which solves (3.1) and (3.2) for unsteady laminar incompressible fluid flows. It is remarkable that this solver has been used in each problem addressed in this thesis.

3.4 CONCLUDING REMARKS

A brief summary of the Finite Volume discretization technique implemented in Open-FOAM® is given in this chapter. It allows to solve the Navier–Stokes equations treating nonlinear terms by using a face addressing.

The basics of the domain discretization and matricial assembling followed in Open-FOAM® are summarized in subsections 3.2.1 and 3.2.2, respectively. The `icoFoam` solver and the PISO method are also described in section 3.3 for being used to solve

the problems studied in this thesis.

On the other hand, the different contributions appearing in the formulation by Chang (1992) have been computed at the runtime by coding `functionObjects` (see, e.g Stroustrup, 2013) within the OpenFOAM® environment. The drag and lift *densities* are essential when analyzing the flow field as they provide and intuitive and meaningful representation of the physics of the problem in terms of the volumetric force. Original discussions on the configuration of the vortical structures for the different thrust efficiency rates are shown in Chapters 4 and 5 by using this approach.

For further information on the OpenFOAM® framework the reader is addressed to Weller et al. (1998), Jasak (1996), Juretic (2004) and Jasak et al. (2007). See also Marić et al. (2014) for getting started with OpenFOAM® coding.

ON THE DEVELOPMENT OF LIFT AND DRAG IN A ROTATING AND TRANSLATING CYLINDER

4.1 INTRODUCTION

The flow around a rotating circular cylinder is a quite well studied fluid flow. Not only for its intrinsic interest, but also because its relative simplicity facilitates the understanding of several interesting phenomena associated with the interaction of a fluid with a moving solid surface. For instance, the mechanisms of the near-wake formation and the development of the von Kármán vortex street behind a rotating cylinder were analyzed by Coutanceau and Ménard (1985) and by Badr and Dennis (1985). The basic patterns of vortex shedding and its kinematics in an impulsively started rotating and translating circular cylinder were studied by Chang and Chern (1991) and Chen et al. (1993). Two-dimensional (2D) numerical simulations by Chew et al. (1995); Kang and Choi (1999); Stojković et al. (2002) and Mittal and Kumar (2003) showed, using quite different numerical approaches, that the von Kármán vortex shedding is suppressed when the rotation is high enough, depending on the Reynolds number Re. Particularly, Mittal and Kumar (2003), who carried out computations at Re = 200 for non-dimensional rotation rate γ in the range $0 \leq \gamma \leq 5$ (see next subsection for the definitions of Re and γ), showed that vortex shedding ceases when $\gamma \leq 1.9$, but reappearing again for $4.34 \leq \gamma \leq 4.7$ with a much lower frequency. This new vortex shedding mode for high γ was further analyzed by Stojković et al. (2003) for a wide range of Re, showing that the amplitudes of the fluctuating lift and drag coefficients are much larger than those characterizing classical vortex shedding, sometimes generating negative values for the mean drag, i.e. generating mean thrust. The instability mechanisms that trigger the first and second modes of vortex shedding in the 2D flow were analyzed by Pralits et al. (2010), identifying the region of the flow where the global instabilities were produced. The structure of the steady flow for very large values of γ was analyzed, also from 2D numerical simulations together with boundary-layer analysis, by Wang and Joseph (2006) and by Padrino and Joseph (2006) with the main aim of connecting it to the potential flow theory. Three-dimensional transitions were considered by El Akoury et al. (2008), and recently the three-dimensional instabilities in the wake behind the rotating cylinder have been investigated in a series of papers (Rao et al., 2013a; Rao et al., 2013b; Pralits et al., 2013; Radi et al., 2013). A very recent review of all these transitions in the wake of a rotating cylinder is given by Rao et al. (2015). In their Fig. 1 these authors present curves demarcating the regimes of instability for $0 \leq \text{Re} \leq 350$ and $0 \leq \gamma \leq 7$.

The interest of the rotating cylinder in aerodynamics and aeronautics for the generation of lift forces by the *Magnus effect* (Prandtl, 1926; see also Seifert, 2012 for a recent review, and references therein) is also well known. It is in this context that we consider here this flow, as a relatively simple model example to try to understand the generation, reduction or suppression of lift and drag in non-steady flows associated

with moving solid surfaces. For complex geometries and movements this is a hard task because of the intricate structures of the associated unsteady three-dimensional flow. However, the two-dimensional flow structures around a rotating cylinder for relatively low Reynolds numbers are more easily analyzed. To identify the vortex elements associated with the generation and development of lift and drag we use the vorticity formulation originally developed by Chang (1992), as already done for other simple models (e.g., Hsieh et al., 2009, Hsieh et al., 2010, Lee et al., 2012). This is even more interesting in the case of the rotating and translating cylinder because the lift can be increased substantially by increasing the rotation rate, changing also from oscillatory to steady, while the drag may decrease substantially to almost vanishing, so that one might gain insight on the flow structures that generate lift and on those that reduce drag. This insight could be applied to understand the mechanisms of lift enhancement and drag reduction in more complex body shapes, especially for rotating bodies (e.g., Jimémenez-González et al., 2013).

4.2 FORMULATION OF THE PROBLEM

We consider here the two–dimensional unsteady incompressible flow around a rotating cylinder. In particular, we analyze two different unsteady flow problems: (i) Starting with the flow of a uniform stream of speed U_0 around a static cylinder of radius a (or a cylinder translating with a constant speed U_0 in a fluid at rest), study the unsteady flow generated by the rotation of the cylinder from rest to a final angular velocity Ω_0 during an interval of time t_c , and (ii) starting from a rotating cylinder with an angular velocity Ω_0 in a fluid at rest, analyze the unsteady flow generated by the moving cylinder from rest until it reaches a final velocity U_0 in a time t_c.

Using the radius a of the cylinder and the steady-state free stream speed U_0 as the reference length and velocity, respectively, the non-dimensional Navier-Stokes equations and boundary conditions governing the incompressible flow in the reference frame moving with the cylinder of Fig. 4.1 can be written as

$$\nabla \cdot \mathbf{v} = 0, \tag{4.1}$$

$$q\frac{\partial}{\partial t}(\mathbf{v} - U\mathbf{e}_x) + \mathbf{v} \cdot \nabla\mathbf{v} = -\nabla p + \frac{2}{\text{Re}}\nabla^2\mathbf{v}, \tag{4.2}$$

subject to

$$|\mathbf{x}| \to \infty, \quad \mathbf{v} \to U(t)\,\mathbf{e}_x, \quad p \to 0, \tag{4.3}$$

$$|\mathbf{x}| = 1, \quad \mathbf{v} = -\gamma\Omega(t)\,\mathbf{e}_\theta, \tag{4.4}$$

where $\mathbf{v}$ is the non-dimensional velocity, p is the non-dimensional relative pressure (scaled with ρU_0^2, being ρ the fluid density), and $\mathbf{e}_x$ and $\mathbf{e}_\theta$ are the unit vectors in the direction of the free stream velocity and in the azimuthal direction, respectively (see Fig. 4.1).
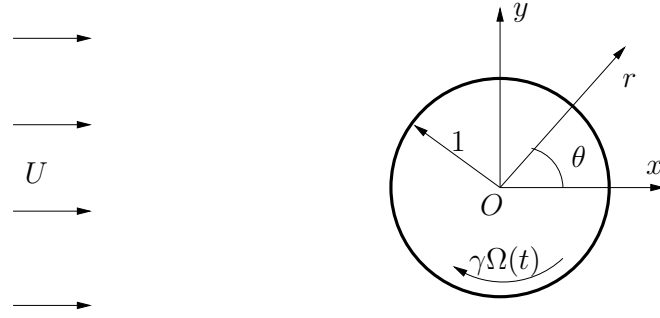
Figure 4.1: Sketch of the non-dimensional geometry and coordinates.

In the above equation we have defined the following non-dimensional parameters:

$$\mathrm{Re} = \frac{\rho U_0 2a}{\mu}, \quad \gamma = \frac{\Omega_0 a}{U_0}, \quad q = \frac{a}{t_c U_0}, \tag{4.5}$$

i.e., a Reynolds number based on the diameter $2a$, a rotation rate parameter and an acceleration parameter, respectively, with μ being the fluid viscosity. The dimensionless functions U and ω in the cases (i) and (ii) described above can be written as:

$$(i) \quad U = 1, \quad \Omega(t) = \begin{cases} t, & 0 \le t < 1 \\ 1, & t \ge 1, \end{cases} \tag{4.6}$$

$$(ii) \quad \Omega = 1, \quad U(t) = \begin{cases} t, & 0 \le t < 1 \\ 1, & t \ge 1, \end{cases} \tag{4.7}$$

where a linear increase of the angular velocity and of the free stream velocity, respectively, have been assumed in each case. Note that U and Ω are obtained from the dimensional free stream velocity and the dimensional angular velocity divided by the characteristic velocity U_0 and the characteristic angular velocity Ω_0, respectively. Thus, γ, defined in (4.5), is the dimensionless parameter resulting from scaling Ω_0 with the characteristic velocity and the characteristic length. The actual boundary conditions implemented numerically in the computational domain (Fig. 4.2, see also next section) are the following:

$$\mathbf{v}(\mathbf{x}, t) = U(t)\mathbf{e}_x, \quad \mathbf{x} \in \Sigma_i, \tag{4.8}$$

$$\mathbf{v}(\mathbf{x}, t) = -\gamma\Omega(t)\mathbf{e}_\theta, \quad \mathbf{x} \in \Sigma_w, \tag{4.9}$$

$$\mathbf{n} \cdot \mathbf{v} = 0, \quad \mathbf{x} \in \Sigma_s, \tag{4.10}$$

$$p(\mathbf{x}, t) = 0, \ \mathbf{n} \cdot \nabla \mathbf{v}(\mathbf{x}, t), \quad \mathbf{x} \in \Sigma_o, \tag{4.11}$$

treating the pressure implicitly by means of the incompressibility condition (4.1) at Σ_i, Σ_w and Σ_s. The initial conditions ($t = 0$) for solving (4.1)–(4.7) are those corresponding to the fully developed flow with $U = 1$ and $\Omega = 0$ in the case (i), and $U = 0$

and $\Omega = 1$ in the case (ii) (see next section for further numerical details).
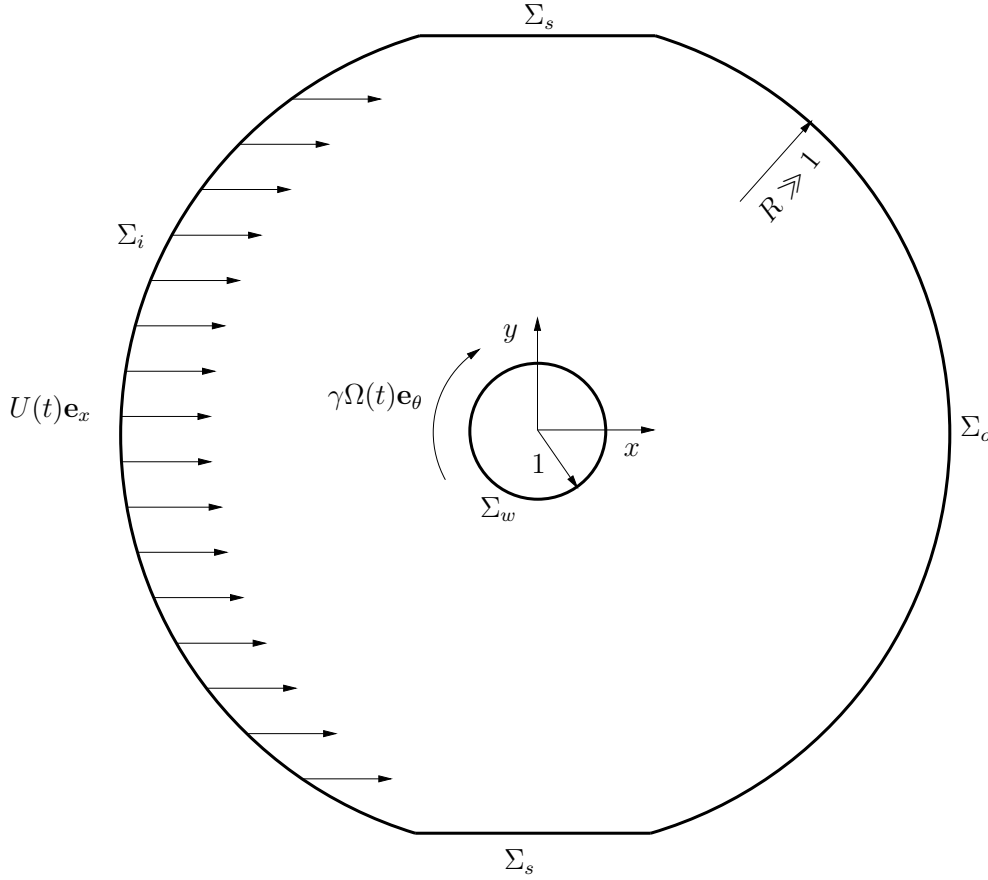
Figure 4.2: Sketch of the non-dimensional computational domain.

For the sake of clarity, the reader is referred to Chapter 2 where the formulation related to the vortex force decomposition of Chang (1992) is gathered.

4.3   NUMERICAL METHOD

Equations (4.1) and (4.2) were solved numerically with the software OpenFOAM® within a computational domain already used by Padrino and Joseph (2006), i.e. with an 'O-type' mesh as shown in Fig. 4.2. OpenFOAM® is an open source Computational Fluid Dynamics (CFD) software based on the finite volume method, which has been validated with success in some previous numerical works (e.g., Muñoz-Esparza and Sanmiguel-Rojas, 2011; Sanmiguel-Rojas and Mullin, 2012; Martín-Alcántara et al., 2014). The reader is referred to Chapter 3 for further information on the Open-FOAM® framework.

For the spatial discretization we used second order accuracy linear interpolation for the diffusion term, and a Total Variation Diminishing scheme, TVD, with a van Leer limiter, for the convection term. This hybrid scheme is set in order to avoid numerical oscillations in grid regions where local mesh Reynolds number is high (far field in ra-

dial coordinates, since cells are clustered around the body to improve resolution within the boundary layer and near wake zones) and convection dominates over diffusion. On the other hand, the temporal discretization was performed by blending a second order Crank-Nicolson scheme with implicit Euler integration, to ensure boundedness of the solution. Moreover, the pressure-velocity coupling has been treated through the pressure-implicit split-operator (PISO) algorithm (Issa, 1985), using a small temporal step to keep the Courant number CFL ≤ 0.6.

Table 4.1 shows the properties of the different meshes considered in the numerical computations. The dimensionless domain radius R varied between 30 and 250. Two different cell sizes were used for $R = 150$, as characterized by the radial step size of the first layer of cells attached to the wall, h_r^1. The number of cells around the cylinder $r = 1$, N_a was 160 for the coarse mesh, with $h_r^1 = 0.005$, and $N_a = 220$ for the fine mesh, with $h_r^1 = 0.0025$. The total number of cells varied between 15 680 and 42 848. The time step Δ was selected such that the Courant number was always less than 0.6. Note that the mesh with $R = 150$ is reported with two different time steps.

Mesh	Nodes	Cells	N_a	H	h_r^1	Δt
1	31 680	15 680	160	30	0.005	0.00625
2	44 160	21 920	160	100	0.005	0.00625
3	48 320	24 000	160	150	0.005	0.00625
4	51 520	25 600	160	200	0.005	0.00625
5	53 760	26 720	160	250	0.005	0.00625
6	48 320	24 000	160	150	0.005	0.003125
7	86 112	42 848	220	150	0.0025	0.003125

Table 4.1: Properties of the meshes considered in the numerical simulations (see main text).
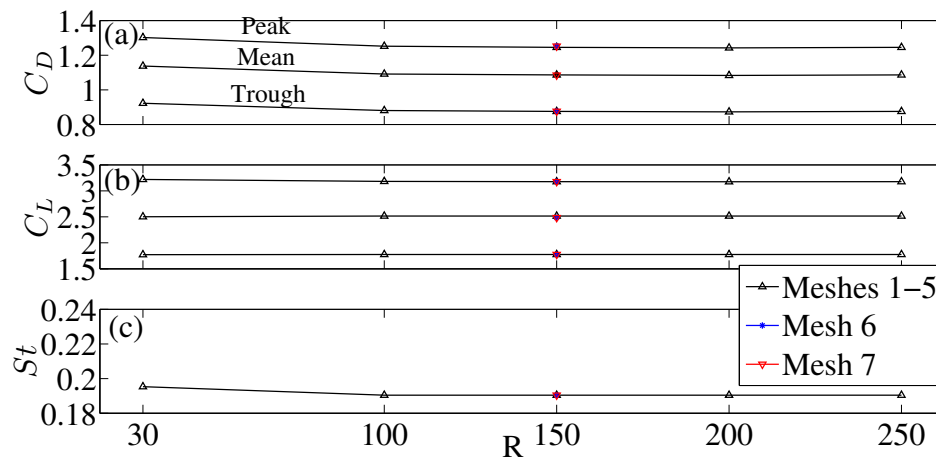
Figure 4.3: Influence of the dimensionless radius of the outer boundary R on the lift, drag and non-dimensional frequency of the vortex shedding for Re = 200 and $\gamma = 1$. Meshes are defined in Table 4.1 (meshes 6 and 7 are both with $R = 150$).
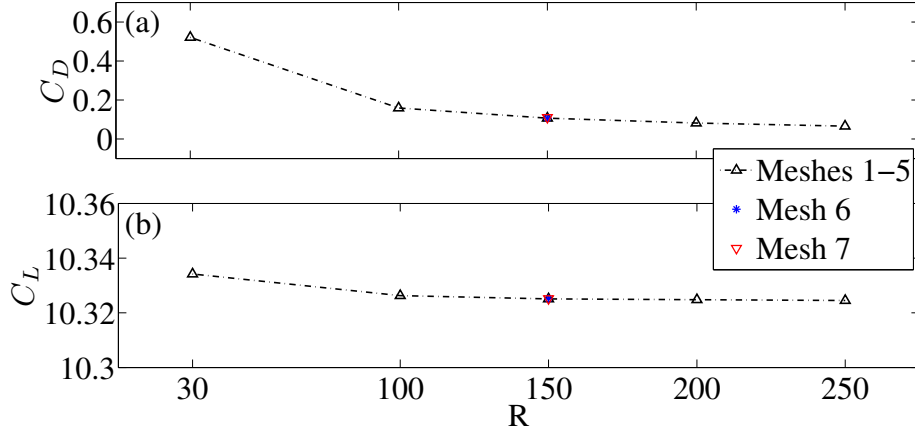
Figure 4.4: Influence of the dimensionless radius of the outer boundary R on the lift, drag and
non-dimensional frequency of the vortex shedding for Re = 200 and $\gamma = 3$. Meshes
are defined in Table 4.1 (meshes 6 and 7 are both with $R = 150$).

Figs. 4.3 and 4.4 show the influence of the computational domain size R and the
mesh size on the large time results for C_L and C_D for Re = 200, which is the selected
Reynolds number for all the results reported below, $\gamma = 1$ and $\gamma = 3$, respectively. The
computations were started at $t = 0$ from the potential flows corresponding to these
values of γ , with $U = 1$ and $\Omega = 1$ for $t \geq 0$. When $\gamma = 1$ (Fig. 4.3), the long time
results for C_L and C_D oscillate with the period T of the vortex shedding behind the
cylinder (see below), and Fig. 4.3 (c) shows the Strouhal number $St = 2a/(U_0 T)$ of
these oscillations to check also the accuracy of the temporal evolution of the numerical
solutions. Fig. 4.3 (a) and (b) shows the final mean values of C_L and C_D together with
their values at the peaks and troughs of these oscillations. On the other hand, for $\gamma = 3$
(Fig. 4.4), a steady state is reached without vortex shedding [the von Kármán vortex
street ceases at $\gamma \simeq 1.91$ for Re = 200 (see Mittal and Kumar, 2003), so that Fig. 4.4
(a) and (b) reports only the final mean values of C_L and C_D.

These figures show that the mesh 3 ($R = 150$, 24000 cells) with $\Delta t = 0.00625$ is
enough to obtain very accurate results for this Reynolds number and this range of
values of γ, both for the steady state and for the oscillatory results. To reinforce this,
Figs. 4.5 and 4.6 compare our numerical results for C_L and C_D obtained with this
mesh for Re = 200, $\gamma = 0$; 1; 3, with those obtained by Mittal and Kumar (2003)
for the same cases. In particular, Fig. 5 shows $C_L(t)$ and Fig. 4.6 the phase diagrams
of C_L and C_D for the fully developed flow. The agreement is very good in all cases
except for C_D when $\gamma = 3$ (Fig. 4.6). This is due to the fact that C_D is too small
compared to C_L in this case (see also Fig. 4) and the relative errors may become quite
large (as noted also by Padrino and Joseph, 2006 in their Table 2, where they report
large differences in the computed C_D in this case). But the difference in the total force
coefficient $\sqrt{C_L^2 + C_D^2}$ between our results and those by Mittal and Kumar (2003) is
negligible. Note also that for $\gamma = 0$ there exists a phase shift in $C_L(t)$ (Fig. 4.5), which
is probably due to the different numerical methods, that trigger the instabilities giving

rise to the vortex shedding at different times. But the amplitude and the frequency of the oscillations due to the vortex shedding are practically the same, as corroborated in the phase diagram of Fig. 4.6 and the Strouhal numbers given in the caption.

4.4 RESULTS AND DISCUSSION

4.4.1 *Preliminary study for $\gamma = 0$*

First we consider the case without rotation ($\gamma = 0$) for a fixed free stream speed corresponding to Re = 200. Fig. 7 shows the time histories of C_D and C_L when the numerical simulations are started at $t = 0$ from the corresponding potential flow.
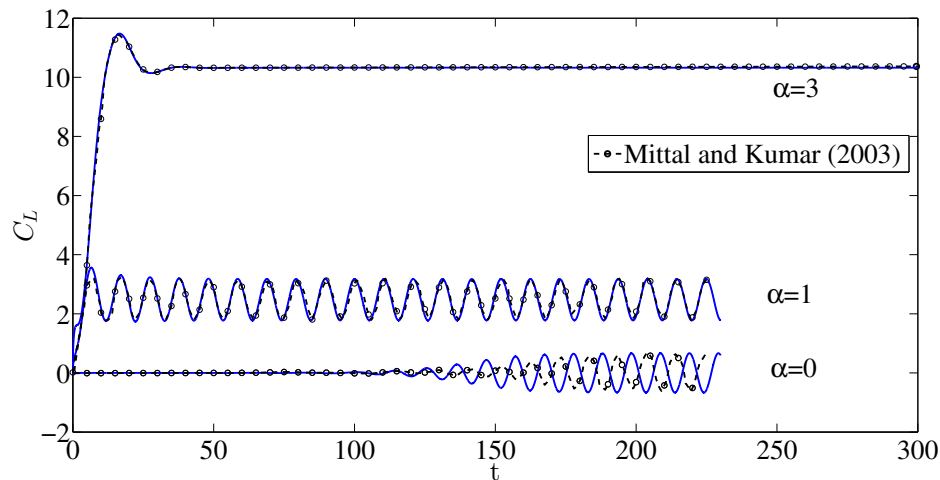
Figure 4.5: Time histories of C_L for Re = 200 and several values of γ (as indicated) computed with mesh 3 with $\Delta t = 0.00625$ (continuous lines), and comparison with the results by Mittal and Kumar (2003) for the same cases (dashed lines with open circles). Strouhal numbers [Mittal and Kumar, 2003]: for $\gamma = 0$, $St = 0.1904$ [0.1934]; for $\gamma = 1$, $St = 0.1904$ [0.192].

The curves for both C_D and C_L are practically indistinguishable when computed from (2.13) and (2.14) or from (2.17) and (2.15). Thus, in all the results reported below C_L and C_D are always computed through (2.17) and (2.15), respectively. Fig. 4.8 shows the contributions of the volume and surface integrals to C_D and C_L, where it is observed that the contributions of the volume integrals are significantly larger than the corresponding contributions of the surface integrals. A note of warning should be given here: as we see in all the reported results, while C_{Ls} is always significantly smaller than C_{Lv}, C_{Ds} is frequently comparable to C_{Dv}. Therefore, while the analysis of the lift force based on its volume elements δ_{Lv} yields always a whole quantitative picture of the lift generation and evolution, the analysis based on δ_{Dv} sometimes only accounts for a fraction of C_D. In any case, it is relevant to map the δ_{Dv} and δ_{Lv} fields to find out the structures of the flow that contribute positively or negatively to the drag and to the lift forces, respectively.
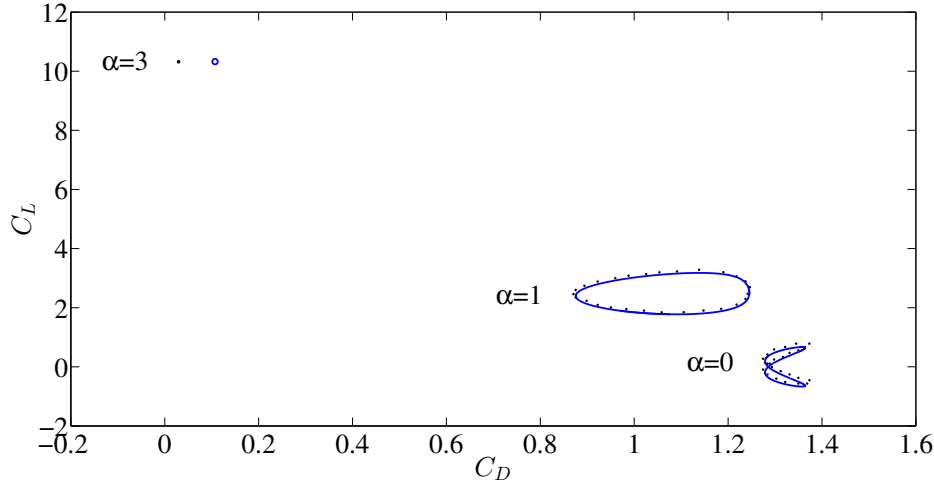
Figure 4.6: Phase diagrams of C_L and C_D for the same cases of Fig. 4.5 (continuous lines and open circle in the case of $\gamma = 3$), and comparison with the results by Mittal and Kumar (2003) (dots).
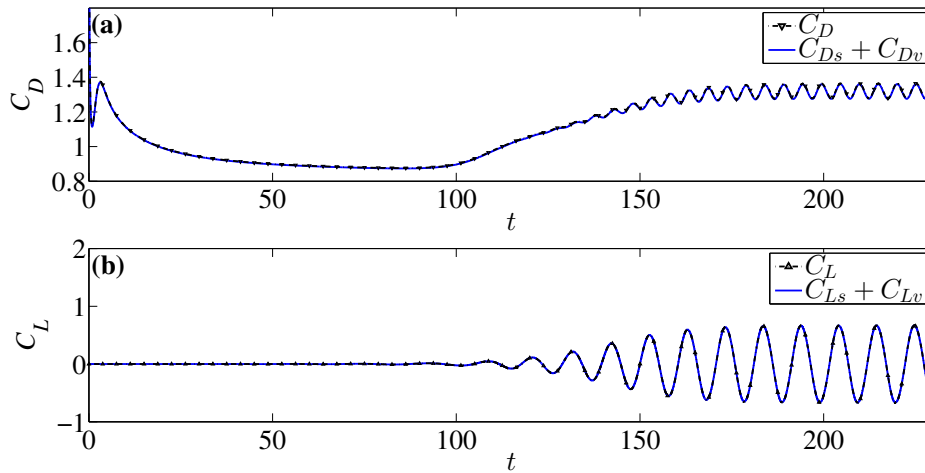
Figure 4.7: Time histories of C_D (a) and C_L (b) for Re $= 200$ and $\gamma = 0$ with $q = 1$ computed from the standard surface integrals (2.13) and (2.14) (dashed-and-dotted lines with symbols), and with the formulation given by (2.17) and (2.15) (continuous lines).

Fig. 4.9 shows that these fields at four instants of time corresponding to the maximum and minimum values of C_L and C_D once the fully developed oscillatory flow is reached for $\gamma = 0$. In particular, at $t = 219.6$ and $t = 224.7$, where C_L is a minimum and a maximum, respectively, and at $t = 220$ and $t = 222.6$, where C_D is a maximum and a minimum, respectively (see insets in Fig. 4.8). Note in Fig. 4.8 that C_{Ls} and C_{Lv} are slightly out of phase: although the oscillations in C_{Lv} are fully controlled by vortex shedding (see below), it is not necessarily so for the component of C_{Ls} due to surface friction. In order to visualize the vortex structure of the flow, we have also superposed in Fig. 4.9 the velocity gradient tensor field characterized by the so-called $Q-$value (Hunt et al., 1998) which for an incompressible flow can be
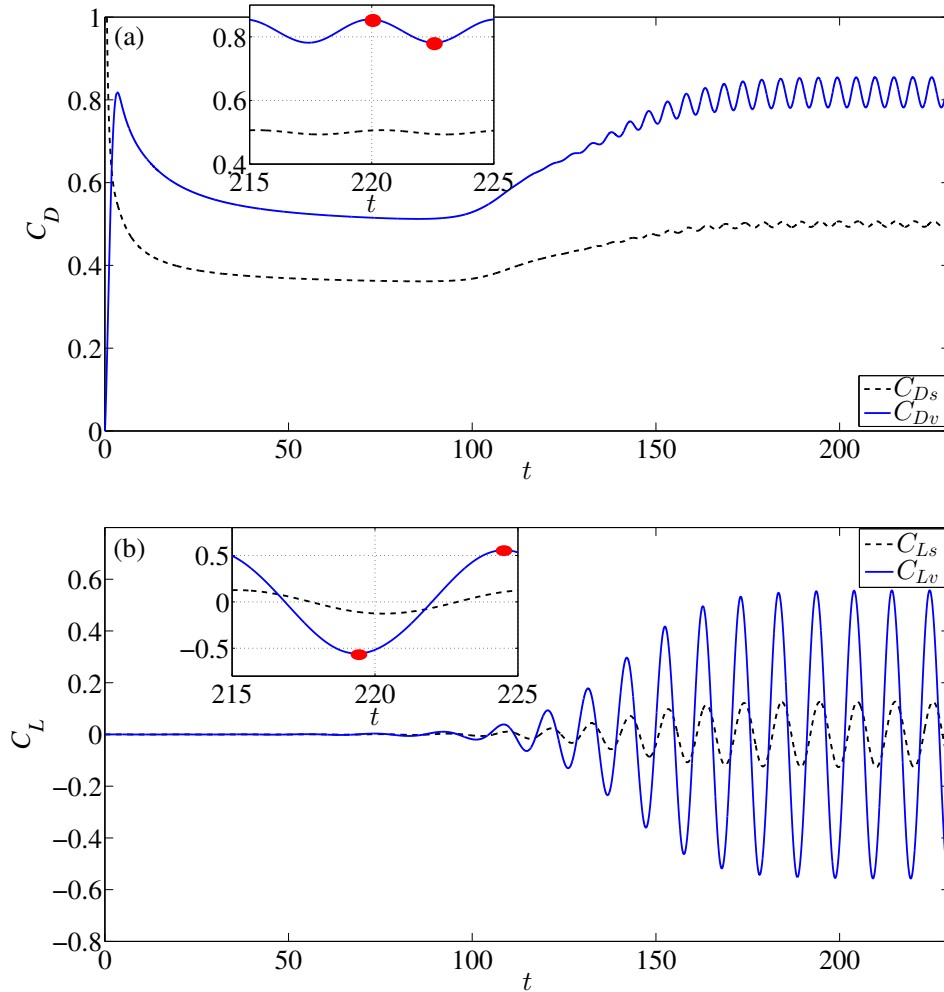
Figure 4.8: Comparison when $\gamma = 0$ between the time histories of C_{Dv} and C_{Ds} (a) and between the time histories of C_{Lv} and C_{Ls} (b) for the same case of Fig. 4.7. The insets are zooms of the fully developed flow and the filled circles correspond to the instants of time plotted in Fig. 4.9.

written as $Q = \|\boldsymbol{\omega}\|^2 - \|\mathbf{S}\|^2$, where $\boldsymbol{\omega} = [\nabla\mathbf{v} - (\nabla\mathbf{v})^T]/2$, $\mathbf{S} = [\nabla\mathbf{v} + (\nabla\mathbf{v})^T]/2$, and $\|\mathbf{A}\|^2 = \mathrm{tr}[\mathbf{A}\mathbf{A}^T]^{1/2}$. This $Q-$value identifies the coherent structures of the flow, and we find that in the present example it provides a clearer visualization of the vortex structures than the vorticity field itself (although this is not always the case, see below).

Fig. 4.9 (a) and (b) shows that the positive and the negative lift are generated by the upper and lower counter-rotating vortices, respectively, just in the front region close to the cylinder surface where these vortices are generated and shed. These are low pressure regions. The lift reaches a maximum ($t = 224.7$) when the upper clockwise vortex is developing and starts shedding from the cylinder while the lower counter-clockwise vortex is already almost detached from the cylinder [Fig. 4.9 (b)]. This configuration corresponds to a maximum of the positive lift elements in the upper front of the cylinder and a minimum of the negative lift elements in the lower front of the cylinder. Conversely, the lift reaches a minimum at $t = 219.6$ [Fig. 4.9 (a)] when the upper
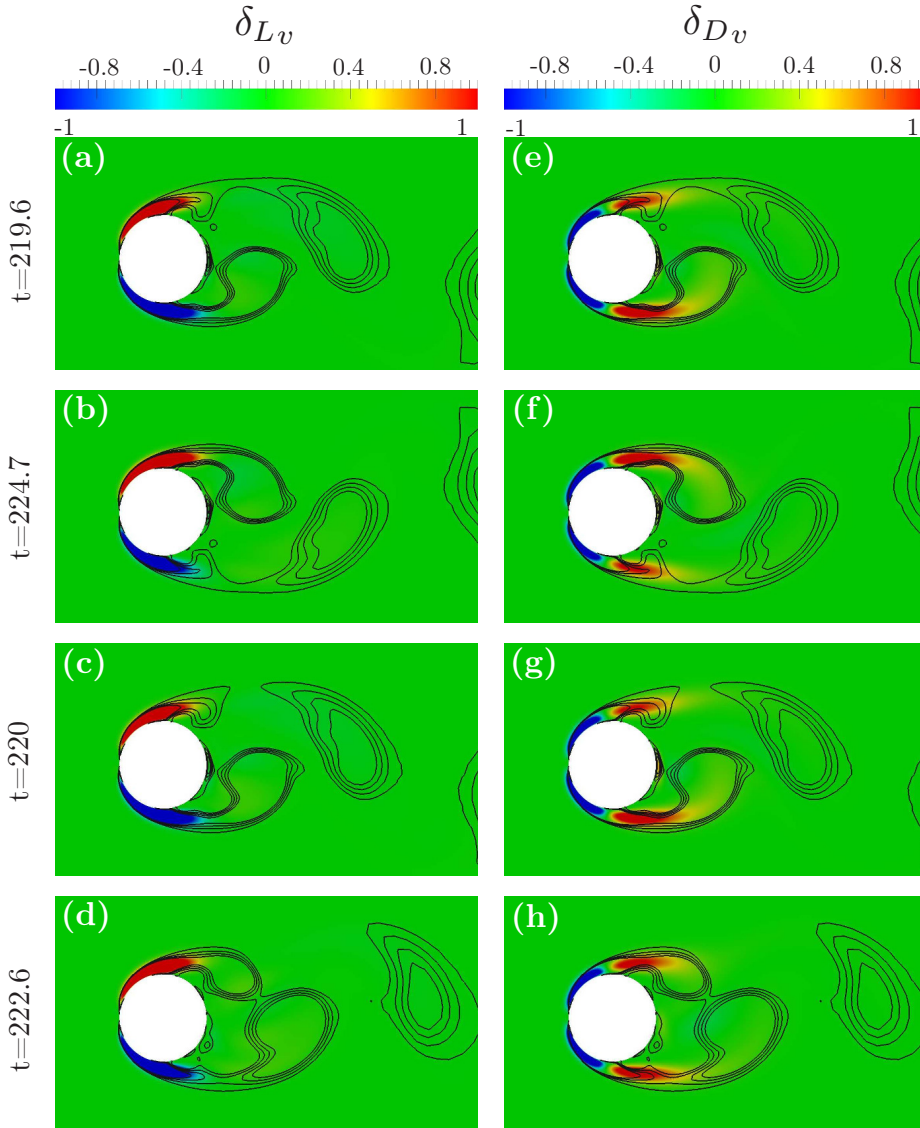
Figure 4.9: Contours of constant Q criterion (solid lines) superimposed to the fields of δ_{Lv} (panels (a)–(d)), and of δ_{Dv} (panels (e)–(h)) at four instants of time (marked in Fig. 4.8) corresponding to minimum and maximum lift (panels in the two top rows, respectively), and to maximum and minimum drag (panels in the two bottom rows, respectively), for Re = 200 and $\gamma = 0$. The contours of Q are for 0.005; 0.105; 0.205 and 0.305. $\lambda_L = 0.6978$ (a), 1.1359 (b), 0.6978 (c), 1.1359 (d); $\lambda_D = 1.9109$ (e), 1.9101 (f), 1.9138 (g), and 1.8355 (h).

vortex is detaching from the cylinder and the lower vortex is developing. On the other hand, the positive drag is also generated by these vortices but in the wake region, where they are shed from the cylinder. The maximum drag at $t = 220$ [Fig. 4.9 (g)] corresponds to a flow configuration close to that of minimum lift, while the minimum drag at $t = 222.6$ [Fig. 4.9] is close to the configuration with maximum lift. The main difference between them resides in the extension of the regions with positive drag elements. Note, however, that C_D is always positive and its oscillations represent a small fraction of its mean value [see Fig. 4.7 (a) or Fig. 4.8 (a)]. The mean lift is zero in this case with $\gamma = 0$, so that their positive and negative fluctuations are much better

characterized by the positive and negative lift volume elements than the drag is by its positive and negative drag volume elements.

To better quantify the total positive and negative volume elements contributing to the lift and drag in each case, we define new quantities that take into account the positive and negative parts of the integrals C Lv and C_{Dv} separately:

$$\lambda_L = \frac{C_{Lv}^+}{|C_{Lv}|^-}, \quad \lambda_D = \frac{C_{Dv}^+}{|C_{Dv}|^-} \tag{4.12}$$

Figure 4.10: Time histories of C_D (a) and C_L (b) for Re = 200, q = 1 and $\gamma = 1$ computed with (2.17) and (2.15), together with their components C_{Ds}, C_{Dv} and C_{Ls}, C_{Lv}. The filled circles correspond to the instants of time plotted in Fig. 4.11.

where C_{Lv}^+ is computed with the elements where $\delta_{Lv} \geq 0$ and C_{Lv}^- with those where $\delta_{Lv} < 0$, and similarly for C_D (of course, $C_{Lv} = C_{Lv}^+ + C_{Lv}^-$ and $C_{Dv} = C_{Dv}^+ + C_{Dv}^-$). The values of these quantities λ_L and λ_D are given in the caption of Fig. 4.9 for each instant of time plotted, and they are also given in all similar figures reported in subsequent sections. $\lambda_L > 1$ means that the positive volume contributions to the lift are larger than the negative ones, and similarly for λ_D.

4.4.2 Case (i)

We first present results for the case (i), i.e. when the (non-dimensional) free stream velocity is set to unity and the cylinder starts rotating at $t = 0$ with a given angular acceleration characterized by an acceleration parameter q until the non-dimensional angular velocity reaches a given value γ. As initial condition we start the numerical computation from the numerical results for $\gamma = 0$ when $C_L = 0$ once the fully developed oscillatory flow has been reached (for instance, from $t = 233.5$ in Fig. 4.7, which is then reset to $t = 0$ when the cylinder starts rotating). All the force coefficients are computed with (2.17) and (2.15). The reported results are for Re = 200 with $\gamma = 1$ and $\gamma = 3$.

4.4.2.1 $\gamma = 1$

Fig. 4.10 shows the temporal evolutions of C_D and C_L for $\gamma = 1$ when $q = 1$. Also their components C_{Ds}, C_{Dv} and C_{Ls}, C_{Lv} are included. As noted above, the volume components are larger than the surface ones, specially for C_L, so that the δ_{Lv} field will provide a convenient picture of the flow structures generating lift forces on the cylinder. It is observed in Fig. 4.10 that in this case with $\gamma = 1$, like in the case with $\gamma = 0$ (see Fig. 4.5), the fully developed flow oscillates due to vortex shedding, with a non-dimensional period of about 10 ($St = 0.1904$). Since $q = 1$, the duration of the initial transient in the rotating cylinder is much shorter than the period of the von Kármán vortex street (about 10 times shorter). Using larger transients (smaller q) would just delay the fully developed flow, but at the end one will obtain the same oscillatory flow. Therefore, we shall only present here results for $q = 1$ (other values of q will be considered below if they are more convenient to analyze the initial transient flow).

In particular, we plot in Fig. 4.11 the structures of the flow together with the δ_{Dv} and δ_{Lv} fields at $t = 0$, and at several instants of time where C_D and C_L reach their extreme values both in the initial transient and in the fully developed flow (see Fig. 4.10): $t = 3.2$; 23.4, and 28.2 for C_D and $t = 9$; 25.8, and 30.8 for C_L. Since we start at $t = 0$ with $\Omega = 0$ in a configuration with zero lift, the regions with non-vanishing lift volume elements in the upper front of the cylinder (positive) and in the lower front of the cylinder (negative) are of the same size and intensity, so that they cancel each other [see Fig. 11(a)]. This fact is quantified with $\lambda_L \simeq 0$ (the values of λ_L and λ_D in each case are given in the caption of Fig. 4.11). As the main difference with the case $\gamma = 0$ discussed above, now the upper front region generating positive lift is always more intense and larger than the lower front region generating negative lift, so that C_L is always positive [Fig. 4.10 (b); $\lambda \simeq 3.6$]. This is due to the fact that the clockwise rotation of the cylinder reinforces the upper clockwise vortex, while it weakens and slightly detaches from the cylinder the lower counter-clockwise vortex, as can be seen from the contours of constant Q−value plotted in Fig. 4.11. The positive (negative) lift volume elements are in the frontal region where this upper (lower) vortex is generated. Initially, this upper vortex grows in intensity, and so increases the intensity and size of the positive lift element, until the vortex reaches a maximum intensity just before it is shed from the cylinder, generating a separate vortex at $t = 9$ [Fig. 4.11 (b)] that travels downstream. As a consequence, the intensity of the upper vortex decays, and so does the intensity of the corresponding positive lift element until it reaches a minimum value. Then the vortex intensity, and that of the positive lift element, grows again due to the interplay between the flow and the rotation of the cylinder until it is again shed from the cylinder, and so on. This process generates the oscillation in C_L. In addition, there is a narrow region of positive lift generation between the lower surface of the cylinder and the detached lower vortex. Fig. 4.11 (c) shows a configuration of minimum lift, where the upper vortex has reached its lower intensity before it begins to grow again. Fig. 4.11 (d) shows the configuration of the next maximum lift, which is similar to that in Fig. 4.11 (b), but with slightly larger λ_L (and, of course, C_L).

In relation to the drag [Fig. 4.11 (e) and (h)], the configurations are similar to the case with $\gamma = 0$, with the main volume elements of positive drag located in the rear
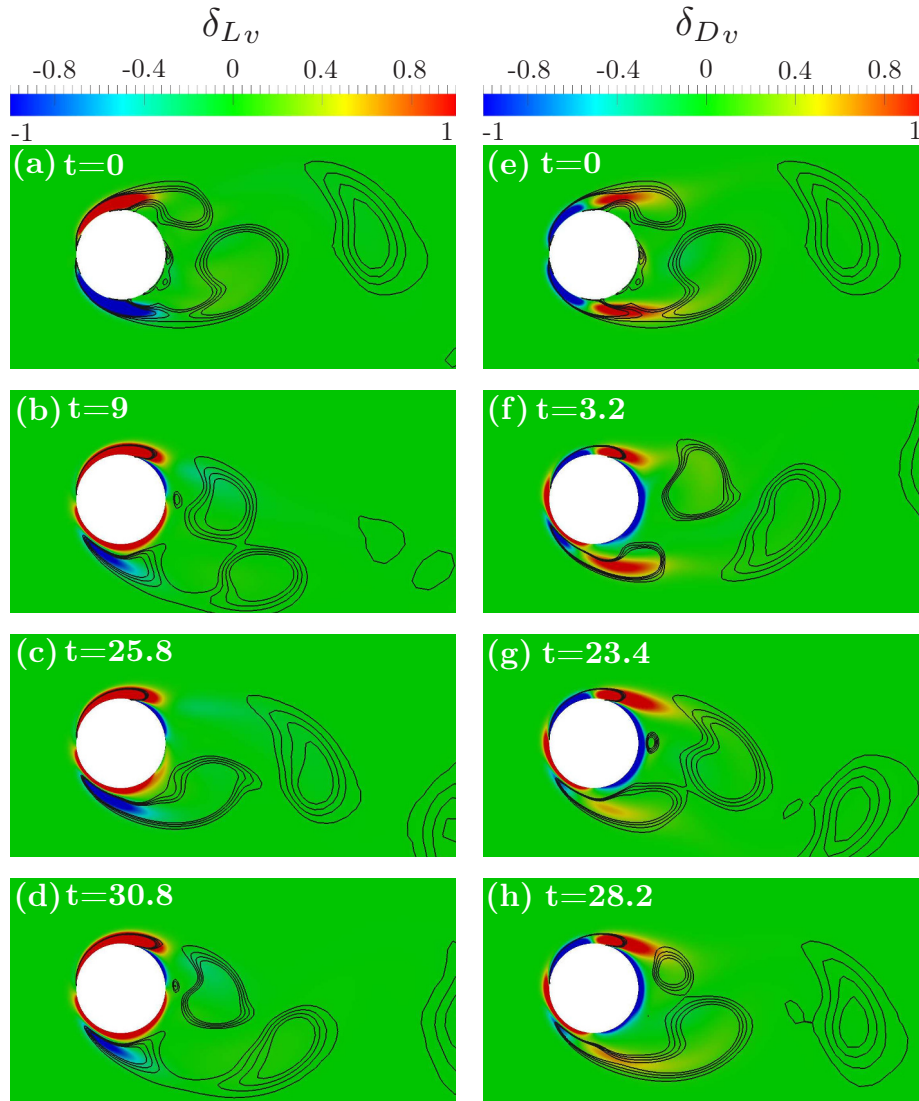
Figure 4.11: Contours of constant Q (solid lines) superimposed to snapshots of δ_{Lv} (left panels), and of δ_{Dv} (right panels), at $t = 0$ and at the instants of time (marked in Fig. 4.10) corresponding to extreme values of C_L and C_D, respectively, for Re = 200 and $\gamma = 1$ with $q = 1$. The contours of Q are for 0.005; 0.105; 0.205 and 0.305. $\lambda_L = 1.0056$ (a), 3.6021 (b), 2.3464 (c), 4.1395 (d); λ_D 1.8453 (e), 1.7076 (f), 1.2539 (g), and 1.5208 (h).

parts of both upper and lower vortices. But now, due to the rotation of the cylinder, there is a new significant source of positive drag on the cylinder's front, caused by the interplay between the clockwise rotation of the cylinder and the counter-clockwise rotation of the lower vortex that generates a high pressure region [compare Fig. 4.11 (f) and (h) with Fig. 4.11(e)]. This interplay between the rotation and the shedding vortices generates an intense source of negative drag on the upper front of the cylinder and another one of less intensity on the rear surface of the cylinder. The global effect is that the mean drag is slightly reduced in the fully developed flow in relation to the case without rotation (see Fig. 4.6). The oscillations are generated by the vortex shedding, as in the case of the lift, but they are not in phase: the maximum drag takes place just
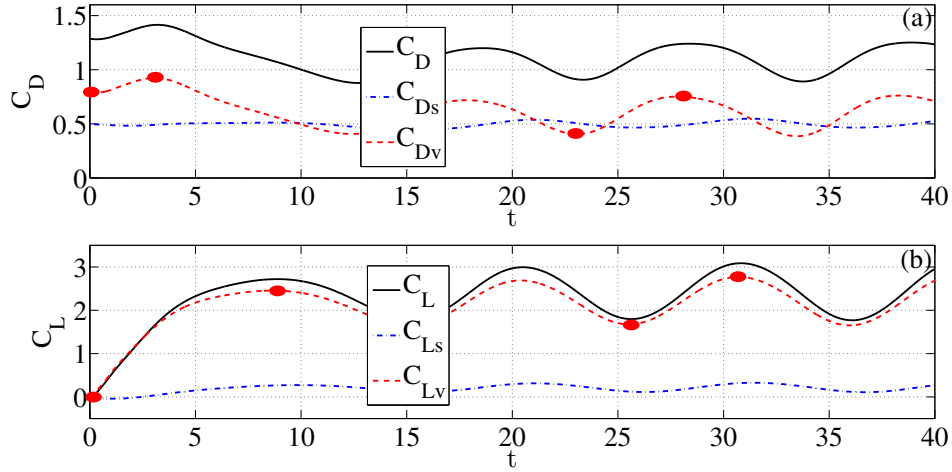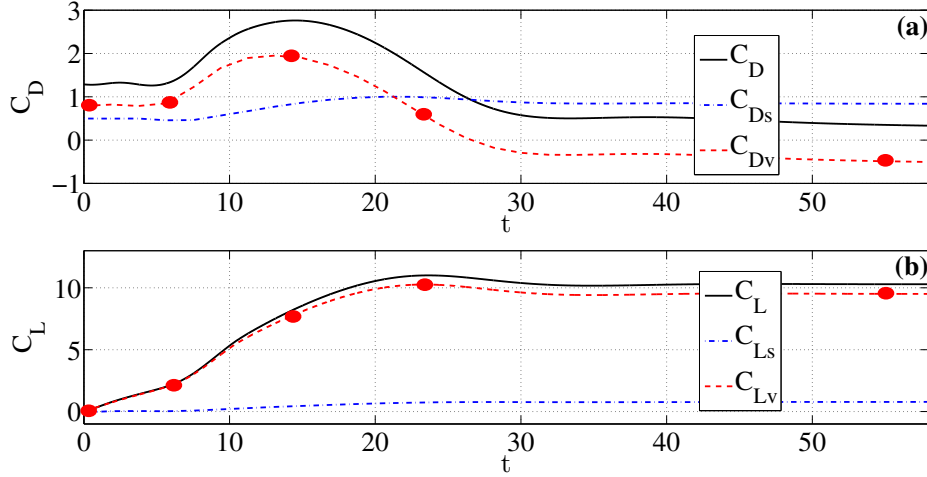
Figure 4.12: Time histories of C_D (a) and C_L (b) for Re=200, $q = 0.1$ and $\gamma = 3$ computed
with (2.17) and (2.15), together with their components C_{Ds}, C_{Dv} and C_{Ls}, C_{Lv}.
The filled circles correspond to the instants of time plotted in Fig. 4.13.

before the lift reaches a maximum, i.e. just before the upper vortex is shed [Fig. 4.11
(h)], and the minimum drag occurs just before the minimum lift, i.e. just before the
minimum intensity of the upper vortex is reached [Fig. 4.11 (g)].

4.4.2.2 $\gamma = 3$

As a difference with the case $\gamma = 1$ just reported, we now use $q = 0.1$ for $\gamma = 3$, so
that the transient from $\Omega = 0$ to $\Omega = 1$ is 10 times longer than in the previous case,
roughly of the order of the vortex shedding period reported above for $\gamma = 0$ and 1.
With this longer initial transient one can better appreciate the mechanisms by which
the vortex shedding (and the von Kármán vortex street) is suppressed in this case
with $\gamma = 3$. The numerical computation is started, as in the previous cases, from the
numerical results for $\gamma = 0$ when $C_L = 0$, once the fully developed oscillatory flow has
been reached. Fig. 4.12 shows the temporal evolutions of C_D and C_L. Now, both C_D
and C_L reach non-oscillatory steady state values, with almost vanishing C D due to the
negative contribution of its volume part C_{Dv}, and a quite large final C_L coming almost
entirely from its volume contribution C_{Lv}. To explain these interesting and different
features in relation to the previous case, we plot in Fig. 4.13 the structures of the flow
at several relevant instants of time, together with the δ_{Dv} and δ_{Lv} fields. We now use
the distribution of (axial or $z-$component) vorticity instead of the $Q-$value to char-
acterize the vortex structures because, as we shall see, it is important to differentiate
the clockwise from the counter-clockwise vortices, i.e. negative from positive (axial)
vorticity.

Fig. 4.12 shows the temporal evolutions of C_D and C_L. Now, both C_D and C_L reach
non-oscillatory steady state values, with almost vanishing C_D due to the negative con-
tribution of its volume part C_{Dv}, and a quite large final C_L coming almost entirely
from its volume contribution C_{Lv}. To explain these interesting and different features in
relation to the previous case, we plot in Fig. 4.13 the structures of the flow at several

relevant instants of time, together with the δ_{Dv} and δ_{Lv} fields. We now use the distribution of (axial or $z-$component) vorticity instead of the $Q-$value to characterize the vortex structures because, as we shall see, it is important to differentiate the clockwise from the counter-clockwise vortices, i.e. negative from positive (axial) vorticity.

The cylinder starts with no rotation at $t = 0$ in a configuration of zero lift, with a developing upper vortex, and a lower vortex almost shed from the cylinder [Fig. 4.12 (a)]. These vortices generate two opposite volume lift elements, positive on the upper front and negative on the lower front of the cylinder, as discussed above. The corresponding drag is mainly generated by these two vortices, from positive drag volume elements in their shedding tails. As the cylinder rotates, a thin region of positive vorticity develops around it generated by the interaction of the circumferential shear produced by the rotation of the surface and the incoming free stream. At $t = 7$ [Fig. 4.12 (b), (g), and (l)], when the cylinder has almost reached its maximum angular velocity (the maximum is reached at $t = 10$ for $q = 0.1$), this region of positive vorticity surrounds almost completely the cylinder. It suppress the shedding of the upper clockwise vortex, which remains then confined between the upper surface of the cylinder and this envelope of positive vorticity [Fig. 4.12 (c)–(e)]. It reinforces also the positive vorticity of the lower, slightly detached vortex. As a consequence, a thin region of positive lift volume elements (high pressure in this case) is generated on the lower half of the cylinder surface, increasing C_L. Also, the positive drag volume elements associated with the upper vortex shedding disappears, and a new thin region with negative drag volume elements behind the cylinder surface develops due to the high pressure generated by the suppression of the flow separation. The drag, however, remains almost constant because the envelope of positive vorticity also replaces the initial negative drag volume elements at the front of the cylinder surface by a thin region of positive drag volume elements (high pressure).

As time goes on, the intensity of positive vorticity surrounding the cylinder increases, suppressing also the shedding of the lower vortex. At $t = 14.25$, the drag reaches a maximum because the frontal region of positive drag volume elements reaches it maximum intensity [Fig. 4.13 (m)]. But then, an intensification of the negative drag volume elements at the rear of the cylinder is produced (the back pressure grows), so that the drag start decreasing. The lift reaches a maximum at $t = 23.75$ [Fig. 4.13 (d), (i), and (n)], when vortex shedding ceases and an envelope of positive lift volume elements surrounds almost entirely the cylinder [Fig. 4.13 (i)]. The lift remains then almost constant, with C_L close to its maximum. The drag, however, decreases further due to C_{Dv}, which even becomes negative [see Fig. 4.12 (a), and the corresponding value $\lambda_D < 1$ in Fig. 4.13 (o)]. This is because a small region of negative drag volume elements is generated on the upper front of the cylinder surface (associated with the confined upper region with negative vorticity) which is added to the existing negative drag volume elements behind the cylinder surface. Since the vortex structures become steady at $t \simeq 30$, so do the values of C_L and C_D, the first is a quite large value and the second almost vanishing. The key point of this interesting situation is the region of positive vorticity surrounding the cylinder generated by the interaction of the high rotation speed of the cylinder surface with the free stream, that suppress vortex shedding, confining the upper negative vortex in a small region on the top
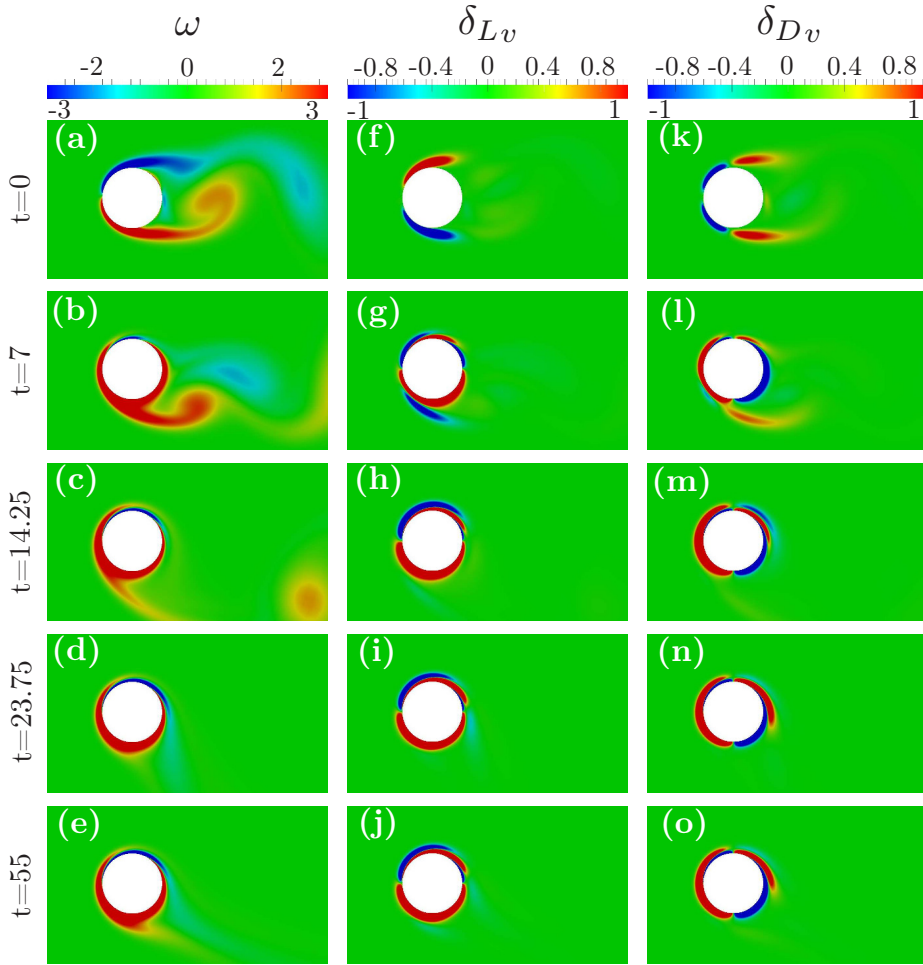
Figure 4.13: Snapshots of ω (left panels), δ_{Lv} (central panels), and δ_{Dv} (right panels) at several significative instants of time (marked in Fig. 4.12) for Re = 200 and $\gamma = 3$ with $q = 0.1$. $\lambda_L = 1.0056$ (f), 2.4741 (g), 5.5530 (h), 8.6392 (i), 7.4633 (j); $\lambda_D = 1.8453$ (k), 1.3758 (l), 1.4762 (m), 1.0868 (n), and 0.9184 (o).

of the cylinder surface, and slightly detaching the lower positive vortex over a wider region below the cylinder. This configuration generates low pressure on the cylinder upper surface, and high pressure on the lower and rear surfaces. Note, however, that C_{Ds} is comparable to C_{Dv}, so that the volume elements analysis based on δ_{Dv} only accounts for a fraction of C_D.

4.4.3 Case (ii)

We present now the results for the case (ii) for the same Reynolds number and values of γ; i.e. we now analyze the case of an initially rotating cylinder in a quiescent fluid, with a given angular velocity γ, that starts accelerating linearly in the x direction from rest until reaching a constant velocity determined by the given Re in a non-dimensional time q^{-1}.

4.4.3.1 $\gamma = 1$

Fig. 4.14 shows the temporal evolution of C_D and C_L for $\gamma = 1$ when $q = 0.1$, checking that the results from the standard surface integrals (2.13) and (2.14) are practically indistinguishable from those computed with (2.17) and (2.15). We repeat this comparison here because in this case (ii) there exists a new drag component C_{Da}, associated with the acceleration of the cylinder (it corresponds to an added-mass force), which is absent in the case (i). We select $q = 0.1$ to have a longer initial transient during which this additional drag acts on the cylinder. It is observed in Fig. 4.15 (a) that the computed C_{Da} is constant [as it must be for a constant acceleration, $\mathrm{d}U/\mathrm{d}t = 1$ in (2.17)] and equal to $\pi q = \pi/10$ for $0 \le t \le q^{-1}$. Then, C_{Da} drops to zero, once the cylinder's velocity remains constant for $t > 10$.
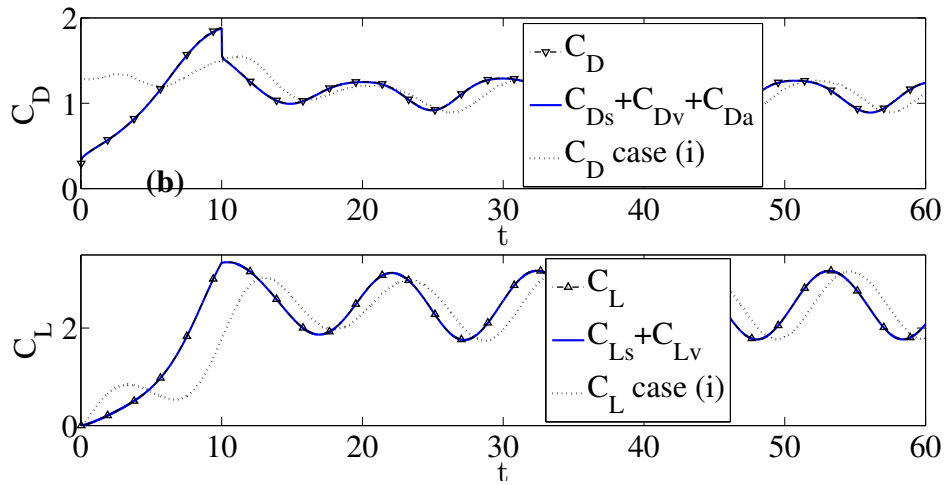
Figure 4.14: Time histories of C_D (a) and C_L (b) for Re = 200 and $\gamma = 1$ with $q = 0.1$ for the case (ii) computed from the standard surface integrals (2.13) and (2.14) (dashed-and-dotted lines with symbols), and with the formulation given by (2.17) and (2.15) (continuous lines). Also included with dotted lines are the results for the case (i) with the same values of Re, γ and q.

For reference sake, we also include in Fig. 4.14 the results obtained for the case (i) with $\gamma = 1$ and $q = 0.1$. Obviously, since Re and γ are the same, the results coincide when the fully developed flow is reached, with just a phase shift in the oscillations of C_d and C_L due to the different initial transient flows. The main differences between these flows can be discussed with the help of Fig. 4.16, where the structure of the flow (vorticity field), together with the δ_{Dv} and the δ_{Lv} fields, is shown at several relevant instants of time (marked in Fig. 4.15).

The computation begins now with the cylinder rotating with $\gamma = 1$ in a quiescent fluid. At $t = 0$, the cylinder starts moving in the direction x (to the left in Fig. 4.1) with a constant acceleration. When $t = 0.25$ [Fig. 4.16 (a)], the flow structure is still very similar to that for $t = 0$, with a positive vorticity layer surrounding the rotating cylinder that decays very fast away from the cylinder, where the fluid is almost at rest. As a consequence, the lift force is practically zero, since the positive volume lift
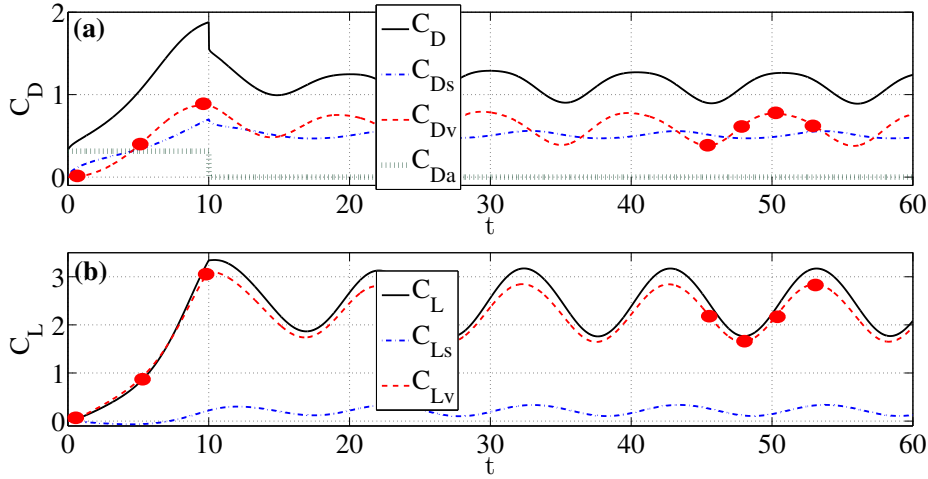
Figure 4.15: Time histories of C_D (a) and C_L (b) for Re = 200, $q = 0.1$ and $\gamma = 1$ for the case (ii) computed with (2.17) and (2.15), together with their components C_{Ds}, C_{Dv}, C_{Da}, and C_{Ls}, C_{Lv}. The filled circles correspond to the instants of time plotted in Fig. 4.16.

elements on the lower part of the cylinder generated by this vorticity distribution cancel out with the negative volume lift elements on the upper part [Fig. 4.16 (h)]. On the other hand, all the drag is practically due to the pressure force necessary to accelerate the cylinder [added-mass term C_{Da}, see Fig. 4.15 (a)], with almost negligible contribution from the volume drag elements depicted in Fig. 4.16 (o). As the cylinder's speed increases (or the free stream velocity increases in the reference frame moving with the cylinder), the vorticity field structure around the cylinder changes, generating both lift and additional drag. At half the accelerating period [$t = 5$, Fig. 4.16(b)], the original positive vorticity surrounding the cylinder is shedding, due to the stream, from the lower part of the cylinder, and a counter-rotating vortex (negative vorticity, i.e. a vortex rotating clockwise) is developing on the upper part of the cylinder. This incipient upper vortex generates positive volume lift elements [Fig. 4.16 (i)] associated with low pressure, which added to the original positive volume elements on the lower part (high pressure) yield a positive lift, that increases quite fast [see Fig. 4.15 (b)]. The maximum lift is reached at the end of the accelerating period, when the cylinder starts moving at a constant velocity. Fig. 16(c) shows the flow structure at t1/49.75, just before this maximum. The upper vortex is about to detach, generating the maximum extension of the positive volume lift elements on the upper part of the cylinder [Fig. 4.16 (j); $\lambda_L \simeq 5.44$]. The drag also reaches a maximum, with the main volume contributions coming from the rear part of this upper vortex [Fig. 4.16 (q)]. After this accelerating period, the minimum and the maximum values of C_D and C_L alternate due to vortex shedding, in a similar fashion to that described above for the case (i). In Fig. 4.16, the instants $t = 45.75$ and $t = 48$ correspond to minimum values of C_D and C_L, respectively, while $t = 50.75$ and $t = 53.25$ correspond to maximum values of C_D and C_L, respectively (see Fig. 4.15).
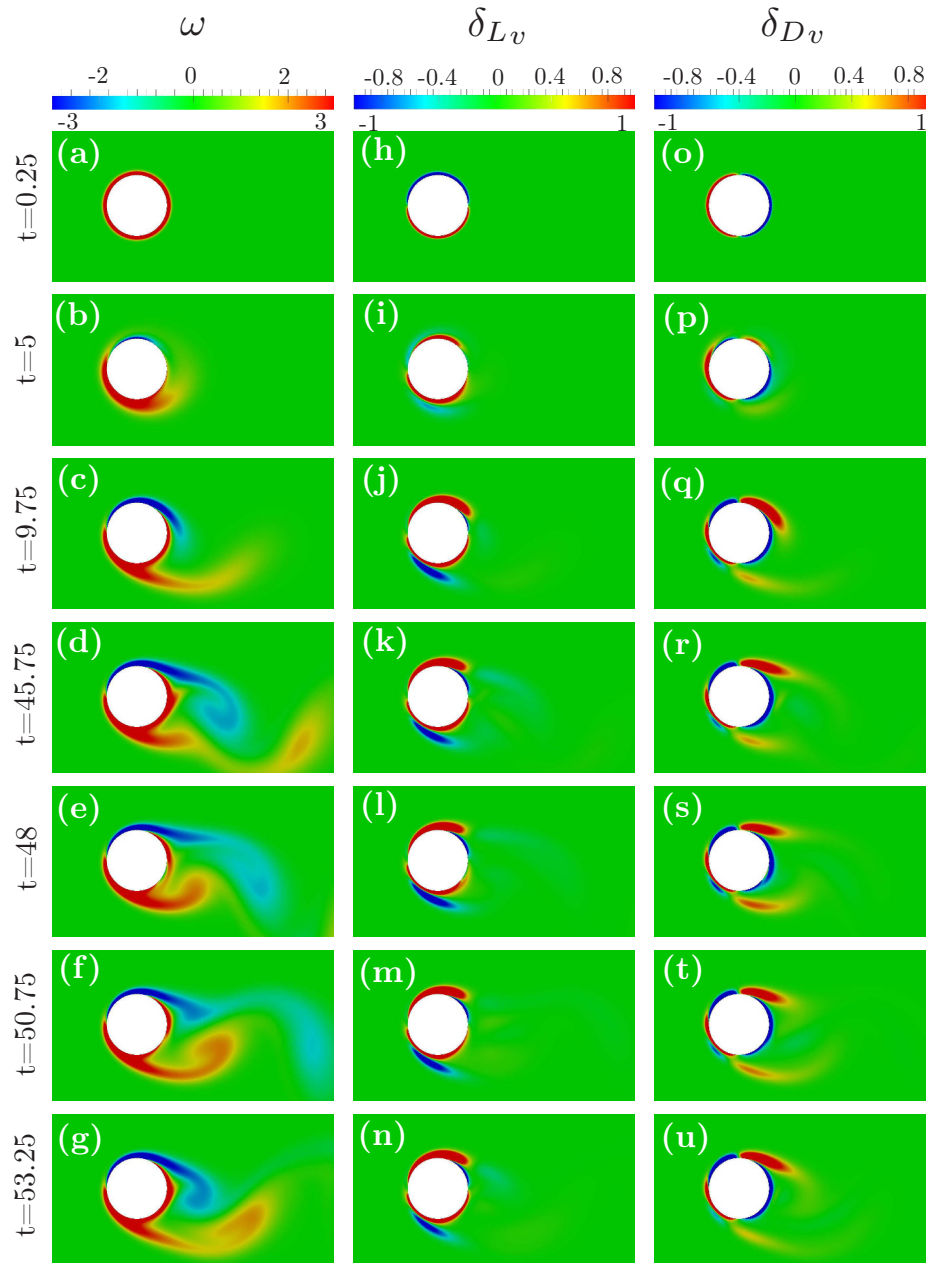
Figure 4.16: Snapshots of ω (left panels), δ_{Lv} (central panels), and δ_{Dv} (right panels) at several significative instants of time (marked in Fig. 4.15) for Re = 200 and $\gamma = 1$ with $q = 0.1$ for the case (ii). $\lambda_L = 1.0177$ (h), 3.0336 (i), 5.4357 (j), 2.6437 (k), 2.2631 (l), 3.5248 (m), 4.2020 (n); $\lambda_D = 1{:}0007$ (o), 1.6928 (p), 1.6581 (q), 1.2330 (r), 1.4286 (s), 1.5205 (t), and 1.3561 (u).

4.4.3.2 $\gamma = 3$

Fig. 4.17 shows C_D and C_L in this case (ii) for $\gamma = 3$ with $q = 0.1$. Obviously, their steady state values coincide with those reached in case (i). In fact, $C_L(t)$ is quite similar for all t [Fig. 4.17 (b)], but $C_D(t)$ differs substantially in the transient period due not only to the additional acceleration term C_{Da}, but also to the volume contribution C_{Dv}, that reaches a higher maximum owing to the acceleration. Thus, the maximum of the
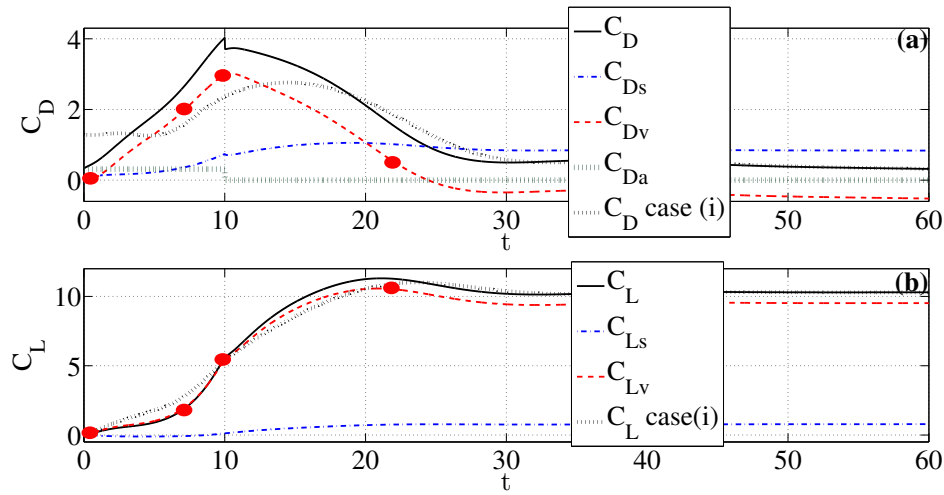
Figure 4.17: Time histories of C_D (a) and C_L (b) for Re = 200, $q = 0.1$ and $\gamma = 3$ for the case (ii) computed with (2.17) and (2.15), together with their components C_{Ds}, C_{Dv}, C_{Da}, and C_{Ls}, C_{Lv}. Also included are the results for the case (i) with the same values of Re, γ and q (Fig. 4.12). The filled circles correspond to the instants of time plotted in Fig. 4.18.
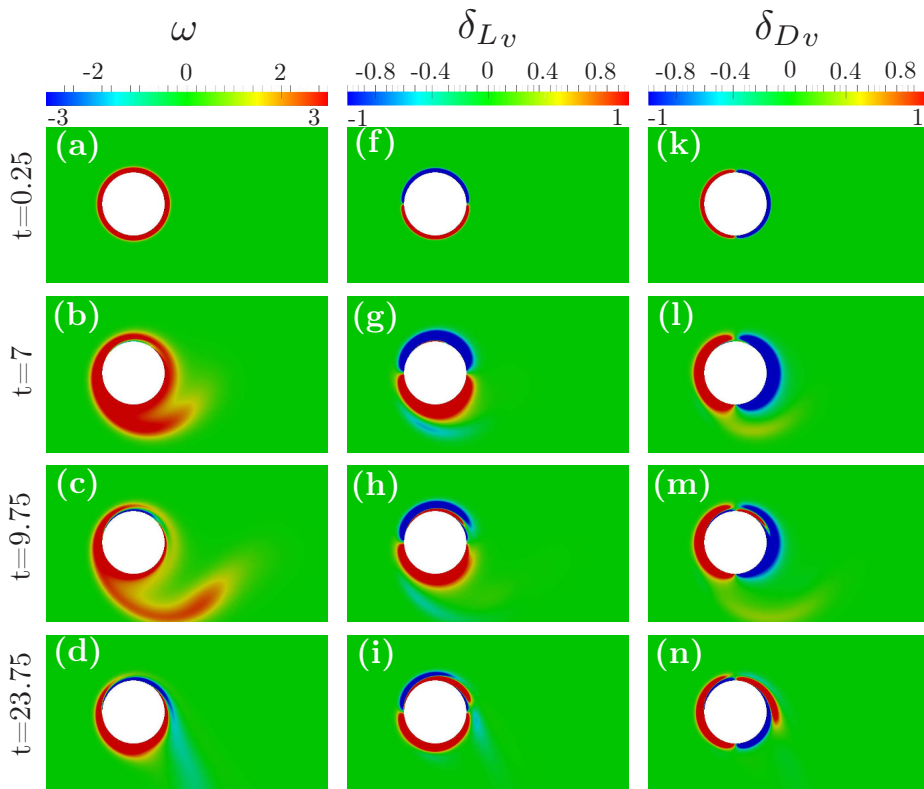
Figure 4.18: Snapshots of ω (left panels), δ_{Lv} (central panels), and of δ_{Dv} (right panels) at several significative instants of time (marked in Fig. 4.16) for Re = 200 and $\gamma = 3$ with $q = 0.1$ for the case (ii). $\lambda_L = 1.0058$ (f), 1.4604 (g), 3.0732 (h), 8.4165 (i); $\lambda_D = 1.0007$ (k), 1.4380 (l), 1.8557 (m), and 1.0200 (n).

total C_D in the transient period is significantly larger in this case (ii) than in the case (i) when $\gamma = 3$ [Fig. 4.17 (a)].

To better appreciate these differences, Fig. 4.18 shows the vorticity ω, δ_{Dv} and δ_{Lv} fields at several instants of time within the transient period (marked in Fig. 4.17). Initially [$t = 0.25$ in Fig. 4.18 (a)], the structure of the flow coincides with that for $\gamma = 1$ discussed above, but differs from the case (i) [Fig. 4.13 (a)] in the absence of vortex shedding, because the initial free stream is zero in the present case. The positive vorticity layer surrounding the rotating cylinder generates a symmetric distribution of δ_{Dv} and δ_{Lv} with no lift and no drag from the volume elements (though there is a drag C_{Da} due to the cylinder's acceleration). As time goes on, the main qualitative difference with the case (i) is that the final steady structure of the flow (without vortex shedding) is reached more straightforwardly in this case (ii) because the initial flow structure is more similar to the final one. Thus, the excess of initial vorticity is shed in just one event from the lower part of the cylinder [compare Fig. 4.18 (b) and (c) with Fig. 4.13 (b) and (c)]. In addition, as already mentioned, the drag in the transient period is larger, as can be seen in the volume drag elements of Fig. 4.18 (l) and (m) [compare with Fig. 4.13 (l) and (m), and the corresponding values of λ_D]. But, at the end, the volume drag contribution C_{Dv} is negative, so that the total drag in the final steady state is relatively small, and the same in both cases.

4.5 CONCLUDING REMARKS

We have analyzed the structure of the flow around a rotating and a translating cylinder with the aim of identifying and quantifying the structures that contribute to the lift and drag forces. We have considered two different situations with Re = 200, a cylinder translating with a constant speed that starts rotating until reaching a non-dimensional rotation rate γ (i), and an initially rotating cylinder in a quiescent fluid at a rate γ that starts translating until reaching the speed corresponding to Re = 200 (ii). In both cases we have considered $\gamma = 1$ and $\gamma = 3$. For the analysis we have used a formulation that quantifies the contribution of the different vortical structures surrounding the body on the forces (Chang, 1992). We find that, especially for the case of lift, the main contribution comes from these volume elements. The formulation can be used without modification to more complex transient laws than (i) or (ii), but the results will be qualitatively very similar provided that the rotation and the translation speeds increase monotonically. In fact, we present results for several values of the acceleration parameter q, and they do not differ significantly from each other because the underlying mechanisms generating lift and drag are essentially the same.

In general, the main contribution to the lift is generated, as expected, by the upper vortex in its root close to the upper front of the cylinder surface, where it generates a low pressure region. Without rotation of the cylinder ($\gamma = 0$), this contribution is balanced by the opposite effect of the lower counter-rotating vortex, so that the mean lift vanishes in the fully developed flow. The instantaneous lift oscillates due to vortex shedding.

When the cylinder rotates moderately ($\gamma = 1$), there is still an oscillating lift force in the fully developed flow due to the vortex shedding from the cylinder. But now the mean lift is positive (for a clockwise rotating cylinder) because the cylinder's rotation reinforces the upper clockwise vortex, while it weakens and slightly detaches from the cylinder the lower counter-clockwise vortex, so that the maximum and the minimum lift are both positive for $\gamma = 1$. For high rotation ($\gamma = 3$), the layer of positive vorticity surrounding the cylinder generated by its (clockwise) rotation ends up suppressing vortex shedding, so that the lift in the fully developed flow becomes constant. It is also large because both the attached lower vortex and the counter-rotating upper one, trapped by the surrounding vorticity, contribute positively to the lift. This interaction also reduces drastically the drag owing to the positive pressure region that it generates at the back of the rotating cylinder. The main difference found in the configuration (ii) for this case with high rotation ($\gamma = 3$) is that the fully developed flow with constant high lift and constant low drag is reached faster, because the positive vorticity layer surrounding the cylinder is already present when the cylinder starts translating, and there is no initial vortex shedding. However, in this configuration the transient drag is significantly larger due to the translating acceleration of the cylinder, which adds an additional drag term reinforcing the positive volume drag elements.

Finally, it is worth commenting that the vorticity forces formulation used in this work can of course be extended to the three-dimensional flow arising for greater values of γ than those considered in the present study. The structure and the stability of these flows have been recently considered by several investigators (see Introduction). But the study of these three-dimensional flows is out of the scope of the present work because the formulation loses the simplicity of the 2D flow around a rotating cylinder to explain the development of lift and drag, which was the main aim of the present work. In the 2D flow the auxiliary potentials are simple analytical functions, and the contributions of the different individual fluid elements to the lift and drag are much more straightforwardly analyzed.

5

VORTEX FLOW STRUCTURES AND INTERACTIONS FOR THE OPTIMUM THRUST EFFICIENCY OF A HEAVING AIRFOIL AT DIFFERENT MEAN ANGLES OF ATTACK

5.1 INTRODUCTION

The unsteady aerodynamics of oscillating airfoils at the low Reynolds number range of in terest for small flying animals (mostly insects) has been widely studied theoretically, numerically, and experimentally (Shyy et al., 2013). The main motivation of many of these studies has been the understanding of the flow mechanisms by which the lift is greatly enhanced in relation to the predictions of the quasi-steady aerodynamic theory and the mechanisms by which thrust or propulsion is generated. Traditionally, these studies were aimed to the understanding of the biomechanics of insect (and small birds and mammals) flight (see Maxworthy, 1981, Dudley, 2000, Sane, 2003, Wang, 2005). But the interest in the unsteady aerodynamics of flapping flight has significantly grown in recent years in relation to the design of Micro-Aerial Vehicles (MAVs) that take advantage of the accumulated knowledge on animal flight (see Ellington, 1999, Mueller, 2001, Pines and Bohorquez, 2006, Ansari et al., 2009 and Jones and Platzer, 2009).

Here, we focus on the thrust generation by an oscillating airfoil at low Reynolds numbers, particularly on the characterization of the vortical flow structures responsible for the maximum thrust efficiency at selected non-dimensional frequencies and amplitudes of the oscillations. We consider the two-dimensional (2D) and incompressible viscous flow around a plunging airfoil at different mean angles of attack. This simplified problem, with only heaving motion, has been widely considered as an appropriate simple model to understand the flow mechanisms which are responsible for thrust generation in flapping flight and swimming. It has been known for a long time that net thrust is characterized by a reversed von Kármán vortex street behind the heaving airfoil (Kármán and Burgers, 1935 and Bratt, 1950), with vortices rotating in the opposite direction of the well known drag-producing von Kármán vortex street. Different kinds of spatial patterns of vortices have been identified in several forms of propulsion by aquatic animals (see e.g., Wu, 1961, Lighthill, 1969 and Lighthill, 1970). In addition, in many of the proposed thrust mechanisms, the leading-edge vortex (LEV) generated during the wing-beat plays an important role. It is well known that the high lift coefficients characterizing most insect flight is due to the low-pressure regions inside the LEV generated temporarily after a sudden change in the effective local angle of attack during flapping (some related information is available in Lighthill, 1975, Maxworthy, 1979, Dickinson and Götz, 1993, Ellington et al., 1996, Liu et al., 1998, Sane and Dickinson, 2001, Minotti, 2002, Maxworthy, 2007, Shyy and Liu, 2007 and Pitt and Babinsky, 2013). To optimize this effect, most insects fly at the limit of dynamic stall to generate a prominent LEV. The relevance of the LEV for high efficiency thrust and propulsion by a pure heaving motion was first acknowledged and studied in relation to simple models for fish swimming as Streitlien et al. (1996), Anderson et al. (1998) and

Triantafyllou et al. (2000) reported. It was already known that the efficiency of thrust generation by a flapping airfoil is mainly governed by a Strouhal number based on the amplitude and frequency of the oscillations (St_a defined in Sec. 5.2) (see Triantafyllou et al., 1993, Jones et al., 1996 and Lai and Platzer, 1999). For very low St_a, below a threshold of about 0.03, only drag is produced by the oscillating airfoil as stated by Lai and Platzer (1999). For large frequencies for a given amplitude, when $St_a \sim 0.06$, net thrust is generated by the inversion of the vortices in the von Kármán vortex wake behind the heaving airfoil (this conclusion is reached in Jones et al., 1996, Lai and Platzer, 1999 and Koochesfahani, 1989). Experimental and numerical results show that in a wide range of Reynolds numbers (Re, also defined in Sec. 5.2), the optimal efficiency for thrust generation is reached in an intermediate range of St_a, between 0.12 and 0.20, approximately, which is thus selected by many swimming and flying animals (Triantafyllou et al., 1993, Triantafyllou et al., 1991, Lentink and Gerritsma, 2003 and Taylor et al., 2003). By the way, these experimental results contrast the potential theory results for small-amplitude oscillations, predicting that propulsion efficiency is maximized as the frequency goes to zero (see Theodorsen, 1935 and Garrick, 1936), whence the relevance of viscous effects in modelling the thrust generated by a heaving airfoil at the relevant Reynolds numbers of interest. This flapping frequency selected for optimum thrust efficiency has been identified with the frequency of maximum spatial amplification of the wake, based on linear stability analyses of the wake mean velocity profile (Triantafyllou et al., 1993 and Lewin and Haj-Hariri, 2003), and with the natural shedding frequency of the airfoil (Lentink and Gerritsma, 2003). Also, this frequency range observed in biological propulsion has been correlated to the range of limiting dimensionless time for optimal vortex formation by the flapping appendage (Dabiri, 2009).

It has been shown that the thrust efficiency of a flapping airfoil depends on the interactions between LEV and trailing-edge vortex (TEV) (Streitlien et al., 1996 and (Anderson et al., 1998)), the efficiency being larger when they interact constructively leading to two vortices deposited per stroke. This situation occurs in the range of St_a mentioned above. Wang (2000) demonstrated, using 2D numerical simulations for a heaving elliptic airfoil and relating the resulting forces to those generated by the LEV in a single stroke, that this preferred range of St_a is connected with maximizing the effective local angle of attack allowed for the low range of Reynolds number considered. But, in addition to St_a, which is a combination of the frequency and amplitude of the oscillations, there exists another degree of freedom, characterized by the reduced frequency (k) or the related Strouhal number based on the flapping frequency only (St_c defined in Sec. 5.2 along with k), which has to be taken into account. Wang (2000) related the range of St_c for optimum thrust efficiency to the equilibrium between the time scales for LEV growth and shedding. The obtained value around 0.7 is consistent with data for many birds' and insects' flight in a wide range of Reynolds numbers (see Dudley, 2000 and Azuma, 2006). In a more detailed numerical study on the vortex structure of the 2D flow around a heaving airfoil at low Reynolds number, Lewin and Haj-Hariri (2003) showed that the timing of the separation of the LEV is crucial to the heaving efficiency, with the optimum thrust occurring when the LEV remains attached for the duration of each stroke. These authors concluded, in agreement with a Anderson et al. (1998), that high propulsion efficiencies correspond to the positive

reinforcement of the TEV by the LEV. They also found aperiodic and asymmetric (deflected wake) solutions in some ranges of the parameters St_a and St_c (related to kh and k, respectively, in their notation, see Sec. 5.2). The wake patterns depended on whether or not the LEV is shed and on how the LEV interacts with the TEV (reinforcing or attenuating it). The numerical simulations by Lewin and Haj-Hariri (2003) produced aperiodic results when both St_a and St_c were sufficiently high. The mechanisms of the wake deflection in a 2D heaving airfoil, caused by the LEV-TEV interaction, and their connection to the aperiodic flows generated at high St a even in a symmetrical and periodic heaving motion, have been more recently studied by Blondeaux et al. (2005), Lua et al. (2007), Zheng and Wei (2012) and Wei and Zheng (2014). For instance, the detailed experimental results by Lua et al. (2007) for a heaving elliptic airfoil shed further light on the relation between the different LEV-TEV interactions, as St_a and St_c are varied, with the different structures of the wake. But neither of these experimental and numerical studies analyzed quantitatively the effect that the successively generated LEVs and TEVs, and their interactions, have on the thrust of the heaving airfoil. We think that this quantitative analysis is very relevant to understand the vortex configuration for optimum thrust efficiency.

Thus, to explain better all the above phenomena affecting the thrust efficiency of a heaving airfoil, we study in this work the connection between the LEV and the TEV dynamics with the thrust efficiency quantitatively by using a vortex force decomposition, originally developed by Chang (1992), in a 2D numerical simulation of the flow. This formulation provides the quantitative contribution of each vortex flow structure, such as the LEV and the TEV, to the lift and drag or thrust at any instant of time (see also Lee et al., 2012 and Martín-Alcántara et al., 2015). In order to be able to obtain analytically the auxiliary potentials that separate the vortex force into lift and drag (or thrust), we use an elliptic airfoil, as in many previous numerical works. In addition, in the present work, we also consider the effect of mean angles of attack α different from zero in the thrust efficiency of the heaving airfoil, which has not been taken into account in previous works. The vertical asymmetry introduced by $\alpha \neq 0$ changes dramatically the structure of the flow and thrust efficiency, even for small $|\alpha|$. In short, we consider quantitatively the effect of the LEV-TEV interaction, the LEV splitting, stretching, convection and diffusion, and other vortex dynamics mechanisms in the thrust efficiency of a heaving airfoil for different values of St_a, St_c, and α for a given (relatively small) value of the Reynolds number of interest in insects' and MAVs' flight.

The present chapter is organized as follows: in Section 5.2, the problem is formulated, with the analytical auxiliary potentials given in Appendix A. In that appendix, we also obtain analytically, with the help of the auxiliary potentials, the added-mass contributions to the lift and drag (or thrust) for any heaving motion of an elliptic airfoil at any mean angle of attack. These solutions also help to the validation of the numerical method, which is described in Section 5.3, and validated further in Appendix B with results from previous works. The numerical results are presented and discussed in Section 5.4, and the main conclusions are summarized in Section 5.5.

5.2   FORMULATION OF THE PROBLEM

We consider here the two-dimensional unsteady and incompressible flow of a uniform current over an oscillating ellipse. In particular, the ellipse, which represents a wing element with chord length c and thickness e, forms an angle α with the current of constant speed U (see Fig. 5.1) and performs a sinusoidal heaving motion perpendicular to the current with amplitude h_0 and frequency f,

$$h(t) = h_0 \sin(2\pi f t). \tag{5.1}$$

Using the chord c and the free stream speed U as the reference length and velocity, respectively, the non-dimensional Navier–Stokes equations and boundary conditions governing the incompressible flow can be written as

$$\nabla \cdot \mathbf{v} = 0, \tag{5.2}$$

$$\frac{\partial}{\partial t}\mathbf{v} + \mathbf{v} \cdot \nabla \mathbf{v} = -\nabla p + \frac{2}{\mathrm{Re}}\nabla^2 \mathbf{v}, \tag{5.3}$$
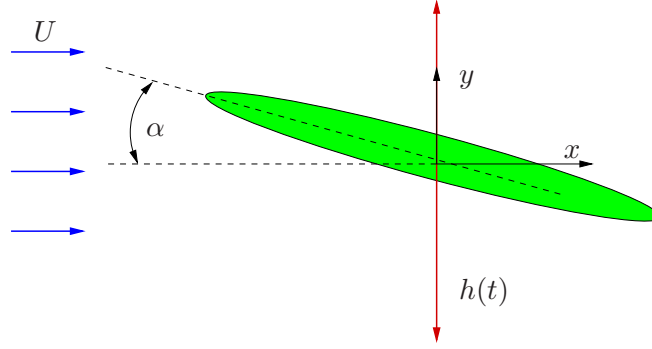
Figure 5.1: Schematic of the problem

$$|\mathbf{x}| \to \infty, \quad \mathbf{v} \to \mathbf{e}_x, \quad p \to 0, \tag{5.4}$$

$$S(\mathbf{x}, t) = 0, \quad \mathbf{v} = V_0(t)\,\mathbf{e}_y \equiv 2\pi St_a \cos(2\pi St_c t)\mathbf{e}_y, \tag{5.5}$$

where $\mathbf{v}$ is the non-dimensional velocity, p the non-dimensional relative pressure (scaled with ρU^2, being ρ the fluid density), $\mathbf{e}_x$ and $\mathbf{e}_y$ are the unit vectors in the direction of the free stream velocity and in its perpendicular direction, respectively, and $S(\mathbf{x}, t)$ defines the non-dimensional position of the ellipse surface as a function of time in a fixed reference frame (see Sec. 5.3). In the above equations, we have defined the following non-dimensional parameters:

$$\mathrm{Re} = \frac{\rho U c}{\mu}, \quad St_a = \frac{h_0 f}{U}, \quad St_c = \frac{cf}{U}, \tag{5.6}$$

i.e., a Reynolds number based on the chord length c and two Strouhal numbers, one based on the amplitude of the oscillation h_0 and the other one on the chord length, being μ the fluid viscosity. These two Strouhal numbers are related to the advance

ratio J and the reduced frequency k, respectively, usually defined in the flapping wing literature (see Shyy et al., 2013 and Dudley, 2000),

$$J = \frac{U}{2\pi f h_0} = \frac{1}{2\pi St_a}, \quad k = \frac{2\pi f c}{U} = 2\pi St_c. \tag{5.7}$$

St_a is also related to the parameter kh used in Lewin and Haj-Hariri (2003) by $k = 2\pi St_a$.

The non-dimensional force (scaled with $\frac{1}{2}\rho U^2 c$) that the fluid exerts on the ellipse surface $S(\mathbf{x}, t) = 0$ can be written as the sum of the pressure and viscous friction forces,

$$\mathbf{F} = -2\int_S p\mathbf{n}\,\mathrm{d}s + \frac{2}{\mathrm{Re}}\int_S (\boldsymbol{\omega} \wedge \mathbf{n})\,\mathrm{d}s, \tag{5.8}$$

where $\mathbf{n}$ is the outward unit vector normal to the ellipse and $\boldsymbol{\omega} = \nabla \wedge \mathbf{v}$ is the nondimensional vorticity field. The $x-$ and $y-$components of $\mathbf{F}$ are the drag and lift coefficients, respectively,

$$C_D = \mathbf{F} \cdot \mathbf{e}_x, \quad C_L = \mathbf{F} \cdot \mathbf{e}_y. \tag{5.9}$$

If $C_D \leq 0$, it becomes a thrust coefficient. Since we are using U as the reference velocity, the output or thrust power coefficient numerically coincides with $-C_D$, while the input power coefficient, or power needed to heave the airfoil, is the product of $-C_L$ and heaving nondimensional velocity V_0 (5.5),

$$C_{Po} = -C_D, \quad C_{Pi} = -C_L V_0. \tag{5.10}$$

We shall compute these quantities both instantaneously and integrated over time to obtain the work done in propelling the airfoil, W_o, and the work needed to heave it, W_o. These integrals are made over a cycle or stroke of the airfoil, of duration St_c^{-1}. The ratio is the thrust efficiency,

$$\eta = \frac{W_o}{W_i}. \tag{5.11}$$

In the fully developed flow, these quantities may vary from cycle to cycle if the fluid motion does not become periodic with the same frequency as the heaving motion, and we shall define also average values over a number of strokes (see Sec. 5.4.1).

Alternatively, we shall obtain the drag and the lift coefficients using a formulation developed by Chang, 1992 that allows for a quantitative identification of the contributions of the different vortex flow structures to these forces (see Lee et al., 2012 and Martín-Alcántara et al., 2015). For a deeper understanding of this formulation the reader is referred to Chapter 2.

5.3   NUMERICAL METHOD

We solve numerically (5.2)–(5.5) in a spatial grid around the ellipse which is obtained by a Joukowski transformation (Milne-Thomson, 1996) that maps a circle of radius a centred at the origin into an ellipse with main axis of length unity forming and angle $-\alpha$ with the horizontal axis x (see Fig. 5.1) and minor axis length $\epsilon = e/c$. This transformation between the $\tau = \xi + i\eta$ complex plane of the circle and the $z = x + iy$ complex plane of the ellipse can be written as

$$z = \left(\tau + \frac{1-\epsilon^2}{16\tau}\right)e^{-i\alpha}, \tag{5.12}$$

with the radius of the circle given by $a = (1 + \epsilon)/4$. The fixed ellipse with chord length 1 is obtained by the transformation of the circle $\tau = ae^{i\theta}$, for $0 \le \theta \le 2\pi$, and is given by $z = (\cos\theta + i\epsilon\sin\theta)e^{-i\alpha}$, or in cartesian coordinates,

$$x = x_0(\theta) \equiv \frac{1}{2}\cos\alpha\cos\theta + \frac{\epsilon}{2}\sin\alpha\sin\theta, \tag{5.13}$$

$$y = y_0(\theta) \equiv -\frac{1}{2}\sin\alpha\cos\theta + \frac{\epsilon}{2}\cos\alpha\sin\theta, \tag{5.14}$$

with $0 \le \theta \le 2\pi$.

Thus, the flapping ellipse, denoted by $S(x,t) = 0$ in (5.5), is given, in terms of the parameter θ, by

$$x = x_0(\theta), \quad y = y_0(\theta) + H(t),$$
$$H(t) = \frac{h_0}{c}\sin(2\pi St_c t), \quad \frac{h_0}{c} = \frac{St_a}{St_c}. \tag{5.15}$$

The outer boundary of the computational domain, where boundary conditions (5.4) are numerically imposed, is chosen as the transformation of the circle $\tau = R_o e^{i\theta}$, with $R_o \gg 1$, which is also "almost" a circle in the plane z.
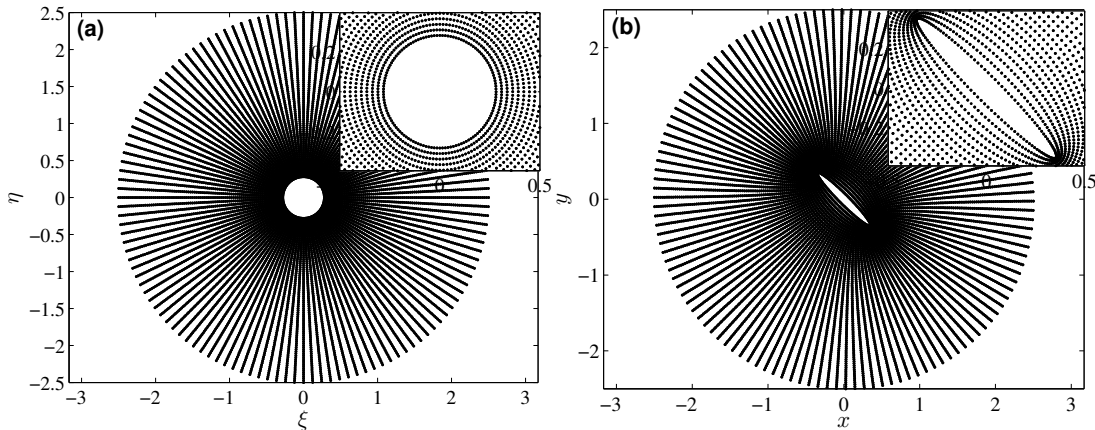
Figure 5.2: Mesh example in the τ plane (a) and its transformation into the z plane (b). Details of the grids near the inner circle and the ellipse are given in the insets. $R = 2.5$, $\varepsilon = 1/8$, and $\alpha = 45°$.

As an illustration, Fig. 5.2 shows an example of a very coarse mesh in the plane τ and its transformation into the plane z for $R_o = 2.5$, $\epsilon = 1/8$ ($a = 9/32$), and $\alpha = 45°$, with 128 nodal points on the circle (and ellipse) and a total of 10 240 grid elements. In the reported computations, we used finer meshes with much more elements and larger values of R_o (see convergence analysis in Appendix B).

Since the ellipse is moving with velocity $V_0 \mathbf{e}_y$ given by (5.5), we used a moving and deforming mesh whose motion is prescribed by solving the Laplace equation $\nabla \cdot (k\nabla \mathbf{x}) = 0$, where $\mathbf{x}$ is the displacement field and k is a diffusion coefficient which is chosen to decrease quadratically with the distance l from the moving boundary, $k(l) = 1/l^2$ (see, e.g., Bos et al., 2013 for details).

To solve numerically (5.2)–(5.5) along with (2.3)–(2.4) and (2.7)–(2.8) in the above described dynamic mesh, we used the software OpenFOAM®, an open source Computational Fluid Dynamics (CFD) package based on the Finite Volume Method. For the spatial discretization, we used second order accuracy linear interpolation for the diffusion term, and a Total Variation Diminishing (TVD) scheme, with a van Leer limiter, for the convection term. This hybrid scheme is set in order to avoid numerical oscillations in grid regions where local mesh Reynolds number is high (far field) and convection dominates over diffusion. On the other hand, the temporal discretization was performed by blending a second order Crank-Nicolson scheme with implicit Euler integration, to ensure boundedness of the solution. Moreover, the pressure-velocity coupling has been treated through the pressure-implicit split-operator (PISO) algorithm (Issa, 1985), using a small temporal step to keep the maximum Courant number under 0.5. Finally, the integrals to compute the different forces' coefficients were discretized with second-order accuracy by using the midpoint rule in combination with linear interpolation schemes.

We set an impulsively started flow past an ellipse located at the center of the domain as initial conditions. Validation with results from previous works and convergence analyses are given in Appendix B. In addition, a validation of the numerical results against analytical results for C_{La} and C_{Da} is given in Appendix A.

5.4   RESULTS AND DISCUSSION

5.4.1   *Flow characteristics for a fixed St_a and $\alpha = 0$*

We consider first the case $St_a = 0.16$ (i.e., $J \simeq 1$) with detail to discuss the different flow structures as the heaving frequency (St_c) is varied and their effect in the thrust power and efficiency. All the results are for Re = 500 and $\alpha = 0$.

Figures 5.3 and 5.4 show the evolution in time of the different components of C_D and C_L as well as the output (thrust) and input works and efficiencies as functions of the successive strokes ($n = tSt_c$) for two frequencies: $St_c = 0.5$ and $St_c = 0.9$. Note that $C_{Da} = 0$ for $\alpha = 0$ (see Appendix A) that is corroborated numerically with the computed auxiliary potential $\overline{\phi}$. The "volumentric" efficiency defined as $\eta_v = W_{ov}/W_i$ [compare with (5.11)], where $W_o = W_{ov} + W_{os}$, with W_{ov} and W_{os} computed integrating

$-C_{Dv}$ and $-C_{Ds}$, respectively, over a period of one stroke $T = St_c^{-1}$. We can also define a "surface" efficiency $\eta_s = W_{os}/W_i$, but it is not necessary because $\eta_v + \eta_s = \eta$.
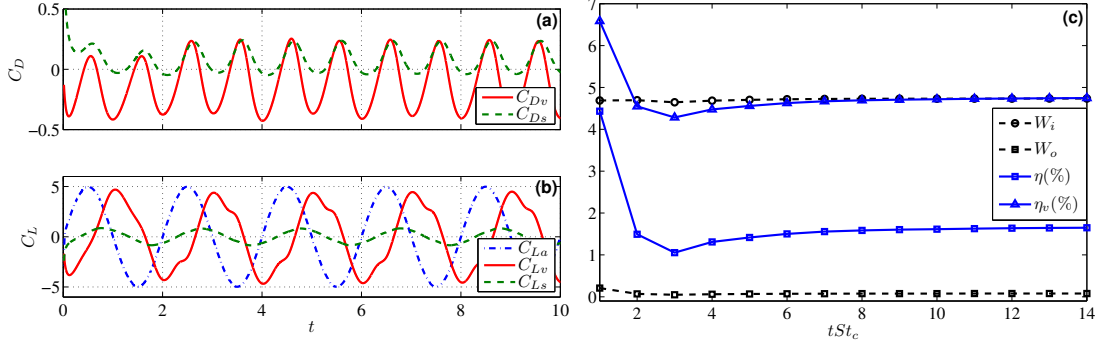
Figure 5.3: Different components of C_D (a) and C_L (b) vs. t for $Re = 500$, $\alpha = 0$, $St_a = 0.16$, and $St_c = 0.5$. (c) Input and output works, W_i and W_o, and efficiencies η and η_v vs. the increasing number of strokes tSt_c for the same case.
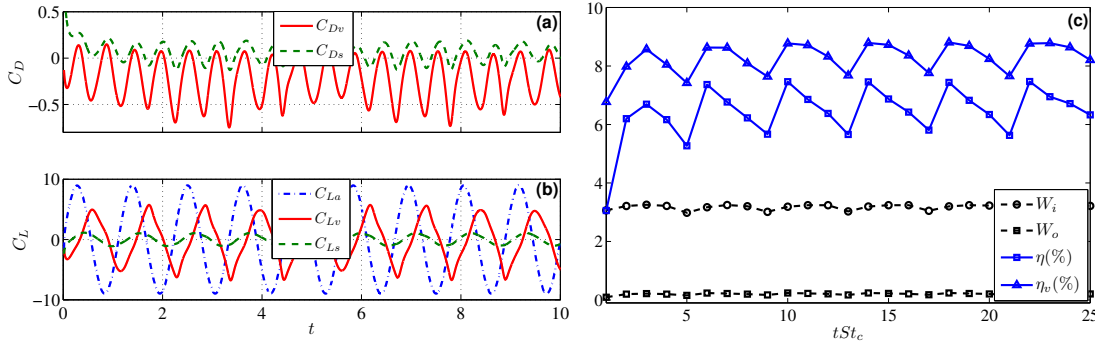
Figure 5.4: As in Fig. 5.3, but for $St_c = 0.9$.

For the first frequency (Fig. 5.3), the flow becomes periodic, and therefore, the different works and efficiencies, which are integrated over a stroke, tend to constant values. However, Fig. 5.3(a) shows that for the higher frequency $St_c = 0.9$, the flow never reaches a periodic state with the heaving frequency, so that the works and efficiencies never tend to constant values. In this particular case, the flow is not completely *aperiodic*: Fig. 5.4(c) shows that the flow reaches a quasi-periodic state, with a period of four full strokes of the airfoil.

To analyze the main differences in the flow structure, we note first that C_{La} appearing in (2.24) is always in phase and proportional to the airfoil heaving motion [in fact, it is proportional to the vertical acceleration, as obtained analytically in (2.40)],

$$C_{La} = 2\pi^3 St_c St_a \sin(2\pi St_c t) = 2\pi^3 St_c^2 H(t). \tag{5.16}$$

This expression corresponds to the added mass contribution to the lift, and it is corroborated by using the auxiliary potential ϕ obtained numerically from (2.3) and (2.4) (see Chapter 2; in fact, all the reported results are obtained numerically, not using 5.16 nor any of the other analytical expressions given in Chapter 2). Thus, this term helps to compare the temporal oscillations of the other components of C_L and C_D with the airfoil oscillations in Figs. 5.3 and 5.4 and subsequent similar figures. Note that

5.22 is valid for any horizontal ellipse moving harmonically in the vertical direction, independently of its thickness ϵ.

The oscillations of the two components of C_D [Figs. 5.3(a) and 5.4(a)] have a frequency twice that of the heaving motion due to the vortex formation and shedding during each half stroke (see below), while the oscillations of the other two components of C_L have the same frequency as the heaving motion, but both with a substantial phase shift. However, in the case of $St_c = 0.9$, these oscillations are not periodic like in the case of $St_c = 0.5$, as already commented. It is also observed in Figs. 5.3(a) and 5.4(a) that C_{Ds} is mostly positive, contributing to the drag, while C_{Dv} is mostly negative, contributing to the thrust of the airfoil. But the overall effect is a net thrust because the mean contribution of C_{Dv} is larger than that of C_{Ds} in both cases. This is clearly seen in the positive values of W_o and η in both cases [Figs. 5.3(c) and 5.4(c)] and in the fact that the volumetric efficiency η_v is also larger than the total efficiency η in both cases (this means that η_s is obviously negative).

We observe in Fig. 5.5) ($St_c = 0.5$) that thrust is generated (δ_{Dv} is negative; see Subsec. 2.2.2 for its definition) during the formation of the LEV, especially in the first part of each downstroke [Figs. 5.5(a)–5.5(d)] and each upstroke [Figs. 5.5(e)–5.5(h)], and by the shedding TEV of the previous half stroke. Drag is generated (positive δ_{Dv}) during the formation of the TEV, especially in the first part of each downstroke and each upstroke, and by the shedding LEV of the previous half stroke when captured and stretched by the current half stroke.

The main difference of the case $St_c = 0.9$ (Fig. 5.6) is that most of the LEV generated in each half stroke is not shed for this higher frequency. A significant fraction of the LEV remains at the leading edge (LE), stretching and diffusing during the subsequent half strokes, thus generating significantly less drag. Since the other thrust and drag generating episodes remain practically the same, the total thrust work and efficiency are larger for this higher frequency than for $St_c = 0.5$ [compare Figs. 5.3(c) and 5.4(c)]. A fraction of each LEV vorticity that is not diffused is eventually shed, joining the TEV of the corresponding half stroke. This happens every four strokes in this case (see multimedia view corresponding to Fig. 5.6), explaining the periodicity of four strokes in Fig. 5.4(c).

Note that in both cases, a thrust-producing reverse-Kármán-vortex-street wake is generated, as it was characterized experimentally by Jones et al. (1996) and by Lai and Platzer (1999). To the generation of these vortices in the wake contributes both the LEVs and the TEVs, as previously found numerically by Lewin and Haj-Hariri (2003) and observed experimentally by Lua et al. (2007) also for a heaving, two-dimensional elliptic airfoil.

Fig. 5.7 shows the mean values of the input and output works and efficiencies, $\overline{W}_o$, $\overline{W}_i$, $\overline{\eta}$, and $\overline{\eta}_v$, as functions of the frequency St_c for the present case $St_a = 0.16$. For the frequencies where the flow becomes periodic with the heaving frequency, these mean values correspond to the asymptotic constant values of W_o, W_i, η, and η_v, respectively [e.g., Fig. 5.3(c)]. For the remaining frequencies, we average these quantities over a
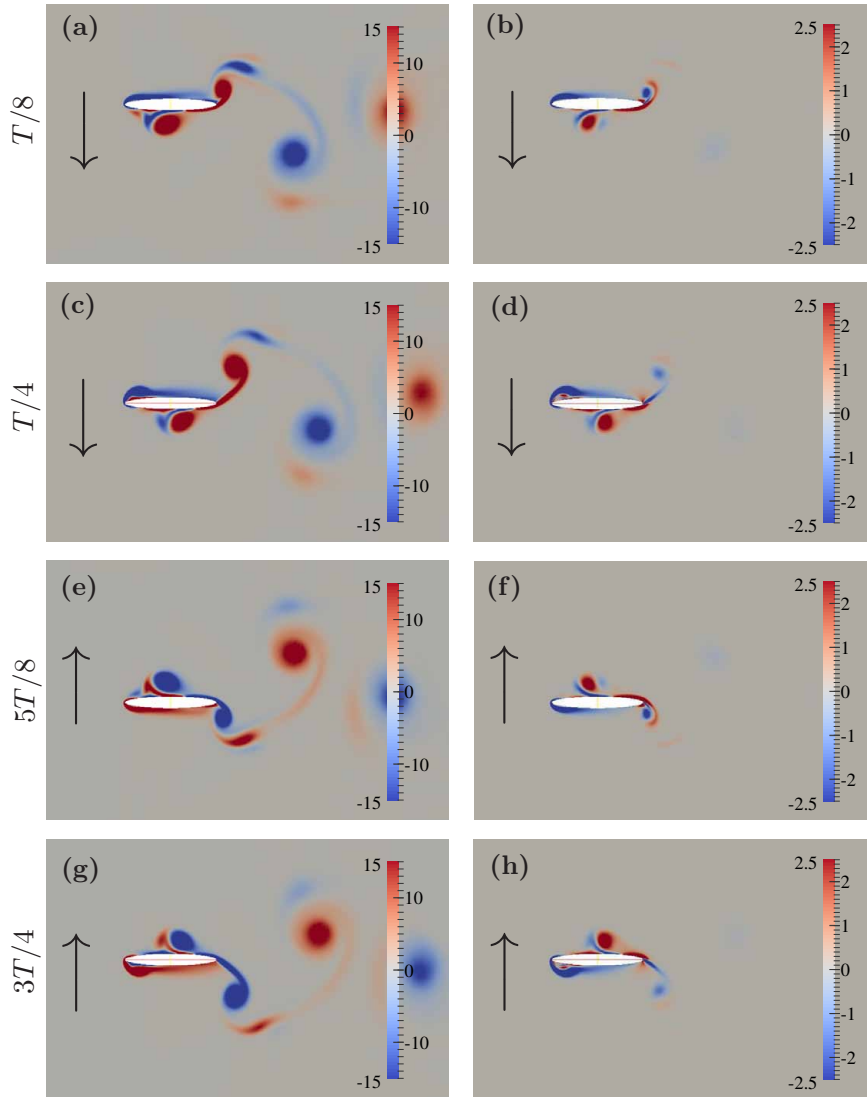
Figure 5.5: Snapshots of ω (left panels) and of δ_{Dv} (right panels) at several significative instants of time within the same stroke ($T = St_c^{-1}$ denotes the non-dimensional period of one stroke, starting from the beginning of the downstroke) for $St_a = 0.16$, $St_c = 0.5$, $Re = 500$, and $\alpha = 0$. (Multimedia view) [URL: http://dx.doi.org/10.1063/1.4926622.1]

sufficiently large number of strokes to get a mean value with an error less that 2.5 % (see Sec.5.4.2). The oscillations in these quantities are characterized by their standard deviations with error bars in Fig. 5.7. It is observed that in the present case $St_a = 0.16$, the flow does not become periodic with the frequency of the heaving motion only for $St_c = 0.9$ and 1.1. For these two frequencies, the flow is not aperiodic (chaotic), as it happens for larger St_a (see below), but acquires a periodicity of several strokes (4 and 3, respectively). Therefore, averaging over these numbers of cycles is enough to obtain accurately the mean values given in Fig. 5.7. More complex aperiodic motions will be described in Secs. 5.4.2 and 5.4.3.
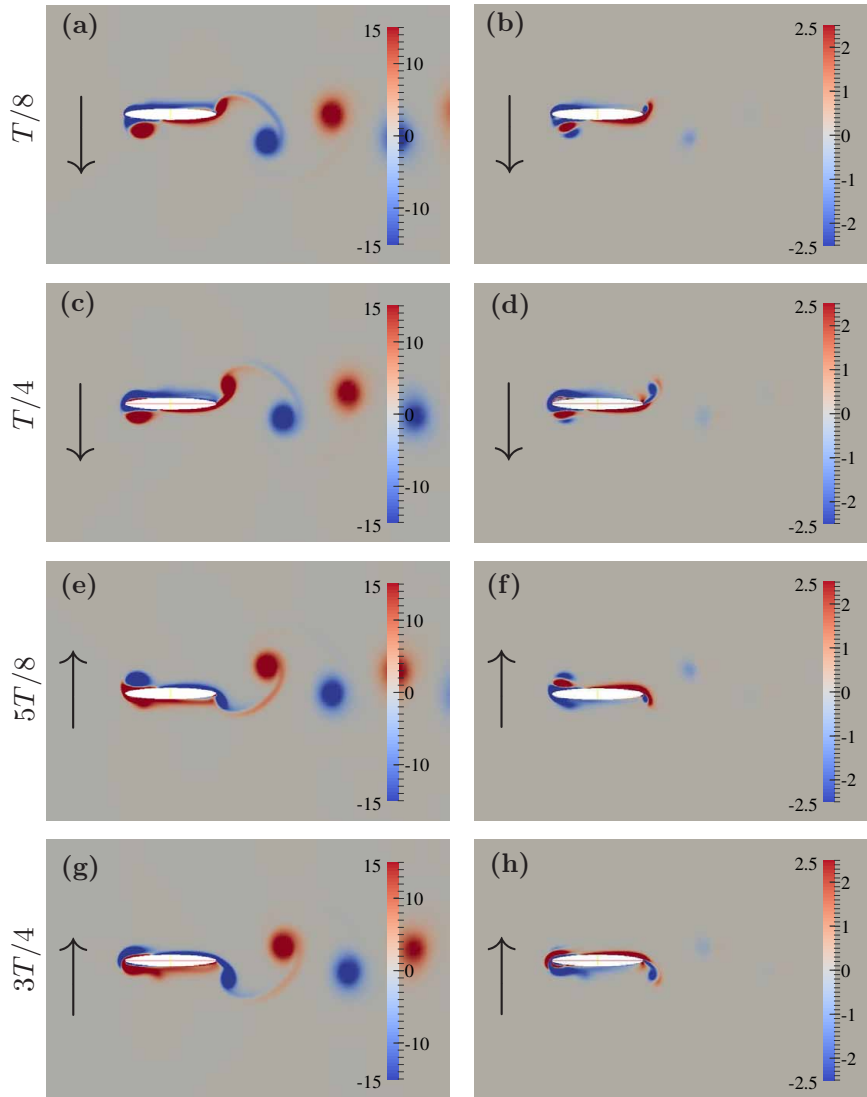
Figure 5.6: Snapshots of ω (left panels) and of δ_{Dv} (right panels) at several significative instants of time within the same stroke for $St_a = 0.16$, $St_c = 0.9$, $Re = 500$, and $\alpha = 0$. (Multimedia view) [URL: http://dx.doi.org/10.1063/1.4926622.2]
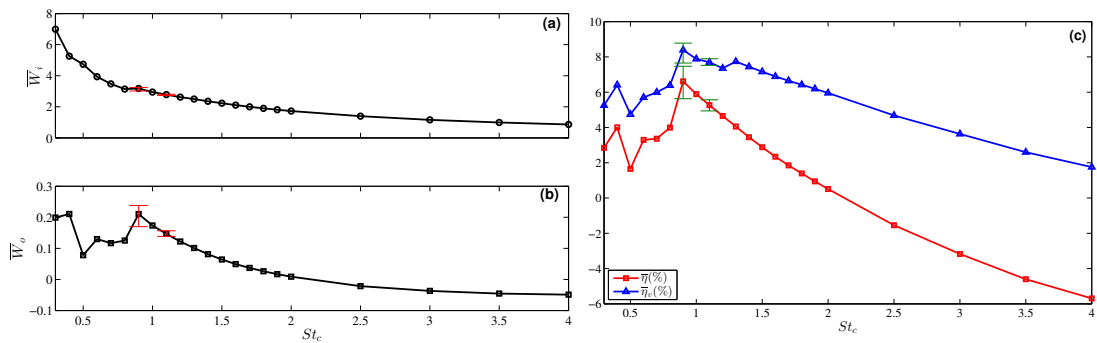
Figure 5.7: Mean values of W_i (a), W_o (b), η and η_v (c) as functions of St_c for $St_a = 0.16$, $Re = 500$, and $\alpha = 0$.

According to Fig. 5.7, the two frequencies analyzed above correspond to the maximum efficiency ($St_c = 0.9$) and to a local minimum ($St_c = 0.5$). As St_c augments from 0.9, an increasing portion of the LEV generated in a previous half stroke moves around the LE to the other part of the airfoil [see Fig. 5.8 for $St_c = 1.2$ and compare with Figs. 5.6(g) and 5.6(h)], generating more drag, and thus reducing the total thrust and mean efficiency in relation to $St_c = 0.9$. Although the mean "volumetric" efficiency $\bar{\eta}_v$ never becomes negative as St_c increases [see Fig. 5.7(c)], i.e., the regions with negative δ_{Dv} always weight more than the regions with positive δ_{Dv}, the global efficiency becomes negative for $St_c \gtrsim 2$ due to the surface contribution C_{Ds}, which always contributes with a positive mean value (i.e., to the drag).
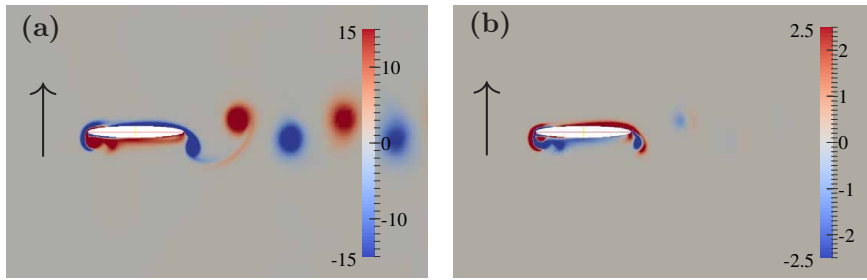
Figure 5.8: Snapshots of ω (left panels) and of δ_{Dv} (right panels) at the instant $3T/4$ within a stroke for $St_a = 0.16$, $St_c = 1.2$, $Re = 500$, and $\alpha = 0$. (Multimedia view) [URL: http://dx.doi.org/10.1063/1.4926622.3]
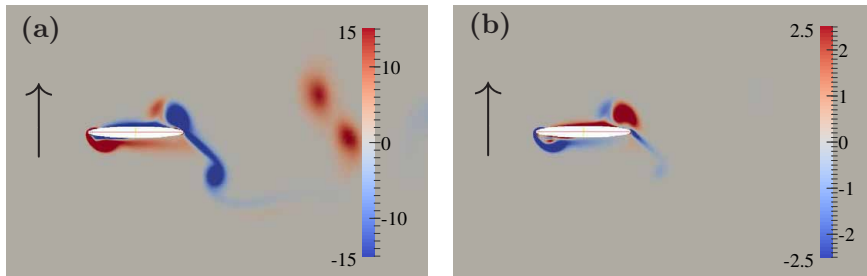
Figure 5.9: Snapshots of ω (left panels) and of δ_{Dv} (right panels) at the instant $3T/4$ within a stroke for $St_a = 0.16$, $St_c = 0.4$, $Re = 500$, and $\alpha = 0$. (Multimedia view) [URL: http://dx.doi.org/10.1063/1.4926622.4]

For $St_c = 0.4$, the efficiency presents a local maximum. The main difference with the case $St_c = 0.5$ is that the LEV of each previous half stroke when $St_c = 0.4$ is shed out from the airfoil before the end of the current half stroke (at $3T/8$ and $9T/8$, approximately), thus generating drag during less time [see Fig. 5.9 and compare with Figs. 5.5(g) and 5.5(h)], i.e., the shedding LEV does not generate drag during the full second half of each half stroke, because in the final part, it is too far from the airfoil. The other contributions remaining similar, this difference yields a larger output thrust and efficiency than for $St_c = 0.5$. For $0.5 < St_c < 0.9$, the flow is very similar to that for $St_c = 0.5$, and $\overline{W}_o$ remains almost constant. However, $\bar{\eta}$ increases with St_c because the input work $\overline{W}_i$ decreases with St_c (see Fig. 5.7). When St_c reaches the value 0.9, approximately, the LEV remains attached to the LE, it is no longer completely shed

during each stroke and the total thrust increases, as already explained above. The mean thrust efficiency reaches a maximum at this frequency.

5.4.2 *Thrust efficiency for $\alpha = 0$*

We summarize here the results for several values of St_a ranging from 0.12 to 0.24 (i.e., for $1.35 \gtrsim J \gtrsim 0.66$) when $\alpha = 0$ and $Re = 500$. As commented on above, in the case that the flow does not become periodic with the same frequency as the heaving motion, we average the integrated works W_i and W_o and the corresponding efficiencies over a sufficiently large number of cycles n such that the relative error in the mean efficiency $\overline{\eta}$ is smaller than 2.5%. For strongly aperiodic flows, the number of cycles n needed may be quite large. For this reason, when the flow is aperiodic, we first average over 300 cycles and check that the relative error is less than 2.5%. For instance, for $St_a = 0.24$ and $St_c = 1.4$ (Fig. 5.10), this criterium is satisfied with $n = 300$ (Fig. 5.11). If it is not so, we use larger values of n until the criterium is met, but that happens only for a few number of cases among those reported here.
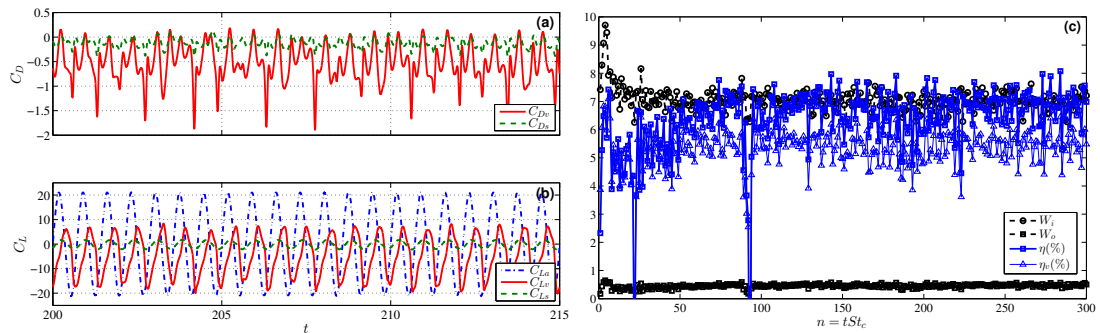
Figure 5.10: Different components of C_D (a) and C_L (b) vs. t (only the last time interval computed is shown) for $Re = 500$, $\alpha = 0$, $St_a = 0.24$, and $St_c = 1.4$. (c) Input and output works, W_i and W_o, and efficiencies η and η_v vs. the increasing number of cycles n for the same case.

Figs. 5.12 and 5.13 show $\overline{W}_o$, $\overline{W}_i$, $\overline{\eta}$, and $\overline{\eta}_v$, as functions of the frequency St_c for the four values of St_a considered. For the sake of clarity of the figures, we omit the error bars that characterize the standard deviations of the mean values when the flow is not periodic with the heaving frequency (the standard deviations are given later together with a discussion on the periodic or aperiodic character of the flow in the different cases). $\overline{W}_i$ increases with St_a for a given St_c, and so does $\overline{W}_o$. The qualitative behavior of these average works with St_c is quite similar for all St_a. Since $\overline{W}_o$ has a pronounced maximum when St_c is near unity for all St_a for which $\overline{W}_o$ is positive (as already explained for $St_a = 0.16$ in Sec. 5.4.1), the maximum efficiency is reached when St_c is close to unity and for a value of St_a around 0.2. More concretely, among all the case computed here, the maximum efficiency ($\overline{\eta}_{max} \simeq 9.3\%$) is reached for $St_c = 0.8$ when $St_a = 0.2$ [Fig. 5.13(a)], which corresponds to a reduced frequency of $k \simeq 5$ and an advance ratio $J \gtrsim 0.8$. These values for optimal thrust in forward flight of a horizontal 2D heaving wing are in agreement with previous experimental and numerical works for different airfoil geometries and Reynolds numbers as can be seen in Triantafyllou et al. (1993), Triantafyllou et al. (1991), Lentink and Gerritsma (2003), Taylor et al. (2003),
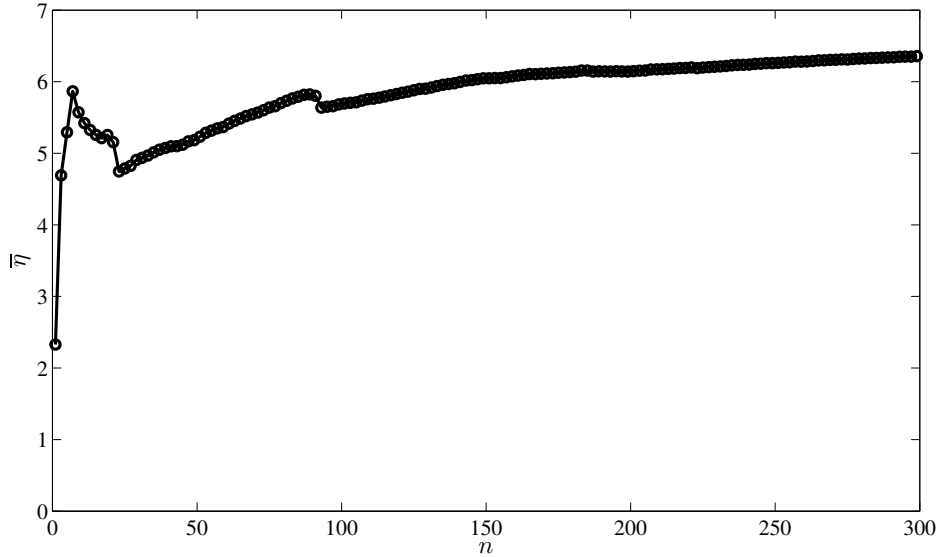
Figure 5.11: Average value of the efficiency $\overline{\eta}$ as a function of the number of cycles used for computing the mean. $St_a = 0.24$, $St_c = 1.4$, $Re = 500$, $\alpha = 0$.

Lewin and Haj-Hariri (2003), Wang (2000) and Young and Lai (2007))(note that the Strouhal number St used in some of the cited experimental works is $St = 2St_a$). In particular, Lewin and Haj-Hariri (2003) who used a different (more efficient) airfoil profile for the same Reynolds number, found that the maximum efficiency (of about 11%) is reached at practically the same frequency and amplitude: $St_c \simeq 0.85$ and $St_a \simeq 0.19$.
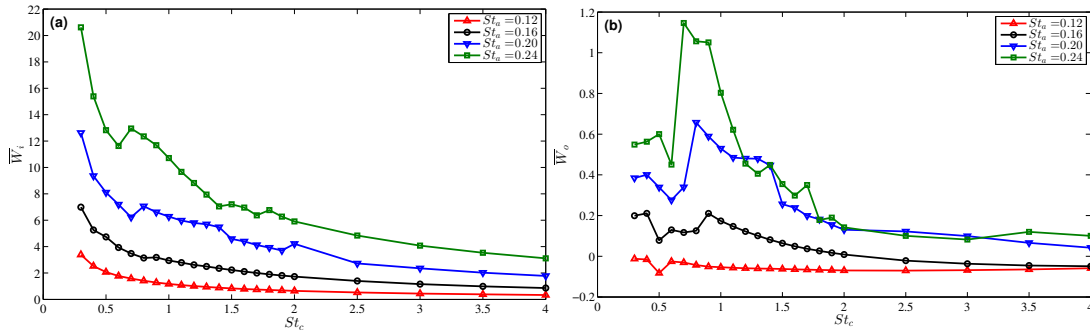
Figure 5.12: $\overline{W}_i$ and $\overline{W}_o$ vs. St_c for the four values of St_a considered. $Re = 500$ and $\alpha = 0$.

For a better characterization of the optimum values of the heaving frequency and amplitude that generate the maximum average thrust efficiency, we plot in Fig. 5.14 the contours of constant $\overline{\eta}$ and constant $\overline{\eta}_v$ in the plane (St_c, St_a) using linear interpolation of the numerical data contained in Fig. 5.13. It is observed that $\overline{\eta}$ is larger than 8.8% (top contour line in Fig. 5.14) in a region $0.79 \leq St_c \leq 0.9$ and $0.19 \leq St_a \leq 0.22$, approximately, with the maximum value very close to the case $St_c = 0.8$ and $St_a = 0.2$ already commented on. This maximum of η corresponds to a flow that eventually becomes periodic with the heaving frequency, so that $\overline{\eta} = \eta$. But the flow is aperiodic for larger heaving frequencies when $St_a = 0.2$: As characterized in Fig. 5.15 by error bars, the flow is no longer periodic for $St_c 1.5$. To illustrate this, Fig. 5.16 compares the
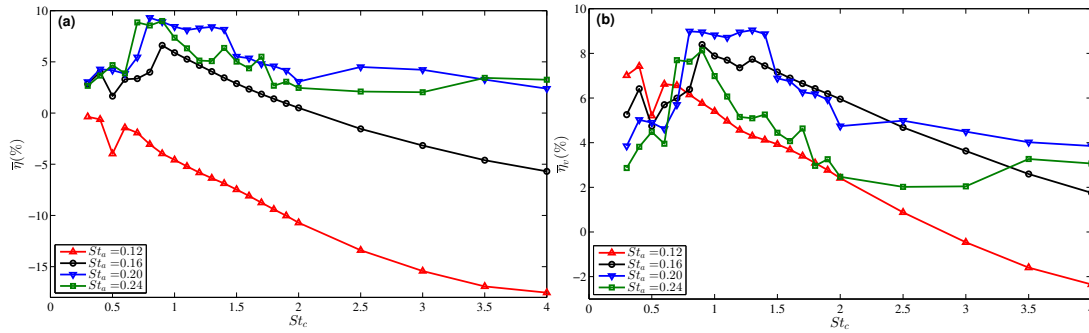
Figure 5.13: $\overline{\eta}$ and $\overline{\eta}_v$ vs. St_c for the four values of St_a considered. $Re = 500$ and $\alpha = 0$.

efficiency η as a function of the number of cycles $n = St_c t$ for the frequencies $St_c = 0.8$, $St_c = 1.5$, and $St_c = 2$, the first one corresponding to a periodic flow (actually, the most thrust efficient one), the second one to an aperiodic flow, and the third one to a quasiperiodic flow. As noted by Blondeaux et al. (2005), very long simulations are needed in some cases to observe the chaotic flow, for sometimes it is preceded by a long quasi-periodic flow. These different behaviors are better identified by using phase diagrams of, for instance, C_L vs. C_D, for the fully developed flow [see Figs. 5.16(d)–5.16(f)]. A limit cycle is reached for periodic and quasi-periodic flows, with several frequencies in the later case, while the phase diagram is chaotic for aperiodic flows (for the sake of clarity, only a few cycles are plotted in this later case).

The flow for the optimum case $St_c = 0.8$ with $St_a = 0.20$ is quite similar to that described in Fig. 5.6(d) for the optimum case $St_c = 0.9$ when $St_a = 0.16$. The main qualitative difference is that now ($St_a = 0.20$) the flow is periodic with the heaving frequency, while for $St_a = 0.16$, the flow became periodic with a frequency four times smaller than the heaving frequency. But both share the main characteristic that most part of the LEV generated in each half stroke remains attached near the leading edge during the subsequent half strokes, where it is stretched and diffused, so that a region of positive thrust ($\delta_{Dv} < 0$) is always present around the LE, maximizing the thrust efficiency. In the present case, a small fraction of the LEV generated in any half stroke, which is stretched during the next one, splits and moves around the LE, being shed during the following half stroke on the opposite airfoil surface and then joins and re-inforces the TEV (of the same sign) corresponding to that half stroke (see Fig. 5.17). Since this process repeats every cycle, the flow is periodic with the heaving frequency.

However, for the higher frequency $St_c = 1.5$ (Fig. 5.18), a large fraction of the LEV generated in a previous half stroke moves around the LE to the other part of the airfoil, as in Fig. 5.8 for $St_c = 1.2$ and $St_a = 0.16$, generating more drag and reducing the total thrust and mean efficiency in relation to $St_c = 0.8$. But now, with the higher amplitude and frequency of the oscillations, a given LEV is split several times in successive half strokes, each fraction being convected downstream along one of the airfoil surfaces. Since these LEV portions are not always of the same size in successive strokes, and due also to their interactions with TEVs of equal and opposite sign, the flow becomes chaotic [Fig. 5.16(e)] and the efficiency aperiodic [Fig. 5.16(b)]. This transition from periodic to chaotic behaviors for sufficiently high frequencies and amplitudes has been documented for the 2D flow over a plunging airfoil at low Re by several authors for
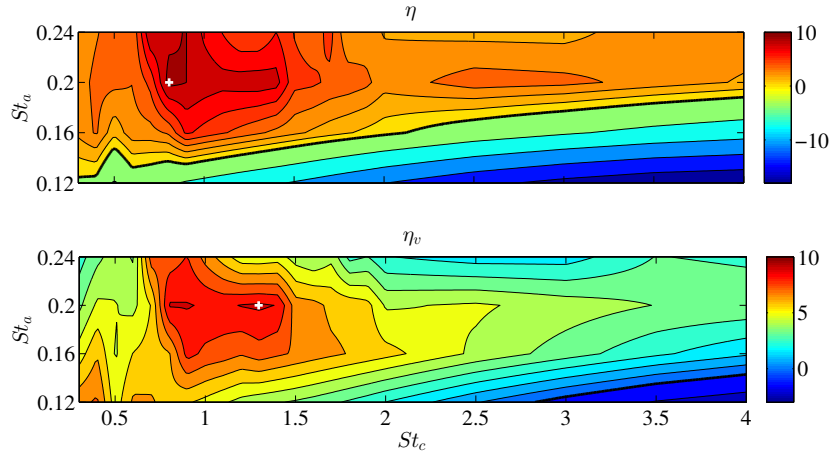
Figure 5.14: Contour plot of $\overline{\eta}$ (top) and $\overline{\eta}_v$ in the $(St_c, St_a)-$plane. $Re = 500$ and $\alpha = 0$. The thick lines separate positive from negative values and the white crosses mark the locations of the maximum values.
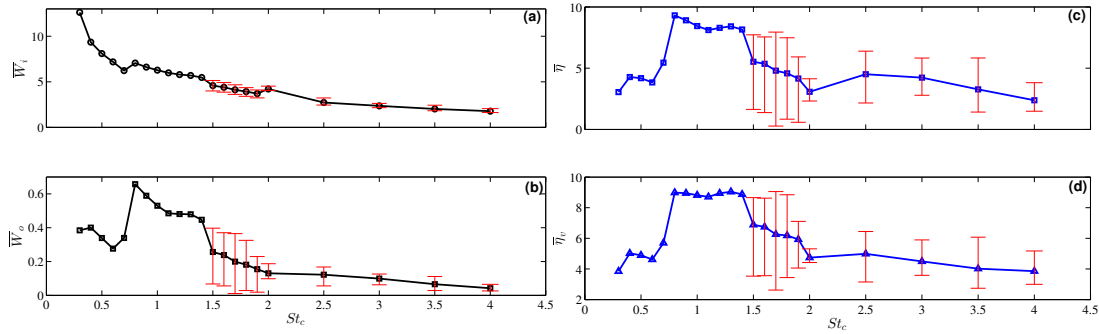
Figure 5.15: $\overline{W}_i$ (a), $\overline{W}_o$ (b), $\overline{\eta}$ (c), and $\overline{\eta}_v$ (d) as functions of St_c for $St_a = 0.20$, $Re = 500$, and $\alpha = 0$. The error bars characterize the standard deviations of the mean values when the flow is not periodic with the heaving frequency.

different airfoil geometries and Reynolds numbers (see Lentink and Gerritsma, 2003, Lewin and Haj-Hariri, 2003, Blondeaux et al., 2005, Zheng and Wei, 2012 and Wei and Zheng, 2014. Three-dimensional numerical simulations by Asraf et al. (2012) of the flow over a plunging NACA0012 airfoil at a higher Re confirmed the chaotic behavior of forces with the increase in plunging amplitude found from 2D analysis at the same Re.

To finish this section, we characterize in a single plot (Fig. 5.19) the type of flow for the different values St_c and St_a when $\alpha = 0$ by the standard deviation of the oscillations in η. This quantity is obviously zero when the flow is periodic with the heaving frequency (marked with P in the figure) and different from zero both for aperiodic flows (AP) and for periodic flows with a different frequency (PO).

5.4.3 *Thrust efficiency for $\alpha \neq 0$*

To analyze the effect that a mean angle of attack α different from zero has on the vortex structure of the flow and, consequently, on the thrust efficiency, we consider in
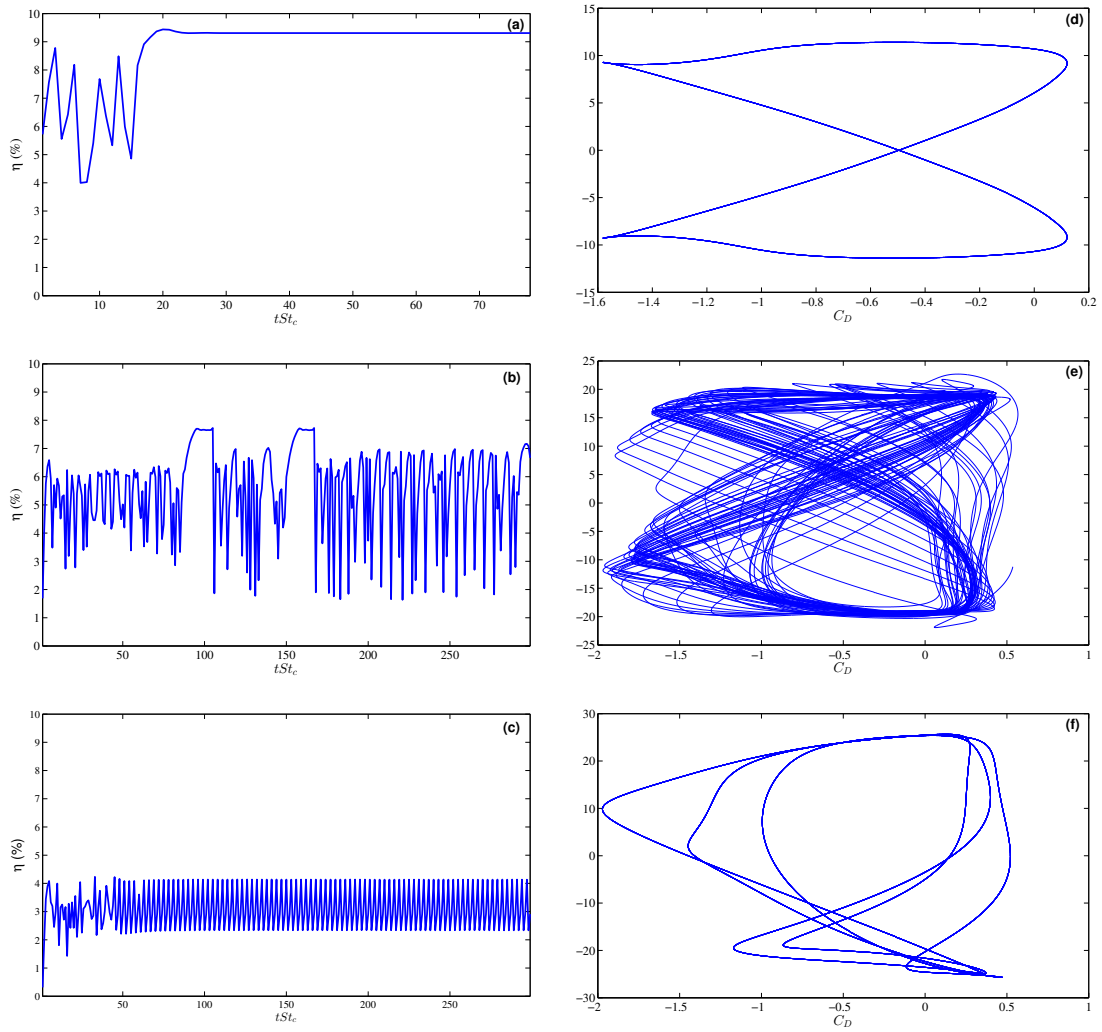
Figure 5.16: (a)–(c) η vs. $n = tSt_c$, (d)–(f) phase diagrams of C_L vs. C_D, for $St_a = 0.20$, $Re = 500$, $\alpha = 0$, and $St_c = 0.8$ [(a) and (d)], $St_c = 1.5$ [(b) and (e)], $St_c = 2$ [(c) and (f)].
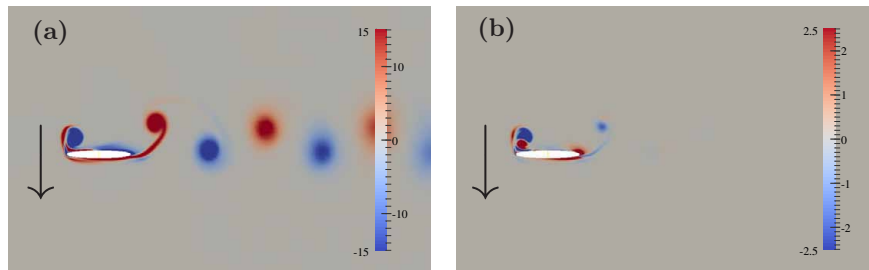
Figure 5.17: Snapshots of $\boldsymbol{\omega}$ (a) and of δ_{Dv} (b) at the instant $T/2$ within a stroke for $St_a = 0.20$, $St_c = 0.8$, $Re = 500$, and $\alpha = 0$. (Multimedia view) [URL: http://dx.doi.org/10.1063/1.4926622.5]

this section several cases for St_c and St_a close to their values of maximum efficiency when $\alpha = 0$. Since the problem is symmetric with respect to $\alpha = 0$, only values $\alpha \leq 0$ are considered.
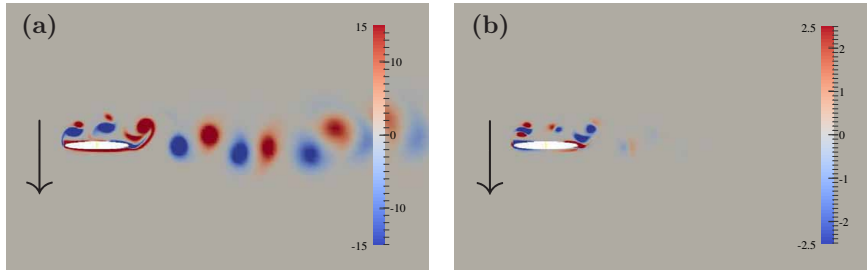
Figure 5.18: Snapshots of ω (a) and of δ_{Dv} (b) at the instant $T/2$ within a stroke for $St_a = 0.20$, $St_c = 1.5$, $Re = 500$, and $\alpha = 0$. (Multimedia view) [URL: http://dx.doi.org/10.1063/1.4926622.6]
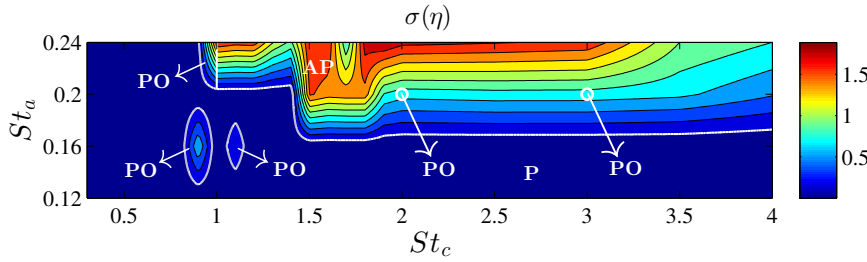
Figure 5.19: Contour plot of the standard deviation of η (top) and η_v (bottom) in the (St_c, St_a)−plane. $Re = 500$ and $\alpha = 0$. The thick lines separate the regions with a periodic flow with the heaving frequency (P), the regions with aperiodic flows (AP), and the regions with periodic flows but with different frequencies (PO).
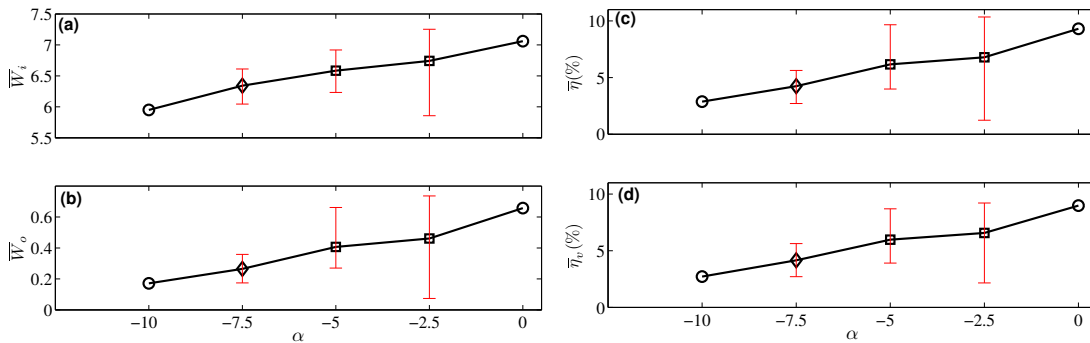
Figure 5.20: $\overline{W}_i$ (a), $\overline{W}_o$ (b), $\overline{\eta}$ (c), and $\overline{\eta}_v$ (d) as functions of α (in degrees) for $St_a = 0.20$, $St_c = 0.8$, $Re = 500$. Circles correspond to periodic flows with the heaving frequency. The error bars characterize the standard deviations of the mean values when the flow is not periodic with the heaving frequency (squares correspond to aperiodic flows and diamonds to quasi-periodic flows).

Fig. 5.20 shows the results as α varies from $-10°$ to $0°$ for the case $St_a = 0.20$ and $St_c = 0.8$, the most thrust efficient one when $\alpha = 0$. It is observed that the largest mean efficiency $\overline{\eta}$ remains for $\alpha = 0$ and that the flow is no longer periodic with the heaving frequency even for small $|\alpha|$. In particular, the flow becomes aperiodic for $\alpha = -2.5°$. This is because, compared to the flow with $\alpha = 0°$ (Fig. 5.17), the trajectories of the split fractions of the LEV that move around the LE and are shed on the opposite airfoil surfaces depend on whether the LEV was generated during the
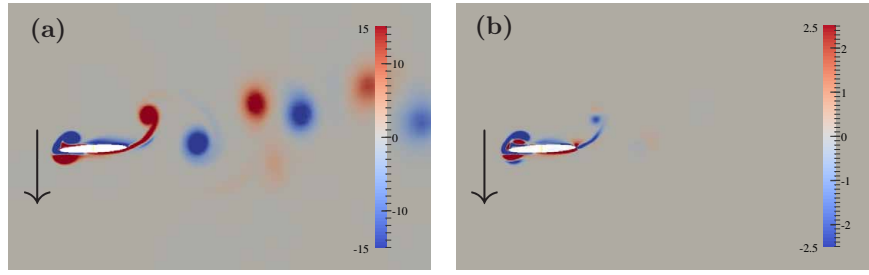
Figure 5.21: Snapshots of $\boldsymbol{\omega}$ (a) and of δ_{Dv} (b) at the instant $T/2$ within a stroke for $St_a = 0.20$, $St_c = 0.8$, $Re = 500$, and $\alpha = -2.5°$. (Multimedia view) [URL: http://dx.doi.org/10.1063/1.4926622.7]
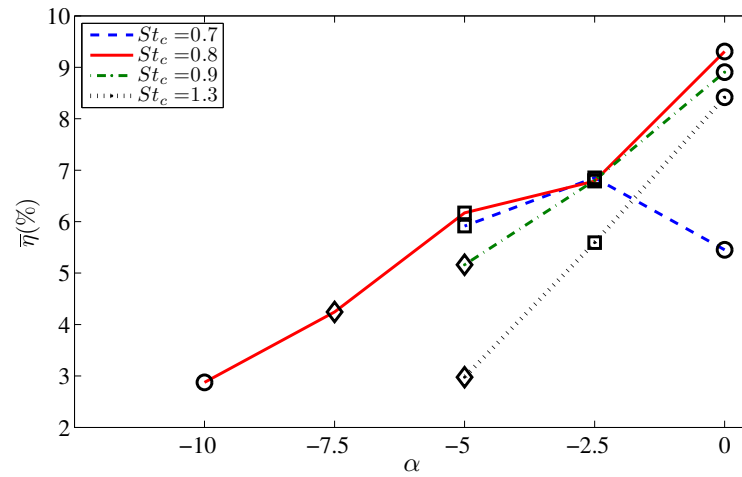
Figure 5.22: $\overline{\eta}$ vs. α (in degrees) for $St_a = 0.20$, $Re = 500$, and different values of St_c (as indicated). Circles correspond to periodic flows with the heaving frequency, squares to aperiodic flows, and diamonds to quasi-periodic or periodic flows with a different frequency (the error bars characterizing the standard deviations of the mean values are not shown for simplicity).

up- or the down-stroke. This up-down asymmetry generates a deflected wake and an aperiodic flow (see Fig. 5.21). The flow remains aperiodic as $|\alpha|$ increases, becoming quasi-periodic or periodic with a different frequency, for $|\alpha| = 7.5°$, and periodic again for $|\alpha| = 10$ (this is marked in Fig. 5.20 with different symbols).

We have repeated the computations as $|\alpha|$ increases for several values of St_a and St_c. The results are summarized in Figs. 5.22–5.24. The trends are quite similar to the case commented on above, with periodic flows for $\alpha = 0$ in the cases of interest (maximum averaged thrust efficiency), aperiodic for small $|\alpha|$, becoming quasi-periodic and periodic again as $|\alpha|$ increases in most cases. Also, for most St_a and St_c, the maximum $\overline{\eta}$ takes place at $\alpha = 0$. The situation is more irregular for the largest heaving amplitude considered ($St_a = 0.24$, Fig. 5.24), where the flow may become aperiodic or quasi-periodic for $\alpha = 0$ or periodic for $|\alpha| = 0$ small, depending on the value of St_c. Finally, it is noteworthy that the most thrust efficient configuration among all the
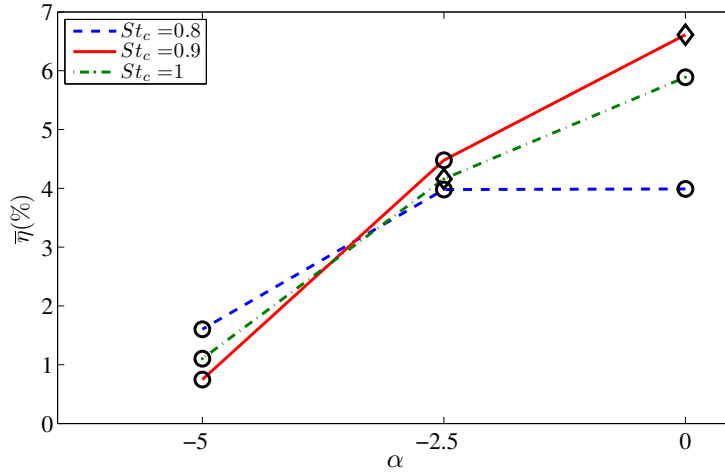
Figure 5.23: As in Fig. 5.22, but for $St_a = 0.16$.
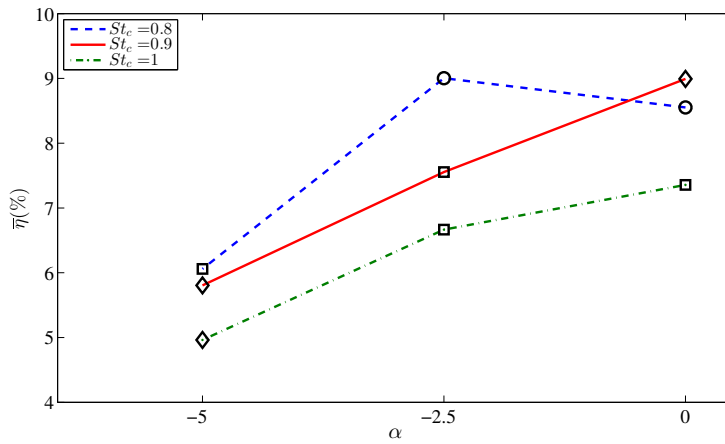
Figure 5.24: As in Fig. 5.22, but for $St_a = 0.24$.

cases considered corresponds to $\alpha = 0$ when $St_a = 0.2$ and $St_c = 0.8$, a case described with detail in Sec. 5.4.1.

5.5 CONCLUSIONS

We have conducted 2D numerical simulations of the flow around a heaving elliptic airfoil for different values of the mean angle of attack α, amplitude and frequency of the heaving motion, St_a and St_c, and for a given low Reynolds number ($Re = 500$) of interest in MAVs and insect flapping flight. The vortex force decomposition used in this work yields analytic expressions for added-mass contributions to the lift and drag force components for any heaving motion of the elliptic airfoil for any α. This circumstance permits an additional validation of the numerical code. More importantly, the vortex force formulation allows for a quantitative characterization of the thrust (or drag) and lift force components exerted by any particular vortex structure of the flow on the

airfoil. Basically, we find that thrust is mainly generated by the growing LEV during the initial part of each half stroke and by the shedding TEV of the previous half stroke when it is still near the airfoil. On the other hand, drag is mainly generated by the growing TEV during the initial part of each half stroke and by the shedding LEV of the previous half strokes (depending on the frequency and amplitude, St_c and St_a) when stretched by the current half stroke. Using these mechanisms, we explain quantitatively the configurations of maximum thrust efficiency in terms of vortex flow structure and interaction. We find that for the present heaving elliptic airfoil at $Re = 500$, the maximum thrust efficiency is reached for $St_a \simeq 0.2$ and $St_c \simeq 0.8$ with $\alpha = 0$. This configuration corresponds to a periodic flow with the heaving frequency. As another interesting result we find that as $|\alpha|$ increases slightly from zero, this thrust efficient flow becomes aperiodic and the average thrust efficiency decreases.

5.A APPENDIX A: VALIDATION OF THE NUMERICAL CODE

To validate further the numerical code, we compare with several published results and make a mesh convergence analysis for an extreme case among those considered in this work.
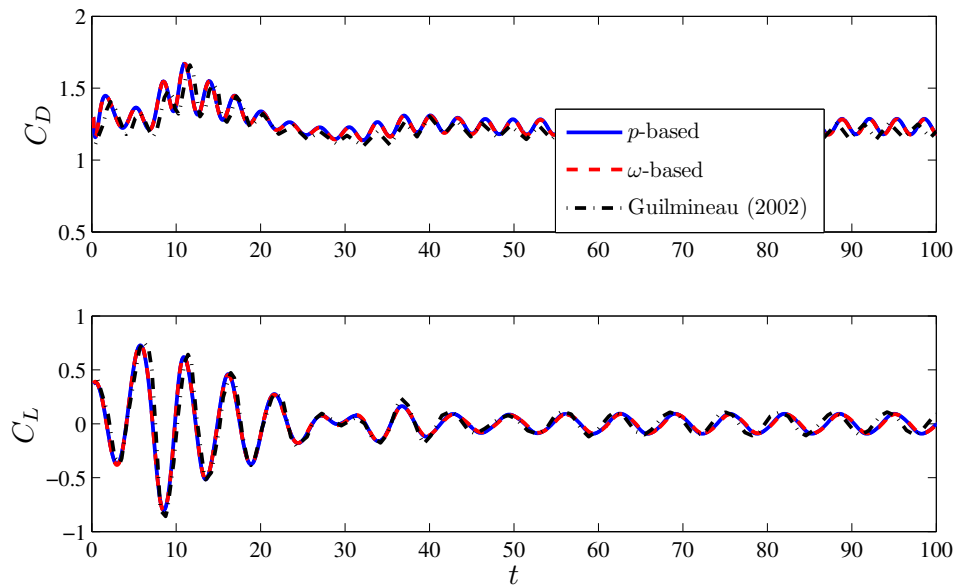
Figure 5.25: Comparison of $C_D(t)$ and $C_L(t)$ for an oscillating cylinder ($\epsilon = 1$, $Re = 185$, $St_a = 0.308$, $St_c = 0.154$) with the results by Guilmineau and Queutey (2002) [their Fig. 10(a)]. Mesh = 120×100, $\Delta t = 0.002$, $R_o = 25$. Absolute error norm from the $p-$based formulation (C_D, C_L): $\|L\|_\infty = (0.07, 0.0764)$ at $t = (63.52, 39.482)$.

Figs. 5.25–5.27 show the temporal evolutions of C_D and C_L for three cases: an oscillating cylinder ($\epsilon = 1$) at $Re = 185$, an oscillating horizontal ($\alpha = 0$) ellipse with $\epsilon = 0.02$ at $Re = 83.2$, and an oscillating horizontal ellipse with $\epsilon = 1/8$ at $Re = 1000$. They are compared with the numerical results by Guilmineau and Queutey (2002),
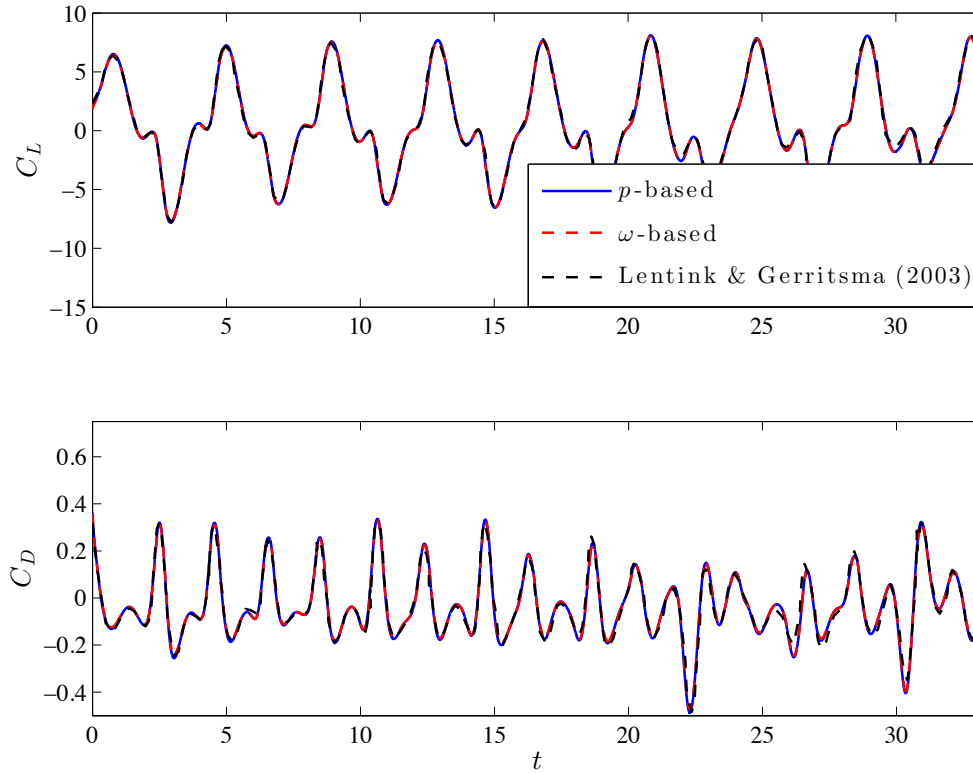
Figure 5.26: Comparison of $C_D(t)$ and $C_L(t)$ for an oscillating ellipse ($\epsilon = 0.02$, $Re = 83.2$, $St_a = 0.375$, $St_c = 25$) with the results by Lentink and Gerritsma (2003) (their Fig. 25). Mesh $= 249 \times 249$, $R_o = 25$, $CFL_{max} \leq 0.5$. Absolute error norm from the $p-$based formulation (C_D, C_L): $\|L\|_\infty = (0.0859, 0.6685)$ at $t = (10.3, 5.3246)$.

Lentink and Gerritsma (2003), Wang (2000), respectively. All these researchers validate their numerical codes against some experimental results, and in the three cases, we use the same meshes and time steps (when the information is available) as they used in their computations (see figure captions). In spite of the very different numerical methods used (for instance, these authors used non-inertial references frames moving with the oscillating cylinder or ellipse), the agreement is quite good in all cases. In particular, in the case of Fig. 5.27, the results are practically identical, including the bifurcation in the evolution of C_D at $t \simeq 22.4$.

In these plots, we have included the computations of $C_D(t)$ and $C_L(t)$ using both pressure-based formulations (8) and (9) and vorticity-based formulations (12) and (13). It is observed that the results are indistinguishable in all cases, thus validating further the numerical implementation of the different integrals used for the computations of these forces in both formulations. As an example, Fig. 5.28 shows the different components of C_D and C_L in vorticity force decompositions (12) and (13) for the case computed in Fig. 5.27.

Finally, to ascertain the effects of the grid refinement on the solution, we consider a heaving ellipse with $\epsilon = 1/8$ at $Re = 1000$ (which is twice the value used in the reported
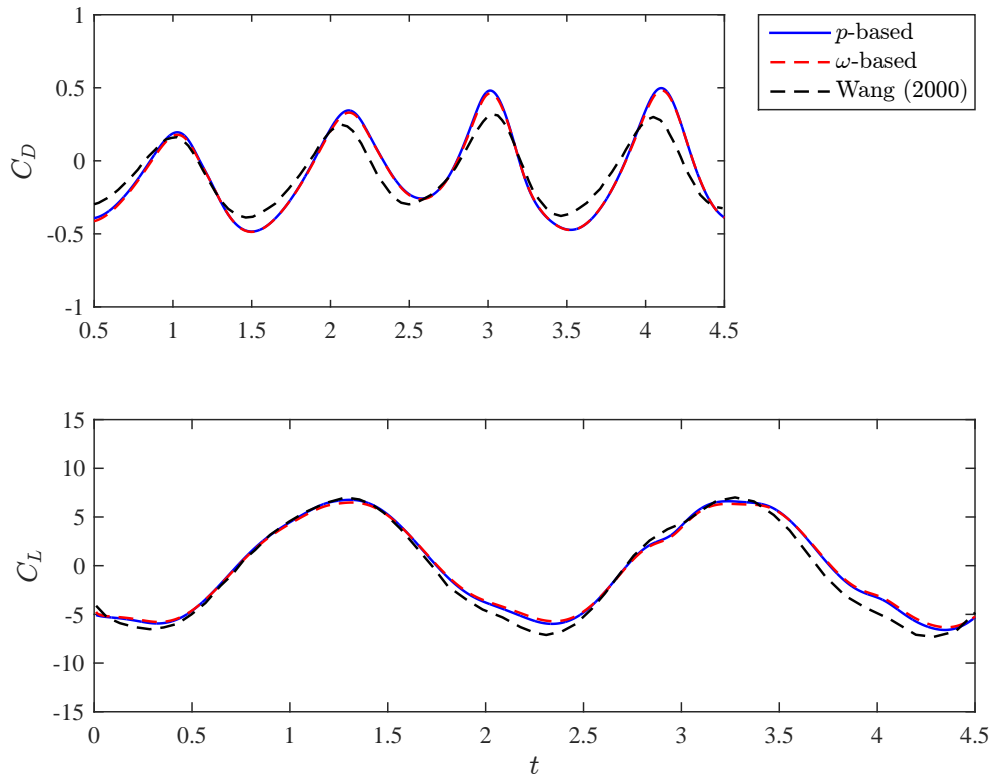
Figure 5.27: Comparison of $C_D(t)$ and $C_L(t)$ for an oscillating ellipse ($\epsilon = 1/8$, $Re = 1000$, $St_a = 0.16$, $St_c = 0.5$) with the results by Wang (2000) (Fig. 3 of this author). Mesh $= 256 \times 256$, $R_o = 5$, $CFL_{max} \leq 0.5$. Absolute error norm from the $p-$based formulation (C_D, C_L): $\|L\|_\infty = (0.2661, 1.6365)$ at $t = (3.6685, 4.023)$.

Mesh	n_θ	n_r	Mesh nodes	$C_{L,max}$	$GCI_{i+1,i}$ (%)	Relative CPU time
#1	512	512	262 144	7.379 586	0.670 338 417	18.9
#2	362	362	131 044	7.396 075	1.028 742 892	9.2
#3	256	256	65 536	7.421 438	1.575 745 917	3.3
#4	181	181	32 761	7.460 419	. . .	1

Table 5.1: $C_{L,max}$ for a heaving ellipse with $\epsilon = 1/8$ for $Re = 1000$, $St_a = 0.16$, and $St_c = 0.637$, computed with four meshes of decreasing grid refinement (grid refinement ratio $\varphi = \sqrt{2}$). $R_o = 30$ in all cases. Also shown is the grid convergence index (GCI) as introduced by Roache (1994), and the computation time relative to that using the coarsest grid #4.

results of Sec. 5.4), $St_a = 0.16$ and $St_c = 0.637$ (corresponding to a periodic flow with the heaving frequency). Table 5.1 shows the peak value of C_L, once a permanent state is reached, computed with four meshes of decreasing refinement, with a grid refinement ratio for each coordinate $\varphi = \sqrt{2}$, a computational domain size $R_o = 30$, and a maximum Courant number less or equal than 0.5. Table 5.1 includes the grid convergence index (GCI) introduced by Roache (1994), which is a more conservative measure of the relative error between the solution obtained on a given grid and the asymptotic
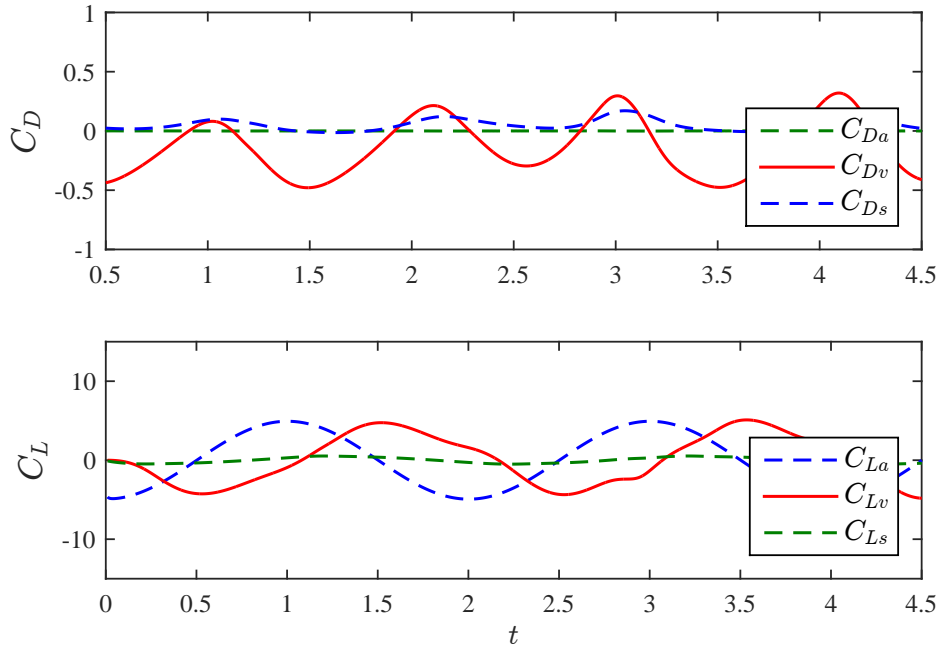
Figure 5.28: Different components of $C_D(t)$ and $C_L(t)$ in vorticity-based formulations (12) and (13) for the same case plotted in Fig. 5.27.
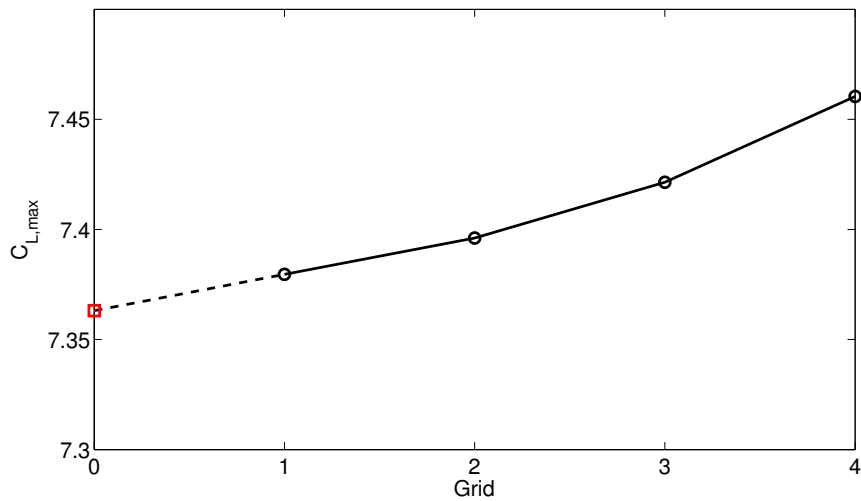
Figure 5.29: $C_{L,max}$ computed with the different meshes described in Table 5.1 compared with that obtained by the Richardson extrapolation (square), which can be considered as an acceptable approach to the limit value calculated on a mesh with theoretically zero grid spacing.

value than the estimated fractional error derived from the Richardson extrapolation. Nonetheless, Fig. 30 shows the Richardson extrapolation together with the computed values for decreasing grid refinement. From this grid convergence analysis, we select the mesh #3 (256 × 256 grid points) for all the computations reported in the main text, since the *GCI* is relatively low and the CPU time is about 6 times smaller than

with the finest mesh #1.

CLOSURE

6.1 CONTRIBUTIONS OF THIS THESIS

The vortex force decomposition developed by Chang (1992), is employed in this thesis to face computationally two aerodynamic problems using the open source code OpenFOAM®. The main aim is to contribute to the understanding of the flow dynamics present in low-Reynolds flapping-like MAVs.

A brief description of the formulation is first introduced in Chapter 2, to be later characterized for each one of the problems studied in Chapters 4 and 5. The unusual and novel discussion of the results from the point of view of the vortex force decomposition is the most relevant contribution of this dissertation. According to Chang (1992), the aerodynamic coefficients can be decomposed into accelerating, rotational, volumetric and superficial contributions. Some conclusions are drawn at the end of the cited Chapters taking advantage of this decomposition.

On the other hand, a summary of the OpenFOAM® framework and the Finite Volume Method is given in Chapter 3. As an example, the reader can figure the software abilities and examine a relevant part of the code used in this thesis.

In Chapter 4, numerical simulations are conducted to investigate the *Magnus Effect* following the formulation by Chang (1992). Two cases are studied: (i) an accelerating cylinder starting from rest to a given velocity with constant angular velocity, and (ii) a constant inlet flow around a spinning cylinder accelerating from rest to a given angular velocity. It is concluded that, especially for the case of lift, the main contribution comes from the volume elements and it is quantified and compared for different configurations of (i) and (ii).

In Chapter 5, the optimal thrust efficiency for a 2D flapping foil in a uniform flow is analyzed numerically in terms of the formulation of Chang (1992). In that case it is found that the maximum thrust efficiency is reached for $St_a \simeq 0.2$ and $St_c \simeq 0.8$, when $\alpha = 0$. This configuration is explained quantitatively in terms of vortex flow structures and their interactions between themselves and the flapping foil.

Another contribution of this thesis is the implementation of the different magnitudes appearing in the formulation of Chang in the OpenFOAM® framework. Thus, for each problem faced in this thesis, it is possible to access the value of every contribution to the aerodynamic forces in each time step and, therefore, to the corresponding temporal evolution.

6.2   FUTURE WORK

The natural next step following the present work is to use the vortex force decomposition of Chang (1992), within the OpenFOAM® code, to analyse the lift and thrust of more complex configurations such as a flapping foil with pitching and heaving motions, and the interaction between two or more flapping and pitching wings (tandem flight).

However, the deforming mesh employed to perform a sinusoidally vertical motion in Chapter 5 ceases to be valid when more complex kinematics and larger amplitudes are considered, or when several moving bodies take part in a same problem. It would generate strong cell deformations and a high skewness ratio within the computational mesh, which could affect the stability of the simulations and the accuracy, enormously.

More versatile methods such as the Immersed Boundary Method (see e.g. Peskin, 1972, Peskin, 2002, Uhlmann, 2005, Mittal and Iaccarino, 2005, Taira and Colonius, 2007 and Pinelli et al., 2010), are proposed in order to be associated with the formulation of Chang (1992). The Immersed Boundary Method was first introduced by Peskin (1972) and a large amount of modifications and improvements have been achieved since then. In this method a surface lagrangian mesh is immersed in a background eulerian grid and the presence of the immersed body is taken into account by means of a fictitious body force introduced in the Navier–Stokes equations.

The Immersed Boundary Method is a *mesh-free* method which can be modeled regardless of the equations discretization approach chosen (Finite Volume, Finite Element or Finite Difference Methods). But it suffers from accuracy when compared with a conformal mesh mostly due to the violation of the non-slip condition on the body surface as stated by Breugem (2012) and by Kempe and Fröhlich (2012). These authors proposed an additional corrector loop to deal with the non-slip restriction to converge the velocity field before solving the Poisson problem in the solution of the Navier–Stokes equations in primitive variables. Another solution is proposed by Lechner and Kuhlmann (2011), based on the work of Taira and Colonius (2007). These solutions can however affect the code efficiency due to the convergence of an additional constraint.

Another and more efficient solution when dealing with the Immersed Boundary Method lies in formulating it along with the Lattice Boltzmann equations (Immersed Boundary–Lattice Boltzmann Method). These equations also govern a fluid flow with the advantage of not presenting coupled variables, being a second-order method (more information can be found in Succi, 2001). Some of the more recent works using this method applied to flapping flight aerodynamics are Inamuro (2012), Rosis et al. (2014), Favier et al. (2014), Minami et al. (2014), Wu and Shu (2015), Wang et al. (2015), Rosis and Lévêque (2015), Rosis (2015), and Suzuki et al. (2015).

Finally, after improving the efficiency and accuracy in the Immersed Boundary Method, the study of three-dimensional problems is as well suggested as a future work. In fact, this extrapolation would be straightforward when a deforming mesh such as the one used in Chapter 5 is used. Nevertheless, for the sake of clarity and efficiency

when analyzing the flow structures according to the formulation by Chang (1992), only 2D problems have been considered in this thesis. As an example, the wing-tip vortex contribution to the drag and lift coefficients could be understood as well as its interactions with the LEV and TEV. The same procedure can be followed to study from the point of view of the formulation of Chang (1992) another relevant static problems such as the three-dimensionality in a 3D spinning cylinder, or even simpler: the flow around a bluff body.

A

A.1 INTRODUCCIÓN

La aerodinámica no estacionaria de alas batientes a bajos números de Reynolds –en el rango de interés de pequeños insectos voladores– ha sido fruto de numerosos estudios tanto teóricos, como numéricos o experimentales. Muchos de estos estudios han venido motivados por la identificación de los mecanismos del flujo por los cuales las fuerzas de sustentación son mucho mayores que las predichas por la teoría quasi-estacionaria, y de los mecanismos que generan las fuerzas de propulsión o empuje. Tradicionalmente, estos estudios se han centrado en la investigación de la biomecánica de los insectos (y pequeños pájaros y mamíferos) voladores (ver e.g. Maxworthy, 1981; Dudley, 2000; Sane, 2003 and Wang, 2005). Pero en los últimos años, el interés en el estudio de la aerodinámica de alas batientes ha experimentado un enorme crecimiento que ha venido motivado por el diseño de Micro-Vehículos Aéreos (MAVs, siglas en inglés). Estos vehículos han ido haciendo uso del conomiciento generado en el campo de la aerodinámica de animales para su desarrollo (Ellington, 1999; Mueller, 2001; Pines and Bohorquez, 2006; Ansari et al., 2009 and Jones and Platzer, 2009).

Así pues, el tema central de esta tesis es el análisis de las fuerzas aerodinámicas en problemas no estacionarios a números de Reynolds relativamente bajos, haciendo uso de la descomposición de fuerzas mediante vórtices desarrollada originalmente por Chang (1992). Esta formulación proporciona de manera cuantitativa la contribución de cada vórtice a los coeficientes aerodinámicos en cada instante (ver e.g. Lee et al., 2012 and Martín-Alcántara et al., 2015). De esta manera es posible identificar los mecanismos involucrados en la propulsión y en la sustentación para ser utilizados en el diseño y desarrollo de MAVs. Para demostrar la eficacia de este nuevo enfoque se ha decidido aplicarlo al estudio de dos problemas clásicos de la mecánica de fluidos.

Por otra parte, los orígenes de los micro-vehículos aéreos datan de alrededor de 1997 (Ansari et al., 2006). Desde entonces, aunque se ha demostrado que las escalas pequeñas de los vehículos ya existentes son válidos en escenarios exteriores, su falta de eficiencia y efectividad en interiores. Por ejemplo, un modelo de avión carece de maniobravilidad en espacios cerrados y necesitaría grandes distancias para despegar y aterrizar. Sin embargo, un modelo de helicóptero (con una o más hélices) tiene la ventaja de su agilidad en estos escenarios pero es ruidoso e ineficiente. Por el contrario, los micro-vehículos de alas batientes son mucho más eficientes y ágiles que los modelos anteriores, pero equiparlos con una fuente de energía duradera es todo un reto. En el desarrollo de los micro-vehículos aéreos, el principal objetivo is predecir cuantitativamente el comportamiento de los fenómenos físicos que ocurren durante el vuelo, siendo el vehículo capaz de maniobrar cuando sea necesario para poder mantener un vuelo estable. Así pues, se requiere tener un completo conocimiento de la dinámica del flujo que aparece en este tipo de vuelos. Los trabajos que se estudian en esta tesis

UNIVERSIDAD
DE MÁLAGA

pretenden aclarar el estudio de los mecanismos del dlujo así como de las interacciones entre vórtices inherentes al vuelo de alas batientes, de manera que sea de utilidad e.g. cuando un micro-vehículo aéreo de alas batientes necesite volar en un modo óptimo de propulsión o generar una determinada sustentación.

Para lograr este objetivo se han estudiado computacionalmente dos problemas aerodinámicos mediante el software OpenFOAM®. Este software es un código abierto basado en el lenguaje de programación C++, por lo que ofrece toda la flexibilidad y eficiencia de un lenguaje orientado a objetos (OOP, del inglés *Object Oriented Programming*). Como aportación fundamental de la tesis, y a modo de ejemplo de la versatilidad que ofrece OpenFOAM®, hay que remarcar que el cálculo de las diferentes contribuciones de la formulación de Chang (1992), en la que se basa esta tesis, ha sido implementado apropiadamente en este software mediante la utilización de `functionObjects` (ver e.g. Stroustrup, 2013, OpenCFD, 2014 and Marić et al., 2014). De esta manera, se puede tener acceso a las diferentes contribuciones en cualquier instante ya que todas las magnitudes son calculadas durante el `runTime` de las simulaciones, con un coste computacional prácticamente inapreciable ya que se han utilizado mallas 2D.

El primero de estos problemas se aborda en el Capítulo 4 y se basa en el estudio del *Efecto Magnus.* Es bien conocido en aerodinámica y aeronaútica el interés en la generación de fuerzas de sustentación mediante *Efecto Magnus* en un cilindro que gira (Seifert, 2012). Por ello, se utiliza como un modelo relativamente simple para tratar de entender la generación, reducción o supresión de la sustentación y resistencia en flujos no estacionarios asociados con superficies sólidas en movimiento. Tanto para geometrías como para movimientos más complejos se trata de una tarea difícil dadas las intrincadas estructuras del flujo tridimensional asociado. Sin embargo, las estructuras bidimensionales del flujo alrededor de un cilindro que gira, para un número de Reynolds relativamente bajo, resultan más sencillas de analizar. En este problema se estudian numéricamente dos efectos transitorios: (i) un cilindro que se acelera desde el reposo cuando gira a una velocidad angular constante, y (ii) un cilindro que se traslada a velocidad constante y se acelera rotacionalmente desde el reposo. Para identificar los vórtices asociados a la generación y desarrollo de la sustentación y resistencia se ha utilizado la formulación desarrollada por Chang (1992), ya utilizada en otros modelos simples (e.g. Hsieh et al., 2009, Hsieh et al., 2010, Lee et al., 2012). Esto es incluso más interesante en el caso de un cilindro que gira y se traslada ya que la sustentación puede incrementarse sustancialmente al aumentar el grado de rotación, pudiendo cambiar también su régimen de oscilatorio a estacionario, mientras que la resistencia puede disminuir sustancialmente hasta casi desaparecer; por ello se pueden llegar a distinguir las estructuras que generan sustentación de aquellas que reducen la resistencia. Este enfoque podría ser de aplicación para entender los mecanismos de mejora de la sustentación y reducción de la resistencia en cuerpos con formas más complejas, especialemnte en cuerpos que giran (e.g. Jimémenez-González et al., 2013).

El segundo de los problemas (Capítulo 5) se basa en el estudio de la propulsión óptima de un perfil alar de forma elíptica que ejecuta un movimiento de batida sinusoidal en un flujo bidimensional, laminar e incompresible. Así, este problema se centra en la generación de la propulsión de un ala batiente a números de Reynolds bajos, en con-

creto en la caracterización de las estructuras de los vórtices responsables de la máxima eficiencia de empuje para los rangos de frecuencias y amplitudes adimensionales de las oscilaciones. Se considera un flujo bidimensional, laminar e incompresible, alrededor de un perfil que bate verticalemente con diferentes ángulos de ataque. Este problema tan simplificado, únicamente con movimiento de batida vertical, ha sido considerado por muchos como un modelo simple y apropiado para entender los mecanismos del flujo responsables de la generación de la propulsión en el vuelo y en el nado de las especies mediante alas/aletas batientes. Desde hace mucho tiempo se conoce que el empuje neto está caracterizado por la inversión de las calles de von Kármán que aparecen tras el ala batiente (Kármán and Burgers, 1935 and Bratt, 1950), donde se desarrollan vórtices que giran en sentido contrario a la dirección natural de los vórtices que se producen en las calles de von Kármán originales, y que generan resistencia. En muchas formas de propulsión utilizadas por especies marinas, se han identificado diferentes tipos de patrones de vórtices (ver e.g., Wu, 1961, Lighthill, 1969 and Lighthill, 1970). Además, en muchos de los mecanismos de propulsión propuestos, el vórtice que se genera en el borde de entrada (LEV, del inglés *Leading-Edge Vortex*) durante las batidas juega un papel fundamental en este aspecto. Es de sobra conocido que los elevados coeficientes de sustentación que caracterizan el vuelo de la mayoría de los insectos, se deben a la aparición de zonas de baja presión dentro del LEV que se ha desarrollado temporalmente durante la batida tras un cambio repentino en el ángulo de ataque local (ver Lighthill, 1975, Maxworthy, 1979, Dickinson and Götz, 1993, Ellington et al., 1996, Liu et al., 1998, Sane and Dickinson, 2001, Minotti, 2002, Maxworthy, 2007, Shyy and Liu, 2007 and Pitt and Babinsky, 2013). Para optimizar este efecto, la mayoría de los insectos vuelan al límite de la entrada en pérdida dinámica, generando un prominente LEV. La relevancia del LEV en la elevada eficiencia de propulsión de un movimiento de batida vertical se comenzó a estudiar mediante modelos simples relacionados con el nado de peces, tal y como demostraron Streitlien et al. (1996), Anderson et al. (1998) and Triantafyllou et al. (2000). Para entonces ya se conocía que la eficiencia de generación del empuje en un ala batiente venía dada por un número de Strouhal basado en la amplitud y frecuencia de las oscilaciones (St_a definido en Sec. 5.2) (véase Triantafyllou et al., 1993, Jones et al., 1996 and Lai and Platzer, 1999). Para St_a muy bajos, por debajo de un valor de 0.03, aproximadamente, el ala batiente únicamente produce resistencia como demostraron Lai and Platzer, 1999. Para mayores frecuencias y una amplitud dada, cuando $St_a \sim 0.06$, se produce una propulsión neta que es generada por la inversión de los vórtices de las calles de von Kármán que aparecen durante la batida del ala, como concluyeron Jones et al., 1996, Lai and Platzer, 1999 and Koochesfahani, 1989. Tanto los resultados numéricos como los experimentales demuestran que en un amplio rango de números de Reynolds (definido en Sec. 5.2), la eficiencia óptima para la generación de la propulsión se alcanza en un intervalo de valores intermedios de St_a, entre 0.12 y 0.20 aproximadamente, que es el seleccionado para el nado y vuelo por un gran número de especies (Triantafyllou et al., 1993, Triantafyllou et al., 1991, Lentink and Gerritsma, 2003 and Taylor et al., 2003). En relación a este hecho, Theodorsen, 1935 y Garrick, 1936 comprobaron que los resultados experimentales son muy diferentes a los que ofrece la teoría potencial para oscilaciones de pequeña amplitud, que predicen que la eficiencia de la propulsión se maximiza cuando la frecuencia de batida tiende a cero, de donde se comprueba la especial relevancia de los efectos viscosos al modelar la propulsión que genera un ala batiente para ciertos números de Reynolds

de interés. Esta frecuencia de batida que optimiza el empuje se ha relacionado con la frecuencia de mayor amplificación espacial de la estela, según los estudios de estabilidad lineal del perfil de velocidades medias en la misma (Triantafyllou et al., 1993 and Lewin and Haj-Hariri, 2003), y con la frecuencia natural de desprendimiento de vórtices en el ala (Lentink and Gerritsma, 2003). Este rango de frecuencias que se ha observado en la propulsión biológica también se ha relacionado con el rango de tiempo adimensional que limita el desarrollo óptimo de vórtices en un ala batiente.

Por último, el núcelo de esta tesis es el análisis de las fuerzas aerodinámicas para problemas no estacionarios a números de Reynolds relativamente bajos, utilizando la descomposición de fuerzas de Chang (1992). Esta formulación proporciona la contribución cuantitativa de cada vórtice del flujo a los coeficientes de las fuerzas aerodinámicas en cada instante de tiempo (ver Lee et al., 2012 y Martín-Alcántara et al., 2015). De esta forma, es posible explicar con más detalle los mecanismos que generan la sustentación y la propulsión para que puedan ser aplicados en el diseño de los micro-vehículos aéreos.

A.2   CONCLUSIONES

En esta tesis se ha utilizado la descomposición de fuerzas en términos de vorticidad desarrollada por Chang (1992) para abordar computacionalmente los problemas aerodinámicos presentes en los Capítulos 4 y 5. El interés principal de esta formulación radica en su aplicación a la hora de tratar de entender la dinámica del flujo presente en micro-vehículos aéreos (MAVs, del inglés *Micro-Air Vehicles*) a bajos números de Reynolds. Así pues, en la presente tesis se presentan dos problemas de aplicación relacionados con la aerodinámica no estacionaria analizada desde el punto de vista de la formulación de Chang (1992), permitiendo entender la física ambos problemas desde una perspectiva novedosa. El primer problema se plantea como un ejemplo de aplicación de dicha formulación integrada numéricamente en el software OpenFOAM®, mientras que el segundo se trata un ejemplo de aplicación directamente relacionado con la aerodinámica de MAVs.

En primer lugar, en el Capítulo 2 se ha llevado a cabo una descripción general de la formulación anterior que posteriormente se ha adaptado a cada uno de los problemas que se estudian en los Capítulos 4 y 5. La principal contribución de este documento se basa en la novedosa discusión de los resultados desde el punto de vista de la descomposición de fuerzas mediante vórtices. Según Chang (1992), los coeficientes aerodinámicos pueden descomponerse en contribuciones de aceleración, rotacionales, volumétricas y superficiales. Al final de los citados Capítulos pueden encontrarse conclusiones desde el punto de vista de esta descomposición.

Por otra parte, en el Capítulo 3 puede encontrarse una breve descripción del paquete OpenFOAM® y el Método de los Volúmenes Finitos (FVM, del inglés *Finite Volume Method*). A título de ejemplo, el lector puede hacerse una idea de las posibilidades que ofrece este software a la vez que examina un fragmento del código utilizado para las simulaciones llevadas a cabo en esta tesis.

En el Capítulo 4, se ha analizado la estructura del flujo alrededor de un cilindro que gira y se traslada, con el objetivo de indentificar y cuantificar las estructuras que contribuyen a las fuerzas de sustentación y de resistencia. Se han considerado dos situaciones diferentes a $Re = 200$: un cilindro desplazándose a velocidad constante que empieza a girar hasta alcanzar una relación de giro adimensional α (i), y un cilindro inicialmente rotando en un fluido en reposo con una relación de giro α, que comienza a trasladarse hasta alcanzar una velocidad correspondiente a $Re = 200$ (ii). En ambos casos se han considerado las relaciones de giro $\alpha = 1$ y $\alpha = 3$. Para este análisis se ha utilizado una formulación que cuantifica la contribución de las diferentes estructuras de vórtices que envuelven al cuerpo a las fuerzas aerodinámicas (Chang, 1992). Se ha comprobado que, especialmente en el caso de la sustentación, la principal contribución proviene de los elementos de volumen. La formulación puede utilizarse sin modificación alguna para casos transitorios más complejos que (i) o (ii), pero los resultados serían cualitativamente muy parecidos dado que las velocidades de rotación y traslación aumentan monótonamente. De hecho, se presentan para diferentes valores del término de aceleración q, y se comprueba que no difieren significativamente unos de otros ya que los citados mecanismos que generan la sustentación o la resistencia son prácticamente los mismos.

En general, la principal contribución a la sustentación se genera, como se esperaba, mediante el desarrollo del vórtice superior que se encuentra en la zona frontal de la superficie del cilindro, donde se genera una zona de baja presión. Sin considerar la rotación del cilindro ($\alpha = 0$), esta contribución se compensa con el efecto contrario que produce el vórtice inferior que gira en sentido opuesto al superior, por lo que la sustentación media se anula cuando el flujo se desarrolla por completo y se alcanza el régimen periódico. La oscilación en la evolución temporal de la sustentación viene dada por el desprendimiento de vórtices.

Cuando el cilindro gira a un régimen moderado ($\alpha = 1$), todavía aparece una fuerza de sustentación que oscila cuando el flujo se ha desarrollado por completo, y que también se debe al desprendimiento de vórtices en el cilindro. Pero ahora el valor medio de la sustentación se vuelve positivo (para un cilindro girando en sentido horario) ya que la rotación del cilindro refuerza el vórtice superior –que gira en sentido horario–, mientras que el vórtice inferior –que gira en sentido contrario– se debilita y se desprende ligeramente del cilindro, por lo que los valores máximos y mínimos de la sustentación son positivos para $\alpha = 1$. Para una mayor velocidad de rotación ($\alpha = 3$), la región de vorticidad positiva que envuelve al cilindro durante su rotación (en sentido horario) es capaz de suprimir el desprendimiento de vórtices, por lo que la sustentación se hace constante cuando el flujo se ha desarrollado por completo. Además, en este caso la sustentación también es mayor ya que tanto el vórtice inferior, que permanece adherido, como el superior que gira en sentido contrario al anterior, son atrapados por la región de vorticidad que envuelve al cilindro, contribuyendo de manera positiva a la sustentación. Esta interacción también reduce drásticamente la resistencia debibo a las zonas de presión positiva que aparecen en la parte posterior del cilindro. La principal diferencia que se aprecia en la configuración (ii), en este caso con mayor grado de rotación ($\alpha = 3$), es que el flujo completamente desarrollado con mayor sustentación y menor resistencia, ambas de valor constante, se alcanza más rápidamente ya que la

capa de vorticidad positiva que envuelve al cilindro está presente cuando el cilindro comienza a trasladarse suprimiéndose el desprendimiento de vórtices inicial. Sin embargo, en esta configuración el efecto transitorio de la resistencia es significativamente mayor debido a la aceleración en la traslación del cilindro, la cual añade un término de resistencia adicional que refuerza la resistencia positiva que originan los elementos de volumen.

Además, es importante destacar que la formulación de fuerzas en términos de vorticidad que se ha utilizado en este trabajo puede extenderse directamente a flujos tridimensionales para mayores valores de α que los considerados en el presente estudio. Recientes investigaciones (ver A.1) han estudiado la estructura y estabilidad de este tipo flujos. Pero el estudio de flujos tridimensionales se encuentra fuera del alcance del presente trabajo ya que la formulación haría perder la simplicidad del flujo 2D alrededor de un cilindro que gira al tratar de entender el desarrollo de la sustentación y resistencia en términos de contribución de vórtices, que es el principal objetivo del Capítulo 4, y de la tesis. En el flujo 2D los potenciales auxiliares son simples funciones analíticas, y las contribuciones de los diferentes elementos fluidos a las fuerzas de sustentación y resistencia pueden analizarse de una manera mucho más directa.

Por otra parte, en el Capítulo 5, se han llevado a cabo simulaciones numéricas 2D de un flujo alrededor de un ala batiente de geometría elíptica para diferentes valores de ángulo de ataque medio α, amplitud y frecuencia del movimiento de batida, St_a y St_c; para un número de Reynolds dado ($Re = 500$) de interés en MAVs y en el vuelo con alas batientes. La descomposición de fuerzas mediante vórtices que se ha utilizado en este trabajo ofrece expresiones analíticas que permiten calcular las contribuciones del término de masa añadida a las fuerzas de sustentación y resistencia, para cualquier movimiento de batida del perfil elíptico, y para cualquier α. Este hecho permite una validación adicional del código numérico. Es más, la formulación de la fuerza en términos de vorticidad permite caracterizar la propulsión (o resistencia) y la sustentación que cualquier vórtice del flujo ejerce sobre el ala. Básicamente, se observa que la propulsión se genera principalmente por el LEV que se origina durante la fase inicial de cada semibatida y por el TEV que se desprende de la semibatida anterior cuando todavía se encuentra cerca del perfil. Por otra parte, la resistencia se genera principalmente por el TEV que nace en la fase inicial de cada semibatida y por el LEV que se ha desprendido en las semibatidas anteriores (ésto depende de la frecuencia y la amplitud, St_c y St_a) cuando la semibatida actual lo presiona con su movimiento. Utilizando estos mecanismos, se explican las configuraciones de máxima eficiencia en la propulsión en términos de estructuras de vórtices en el flujo y su interacción. Se ha comprobado que para el ala elíptica del estudio a $Re = 500$, la eficiencia máxima en la propulsión se alcanza para $St_a \simeq 0.2$ y $St_c \simeq 0.8$ con $\alpha = 0$. Esta configuración corresponde a un flujo periódico con la misma frecuencia que la de batida. Otro resultado interesante es que a medida que $|\alpha|$ aumenta ligeramente desde cero, la eficiencia de propulsión se vuelve aperiódica y su valor medio disminuye.

Por último, hay que mencionar que las diferentes magnitudes que intervienen en la formulación de Chang (1992) se han implementado en el entorno de OpenFOAM® para cada uno de los problemas aerodinámicos que se abordan en esta tesis, por lo que es

posible acceder al valor de cada contribución en cada instante de tiempo y, desde luego, a la evolución temporal completa.

A.3 TRABAJO FUTURO

Como se ha comentado anteriormente, la principal contribución de esta tesis es la utilización de la descomposición de la fuerza mediante vórtices de Chang (1992), integrada en el entorno de OpenFOAM®, para llevar a cabo estudios relacionados con problemas de cuerpos móviles a bajos números de Reynolds.

En primer lugar, se ha comprobado la validez de esta formulación para estudiar un problema basado en el Efecto Magnus en el Capítulo 4, donde se ha utilizado una malla estática y se ha impuesto una velocidad azimutal a la superficie del cilindro. Luego, para abordar el problema del Capítulo 5 se ha utilizado una malla deformable para poder ejecutar un movimiento sinusoidal puramente vertical, aunque este método deja de ser válido cuando se tienen en cuenta cinemáticas más complicadas, movimientos de mayor amplitud y múltiples cuerpos que se mueven. Esto daría lugar a importantes deformaciones y elevados coeficientes de asimetría en las celdillas de la malla, lo que podría afectar enormemente a la estabilidad y precisión de las simulaciones.

Por esta razón, se propone para el futuro el uso de métodos más versátiles tales como el Método del Contorno Inmerso (del inglés, *Immersed Boundary Method*, ver e.g. Peskin, 1972, Peskin, 2002, Uhlmann, 2005, Mittal and Iaccarino, 2005, Taira and Colonius, 2007 and Pinelli et al., 2010) para integrarlo junto con la formulación Chang (1992). Este método lo presentó por primera vez Peskin (1972) y, desde entonces, ha sufrido una gran cantidad de modificaciones y mejoras. En una malla base se superpone la malla superficial del objeto, que se tiene en cuenta mediante un término de fuerza ficticia que se introduce en las ecuaciones de Navier–Stokes.

El Método del Contorno Inmerso es un método *mesh-free* (libre de malla) que puede modelarse independientemente del tipo de método de discretización de las ecuaciones que se haya elegido (e.g., Método de los Volúmenes Finitos, de los Elementos Finitos, o de las Diferencias Finitas). Pero al igual que cualquier otro método, el Método del Contorno Immerso también tiene sus limitaciones. Una de ellas, se debe a la falta de precisión cuando los resultados que ofrece este método se comparan con los obtenidos con una malla conforme. Sin embargo, la limitación más importante recae en la violación de la condición de no deslizamiento sobre la superficie del cuerpo, como concluyen Breugem (2012) y Kempe and Fröhlich (2012). Para paliar esta limitación, estos autores proponen un bucle corrector adicional para converger el campo de velocidades antes de resolver la ecuación de Poisson para la presión cuando se resuelven las ecuaciones de Navier–Stokes en variables primitivas. Otra solución es la propuesta por Lechner and Kuhlmann (2011) basada en el trabajo de Taira and Colonius (2007). Todas estas propuestas pueden afectar la eficiencia del código dada la necesidad de converger las restricciones adicionales que incluyen.

Otra solución más eficiente cuando se utiliza el Método del Contorno Inmerso es su integración en las ecuaciones de Lattice Boltzmann. Estas ecuaciones también gobier-

nan el comportamiento de un flujo con la ventaja de que sus variables no se encuentran acopladas, siendo éste, además, un método de segundo orden (más información en Succi, 2001). Algunos de los trabajos más recientes que usan este enfoque y lo aplican a la aerodinámica de alas batientes son e.g., Rosis et al. (2014), Favier et al., 2014 y Suzuki et al. (2015).

Por último, después de mejorar la eficiencia y la precisión del Método del Contorno Inmerso, se sugiere también, como trabajo futuro, el estudio de problemas tridimensionales. De hecho, esta extrapolación es ya directa cuando se utiliza el método de la malla deformable, como en el Capítulo 5, para imponer el movimiento de objetos en la malla. Sin embargo, no se ha tenido en cuenta en la presente tesis por preferir abordar inicialmente problemas bidimensionales por razones de claridad en la identificación de estructuras al utilizar la formulación de Chang (1992), además de por razones de coste computacional. Por ello, el enfoque de Lattice Boltzmann sería el más recomendable por razones de eficiencia. A título de ejemplo, podrían estudiarse las contribuciones del vórtice que se desarrolla en la punta del ala a los coeficientes de sustentación y resistencia, así como su interacción con los vórtices generados en los bordes de entrada y de salida del perfil. También serían de interés otros problemas tridimensionales tales como la tridimensionalidad de los vórtices en un cilindro que gira, o incluso más simple: un flujo alrededor de un cuerpo dado; estudiados desde el punto de vista de la formulación de Chang (1992).

BIBLIOGRAPHY

Anderson, J. M., K. Streitlien, K. S. Barret, and M. S Triantafyllou (1998). "Oscillating foils of high propulsive efficiency." In: *Journal of Fluid Mechanics* 360, pp. 41–72.

Ansari, S. A., R. Zbikowski, and K. Knowles (2006). "Aerodynamic modelling of insect-like flapping flight for micro air vehicles." In: *Progress in Aerospace Sciences* 42, pp. 129–172.

Ansari, S. A., N. Phillips, G. Stabler, P. C. Wilkins, R. Zbikowski, and K. Knowles (2009). "Experimental investigation of some aspects of insect-like flapping flight aerodynamics for application to micro air vehicles." In: *Experiments in Fluids* 46, pp. 777–798.

Asraf, M. A., J. Young, and J. C. S. Lai (2012). "Oscillation frequency and amplitude effects on plunging airfoil propulsion and flow periodicity." In: *AIAA Journal* 50, pp. 2308–2324.

Azuma, A. (2006). *Biokinetics of Flying and Swimming.* AIAA, Washington.

Badr, H.M. and S.C.R. Dennis (1985). "Time-dependent viscous flow past an impulsively started rotating and translating circular cylinder." In: *Journal of Fluid Mechanics* 158, pp. 447–448.

Blondeaux, P., L. Guglielmini, and M. S. Triantafyllou (2005). "Chaotic flow generated by an oscillating foil." In: *AIAA Journal* 43, pp. 918–921.

Bos, F. M., B. W. van Oudheusden, and H. Bijl (2013). "Radial basis function based mesh deformation applied to simulation of flow around flapping wings." In: *Computer and Fluids* 79, pp. 167–177.

Bratt, J. B. (1950). *Flow patterns in the wake of an oscillating aerofoil.* Tech. rep. Technical Report R & M 2773, Aeronautical Research Council.

Breugem, W.-P. (2012). "A second-order accurate immersed boundary method for fully resolved simulations of particle-laden flows." In: *Journal of Computational Physics* 231, pp. 4469–4498.

Chang, C-C. and R.L. Chern (1991). "Vortex shedding from an impulsively started rotating and translating cylinder." In: *Journal of Fluid Mechanics* 223, pp. 265–298.

Chang, C.C. (1992). "Potential flow and forces for the incompressible viscous flow." In: *Proceedings of the Royal Society of London A: Mathematical, Physical and Engineering Sciences* 437, pp. 517–525.

Chen, Y.M., Y.R. Ou, and A.J. Pearlstein (1993). "Development of the wake behind a circular cylinder impulsively started into rotatory and rectilinear motion." In: *Journal of Fluid Mechanics* 253, pp. 449–484.

Chew, Y.T., M. Cheng, and S.C. Luo (1995). "A numerical study of the flow past a rotating circular cylinder using a hybrid vortex scheme." In: *Journal of Fluid Mechanics* 299, pp. 35–71.

Coutanceau, M. and C. Ménard (1985). "Influence of rotation on the near-wake development behind an impulsively started circular cylinder." In: *Journal of Fluid Mechanics* 158, pp. 399–446.

Dabiri, J. O. (2009). "Optimal vortex formation as a unifying principle in biological propulsion." In: *Annual Review of Fluid Mechanics* 41, pp. 17–33.

Dickinson, M. H. and K. G. Götz (1993). "Unsteady aerodynamics performance of model wings at low Reynolds numbers." In: *Journal of Experimental Biology* 174, pp. 45–64.

Dudley, R. (2000). *The Biomechanics of Insect Flight.* Ed. by Princeton University Press. Princeton.

El Akoury, R., M. Braza, R. Perrin, G. Harran, and Y. Hourau (2008). "The three-dimensional transition in the flow around a rotating cylinder." In: *Journal of Fluid Mechanics* 607, pp. 1–11.

Ellington, C. P. (1999). "The novel aerodynamics of insect flight: Application to micro-air vehicles." In: *Journal of Experimental Biology* 202, pp. 3439–3448.

Ellington, C. P., C. van den Berg, A. P. Willmott, and A. L. R. Thomas (1996). "Leading-edge vortices in insect flight." In: *Nature* 384, pp. 626–630.

Favier, J., A. Revell, and A. Pinelli (2014). "A Lattice Boltzmann–Immersed Boundary method to simulate the fluid interaction with moving and slender flexible objects." In: *Journal of Computational Physics* 261, pp. 141–161.

Ferziger, J. H. and M. Perić (2001). *Computational Methods for Fluid Dynamics.* Springer-Verlag, New York, NY.

Garrick, I. E. (1936). "Propulsion of a flapping and oscillating airfoil." In: *Technical Report TR 567, NACA.*

Guilmineau, E. and P. Queutey (2002). "A numerical simulation of vortex shedding from an oscillating circular cylinder." In: *Journal of Fluids and Structures* 16, pp. 773–794.

Hsieh, C.-T., C.-C. Kung, C. C. Chang, and C.-C. Chu (2010). "Unsteady aerodynamics of a dragonfly using a simple wing-wing model from the perspective of force decomposition." In: *Journal of Fluid Mechanics* 663, pp. 233–252.

Hsieh, C.T., C.C. Chang, and C.C. Chu (2009). "Revisiting the aerodynamics of hovering flight using simple models." In: *Journal of Fluid Mechanics* 623, pp. 121–148.

Hunt, J.C.R., A.A. Wray, and P. Moin (1998). *Eddies, Stream, and Convergence Zones in Turbulent Flows.* Technical Report CTR-S88 pp. 193-208. Center for Turbulence Research.

Inamuro, Takaji (2012). "Lattice Boltzmann methods for moving boundary flows." In: *Fluid Dynamics Research* 44.2.

Issa, R.I. (1985). "Solution of the implicitly discretized fluid flow equations by operator-splitting." In: *Journal of Computational Physics* 62, pp. 40–65.

Jasak, H. (1996). "Error Analysis and Estimation for the Finite Volume Method with Applications to Fluid Flows." PhD thesis. Imperial College of Science, Technology and Medicine.

Jasak, H., A. Jemcov, and Z. Tuković (2007). "OpenFOAM: A C++ Library for Complex Physics Simulations." In: *International Workshop on Coupled Methods in Numerical Dynamics*. (IUC). Dubrovnik, Croatia.

Jimémenez-González, J.I., E. Sanmiguel-Rojas, A. Sevilla, and C. Martínez-Bazán (2013). "Laminar flow past a spinning bullet-shaped body at moderate angular velocities." In: *Journal of Fluids and Structures* 43, pp. 200–219.

Jones, K. D. and M. F. Platzer (2009). "Design and development considerations for biologically inspired flapping-wing micro air vehicles." In: *Experiments in Fluids* 46, pp. 799–810.

Jones, K. D., C. M. Dohring, and M. F. Platzer (1996). "Wake structures behind plunging airfoils: A comparison of numerical and experimental results." In: *AIAA Paper 96-0078*.

Juretic, Franjo (2004). "Error Analysis Finite Volume CFD." PhD thesis. Imperial College of Science, Technology and Medicine.

Kang, S. and H. Choi (1999). "Laminar flow past a rotating circular cylinder." In: *Physics of Fluids* 11, pp. 3312–3321.

Kármán, T. Von and J. M. Burgers (1935). *General aerodynamic theory – Perfect fluids.* Ed. by edited by W.F. Durand. Springer, Berlin.

Kempe, T. and J. Fröhlich (2012). "An improved immersed boundary method with direct forcing for the simulation of particle laden flows." In: *Journal of Computational Physics* 231, pp. 3663–3684.

Koochesfahani, M. M. (1989). "Vortical patterns in the wake of an oscillating airfoil." In: *AIAA Journal* 27, pp. 1200–1205.

Lai, J. C. S. and M. F. Platzer (1999). "Jet characteristics of a plunging airfoil." In: *AIAA Journal* 37, pp. 1529–1537.

Lechner, C. and H. C. Kuhlmann (2011). "Direct numerical simulation of particles in a fluid interacting with a wall." In: *Proc. Appl. Math. Mech* 11, pp. 481–482.

Lee, J.J., C.T. Hsieh, C.C. Chang, and C.C. Chu (2012). "Vorticity forces on an impulsively started finite plate." In: *Journal of Fluid Mechanics* 694, pp. 464–492.

Lentink, D. and M. Gerritsma (2003). "Influence of airfoil shape on performance in insect flight." In: *AIAA Paper 2003-3447*.

Lewin, G. C. and H. Haj-Hariri (2003). "Modelling thrust generation of a two-dimensional heaving airfoil in a viscous flow." In: *Journal of Fluid Mechanics* 492, pp. 339–362.

UNIVERSIDAD
DE MÁLAGA

Lighthill, M. J. (1969). "Hydromechanics of aquatic animal propulsion." In: *Annual Review of Fluid Mechanics* 1, pp. 413–449.

Lighthill, M. J. (1970). "Aquatic animal propulsion of high hydromechanical efficiency." In: *Journal of Fluid Mechanics* 44, pp. 265–301.

Lighthill, M. J. (1975). *Mathematical Biofluiddynamics.* SIAM, Philadelphia.

Liu, H., C. P. Ellington, K. Kawachi, C. van den Berg, and A. P. Willmott (1998). "A computational fluid dynamic study of hawkmoth hovering." In: *Journal of Experimental Biology* 201, pp. 461–477.

Lua, K. B., T. T. Lim, K. S. Yeo, and G. Y. Oo (2007). "Wake-structure formation of a heaving two-dimensional elliptic airfoil." In: *AIAA Journal* 45, pp. 1571–1583.

Marić, T., J. Höpken, and K. Mooney (2014). *The OpenFOAM® Technology Primer.* sourceflux UG.

Martín-Alcántara, A., E. Sanmiguel-Rojas, C. Gutiérrez-Montes, and C. Martínez-Bazán (2014). "Drag reduction induced by the addition of a multi-cavity at the base of a bluff body." In: *Journal of Fluids and Structures* 48, pp. 347–361.

Martín-Alcántara, A., E. Sanmiguel-Rojas, and R. Fernandez-Feria (2015). "On the development of lift and drag in a rotating and translating cylinder." In: *Journal of Fluids and Structures* 54.1, pp. 868–885. ISSN: 1520-9202.

Maxworthy, T. (1979). "Experiments on the Weis-Foch mechanism of lift generation by insects in hovering flight. Part 1. Dynamics of the "fling"." In: *Journal of Fluid Mechanics* 93, pp. 47–63.

Maxworthy, T. (1981). "The fluid dynamics of insect flight." In: *Annual Review of Fluid Mechanics* 13, pp. 329–350.

Maxworthy, T. (2007). "The formation and maintenance of a leading-edge vortex during the forward motion of an animal wing." In: *Journal of Fluid Mechanics* 587, pp. 471–475.

Milne-Thomson, L. M. (1996). *Theoretical Hydrodynamics.* Dover, New York.

Minami, Keisuke, Kosuke Suzuki, and Takaji Inamuro (2014). "Free flight simulations of a dragonfly-like flapping wing-body model using the immersed boundary-lattice Boltzmann method." In: *Fluid Dynamics Research* 47.1.

Minotti, F. O. (2002). "Unsteady two-dimensional theory of a flapping wing." In: *Physical Review E: Statistical, Nonlinear, and Soft Matter Physics* 66, p. 051907.

Mittal, R. and G. Iaccarino (2005). "Immersed boundary methods." In: *Annual Review of Fluid Mechanics* 37, pp. 239–261.

Mittal, S and B. Kumar (2003). "Flow past a rotating cylinder." In: *Journal of Fluid Mechanics* 476, pp. 303–334.

Morse, P. M. and H. Feshbach (1953). *Methods of Theoretical Physics.* McGraw-Hill, New York.

Mueller, T. J. (2001). *Fixed and Flapping Wing Aerodynamics for Micro Air Vehicles Applications.* Ed. by AIAA. Reston.

Muñoz-Esparza, D. and E. Sanmiguel-Rojas (2011). "Numerical simulations of the laminar flow in pipes with wire coil inserts." In: *Computers & Fluids* 44, pp. 169–177.

OpenCFD (2014). *OpenFOAM: The Open Source CFD Toolbox. User Guide. Version 2.3.1.* OpenFOAM Foundation.

Padrino, J.C. and D.D. Joseph (2006). "Numerical study of the steady-state uniform flow past a rotating cylinder." In: *Journal of Fluid Mechanics* 557, pp. 191–223.

Peskin, C. S. (1972). "Flow patterns around heart valves: A numerical method." In: *Journal of Computational Physics* 10, pp. 252–271.

Peskin, C.S. (2002). "The immersed boundary method." In: *Acta Numerica*, pp. 479–517.

Pinelli, A., I.Z. Naqavi, U. Piomelli, and J. Favier (2010). "Immersed-boundary methods for general finite-difference and finite-volume Navier-Stokes solvers." In: *Journal of Computational Physics* 229, pp. 9073–9091.

Pines, D. J. and F. Bohorquez (2006). "Challenges facing future micro-air-vehicle development." In: *Journal of Aircraft* 43, pp. 290–305.

Pitt, C. W. and H. Babinsky (2013). "Lift and the leading-edge vortex." In: *Journal of Fluid Mechanics* 720, pp. 280–313.

Pralits, J.O., L. Brandt, and F. Gianetti (2010). "Instability and sensitivity of the flow around a rotating circular cylinder." In: *Journal of Fluid Mechanics* 650, pp. 513–536.

Pralits, J.O., F. Gianetti, and L. Brandt (2013). "Three-dimensional instability of the flow around a rotating circular cylinder." In: *Journal of Fluid Mechanics* 730, pp. 5–18.

Prandtl, L. (1926). *Application of the "Magnus Effect" to the Wind Propulsion of Ships.* Technical Report TM-367. NACA.

Radi, A., M.C. Thompson, A. Rao, K. Hourigan, and J. Sheridan (2013). "Experimental evidence of new three-dimensional modes in the wake of a rotating cylinder." In: *Journal of Fluid Mechanics* 734, pp. 567–594.

Rao, A., J. Leontini, M.C. Thompson, and K. Hourigan (2013a). "Three-dimensionality in the wake of a rapidly rotating cylinder in uniform flow." In: *Journal of Fluid Mechanics* 730, pp. 379–391.

Rao, A., J. Leontini, M.C. Thompson, and K. Hourigan (2013b). "Three-dimensionality in the wake of a rotating cylinder in a uniform flow." In: *Journal of Fluid Mechanics* 717, pp. 1–29.

Rao, A., A. Radi, J.S. Leontini, M.C. Thompson, J. Sheridan, and K. Hourigan (2015). "A review of rotating cylinder wake transitions." In: *Journal of Fluids and Structures* 53, pp. 2–14.

Roache, P. J. (1994). "Perspective: A method for uniform reporting of grid refinement studies." In: *Journal of Fluids Enginnering* 116, pp. 405–413.

Rosis, A. de (2015). "Ground-induced lift enhancement in a tandem of symmetric flapping wings: Lattice Boltzmann-immersed boundary simulations." In: *Computers and Structures* 153, pp. 230–238.

Rosis, A. de and E. Lévêque (2015). "Harmonic oscillations of a thin lamina in a quiescent viscous fluid: A numerical investigation within the framework of the lattice Boltzmann method." In: *Computers and Structures* 157, pp. 209–217.

Rosis, A. de, G. Falucci, S. Ubertini, and F. Ubertini (2014). "Aeroelastic study of flexible flapping wings by a coupled lattice Boltzmann-finite element approach with immersed boundary method." In: *Journal of Fluids and Structures* 49, pp. 516–533.

Saffman, P. G. (1992). *Vortex Dynamics.* Cambridge University Press.

Sane, S. P. (2003). "The aerodynamics of insect flight." In: *Journal of Experimental Biology* 206, pp. 4191–4208.

Sane, S. P. and M. H. Dickinson (2001). "The control of flight force by a flapping wing: Lift and drag production." In: *Journal of Experimental Biology* 204, pp. 2607–2626.

Sanmiguel-Rojas, E. and T. Mullin (2012). "Finite-amplitude solutions in the flow through a sudden expansion in a circular pipe." In: *Journal of Fluid Mechanics* 691, pp. 201–213.

Seifert, J. (2012). "A review of the Magnus effect in aeronautics." In: *Progress in Aerospace Sciences* 55, pp. 14–45.

Shyy, W. and H. Liu (2007). "Flapping wings and aerodynamic lift: The role of the leading-edge vortex." In: *AIA Journal* 45, pp. 2817–2819.

Shyy, W., H. Aono, C. K. Kang, and H. Liu (2013). *An Introduction to Flapping Wing Aerodynamics.* Ed. by Cambridge University Press. Cambridge.

Stojković, D., M.Breuer, and F. Durst (2002). "Effect of high rotation rates on the laminar flow around a circular cylinder." In: *Physics of Fluids* 14, pp. 3160–3178.

Stojković, D., P. Schön, M. Breuer, and F. Durst (2003). "On the new vortex shedding mode past a rotating circular cylinder." In: *Physics of Fluids* 15, pp. 1257–1260.

Streitlien, K., G. S. Triantafyllou, and M. S. Triantafyllou (1996). "Oscillating foils of high propulsive efficiency." In: *AIAA Journal* 34, pp. 2315–2319.

Stroustrup, Bjarne (2013). *The C++ Programming Language.* Addison-Wesley.

Succi, S. (2001). *The Lattice Boltzmann Equation for Fluid Dynamics and Beyond.* Clarendon, Oxford.

Suzuki, K., K. Minami, and T. Inamuro (2015). "Lift and thrust generation by a butterfly-like flapping wing-body model: immersed boundary–lattice Boltzmann simulation." In: *J. Fluid Mech.* 767, pp. 659–695.

Taira, K. and T. Colonius (2007). "The immersed boundary method: A projection approach." In: *Journal of Computational Physics* 225, pp. 2118–2137.

Taylor, G. K., R. L. Nudds, and A. L. R. Thomas (2003). "Flying and swimming animals cruise at a Strouhal number tuned for high power efficiency." In: *Nature* 425, pp. 707–711.

Theodorsen, T. (1935). *General theory of aerodynamic instability and the mechanism of flutter.* Technical Report TR 496. Technical Report TR 496, NACA.

Triantafyllou, G. S., M. S. Triantafyllou, and M. A. Grosenbaugh (1993). "Optimal thrust development in oscillating foils with application to fish propulsion." In: *Journal of Fluids and Structures* 7, pp. 205–224.

Triantafyllou, M. S., G. S. Triantafyllou, and R. Gopalkrishnan (1991). "Wake mechanics for thrust generation in oscillating foils." In: *Physics of Fluids A* 3, pp. 2835–2837.

Triantafyllou, M. S., G. S. Triantafyllou, and D. K. P. Yue (2000). "Hydrodynamics of fishlike swimming." In: *Annual Review of Fluid Mechanics* 32, pp. 33–53.

Uhlmann, M. (2005). "An immersed boundary method with direct forcing for the simulation of particulate flows." In: *Journal of Computational Physics* 209, pp. 448–476.

Wang, J. and D.D. Joseph (2006). "Boundary-layer analysis for the effects of viscosity on the irrotational flow induced by a rapidly rotating cylinder in a uniform stream." In: *Journal of Fluid Mechanics* 557, pp. 167–190.

Wang, Y., C. Shu, C.J. Teo, and J. Wu (2015). "An immersed boundary-lattice Boltzmann flux solver and its applications to fluid–structure interaction problems." In: *Journal of Fluids and Structures* 54, pp. 440–446.

Wang, Z. J. (2000). "Vortex shedding and frequency selection in flapping fight." In: *Journal of Fluid Mechanics* 410, pp. 323–341.

Wang, Z. J. (2005). "Dissecting insect fligth." In: *Annual Review of Fluid Mechanics* 37, pp. 183–210.

Wei, Z. and Z. C. Zheng (2014). "Mechanisms of wake deflection angle change behind heaving airfoil." In: *Journal of Fluids and Structures* 48, pp. 1–13.

Weller, H. G., G. Tabor, H. Jasak, and C. Fureby (1998). "A tensorial approach to computational continuum mechanics using object-oriented techniques." In: *Computers in Physics* 12, p. 620.

Wu, J. and C. Shu (2015). "A coupled immersed boundary–lattice Boltzmann method and its simulation for biomimetic problems." In: *Theoretical and Applied Mechanics Letters* 5, pp. 16–19.

Wu, T. Y. (1961). "Swimming of a waving plate." In: *Journal of Fluid Mechanics* 10, pp. 321–344.

Yih, C.S. (1977). *Fluid Mechanics.* Ed. by West River Press. Ann Arbor.

Young, J. and J. C. S. Lai (2007). "Mechanisms influencing the efficiency of oscillating airfoil propulsion." In: *AIAA Journal* 45, pp. 1695–1702.

Zheng, Z. C. and Z. Wei (2012). "Study of mechanisms and factors that influence the formation of vortical wake of a heaving airfoil." In: *Physics of Fluids* 24.103601.

DECLARACIÓN

Los profesores Dr. Ramón Fernández Feria y Dr. Enrique Sanmiguel Rojas, Catedrático de Universidad en el Dpto. de Ingeniería Mecánica, Térmica y de Fluidos de la Universidad de Málaga, y Profesor Titular de Universidad del Dpto. de Ingeniería Mecánica y Minera de la Universidad de Jaén, respectivamente.

INFORMAN:

Que el trabajo de investigación que se ha desarrollado durante la tesis doctoral de D. Antonio Martín Alcántara es original y las publicaciones que avalan esta tesis no han sido utilizadas en tesis anteriores.

Málaga, 2016

Dr. Ramón Fernández Feria

Dr. Enrique Sanmiguel Rojas

CURRICULUM VITÆ

PERSONAL INFORMATION

Antonio Martín Alcántara

Born in Córdoba, 20 September 1985

email	a.martin.alcantara@gmail.com
phone	+34 627 01 30 32

EDUCATION

PhD in Mechatronic Engineering

2013-2016   Universidad de Málaga

School: Escuela Técnica Superior de Ingenieros Industriales (ETSII).
Thesis: *Contribution to the study of the nonstationary arodynamic forces in problems of interest for Micro-Air Vehicles.*
Description: This thesis explores the low-Reynolds aerodynamics from the point of view of a vortex-force decomposition in order to identify the fluid elements (vortices) that contribute to drag or lift forces.
Advisors: Prof. Ramón FERNANDEZ-FERIA & Prof. Enrique SANMIGUEL-ROJAS.

PhD complementary education

2011-2012   Universidad de Córdoba-Málaga-Granada

GPA: 8.8/10 · *Itinerary of Vehicles Hydro-Aerodynamics* · School: Escuela Técnica Superior de Ingenieros Industriales (ETSII).
Description: Complementary education required to access the PhD program and related to the thesis topic.
Workload: 30 ECTS.

Master in Sustainability and energetic efficiency in buildings and industry

2010-2011   Universidad de Jaén

GPA: 1.93/4 · *Master thesis award* · School: Escuela Politécnica Superior de Jaén.
Thesis: *Drag control behind blunt bodies.*
Description: Research on the drag reduction by the addition of cavities in the rear part of a two-dimensional Ahmed Body immersed in a two-dimensional, incompressible and turbulent flow.
Workload: 60 ECTS.

Bachelor of Industrial Engineering in Electricity

2004/05-2009/10   Universidad de Córdoba

GPA: 1.68/4 · School: Escuela Politécnica Superior de Córdoba.
Thesis: *Prototype for the Córdoba water network sectorization.*
Description: Design of an automatic system able of measuring, acting and displaying the information related to several valves of the Córdoba water network in real time.
Workload: 235 ECTS.

GRANTS AND CONTRACTS

Research grant

02/2012-10/2012   Universidad de Jaén

Description: Grant Ref.: 2011/BA048.

Research grant

03/2014-07/2014   Universidad de Jaén

Description: Research grant in the Fluid Mechanics group TEP-235.

Research contract	*03/2013-03/2014*	Universidad de Jaén

Project title: Control de la estela turbulenta de cuerpos esbeltos.
Ref.: P10TEP-5702.
Main researcher: Enrique Sanmiguel Rojas.
Funding entity: Junta de Andalucía.
Amount > 100.000€

Research contract	*02/2015-08/2015*	Universidad de Málaga

Project title: Estudio de la interacción aerodinámica de alas batientes al modo de una libélula para su uso en microvehículos aéreos.
Ref.: DPI2013-40479-P.
Main researcher: Ramón Fernández Feria.
Funding entity: Ministerio de Economía y Competitividad.
Amount > 100.000€

RESEARCH STAYS

Animal Flight Laboratory	*08/2015-11/2015*	University of California, Berkeley

Supervisor: Robert Dudley.
Description: Short-term stay related to the animal flight aerodynamics.

PUBLICATIONS RELATED TO THE PHD THESIS

Phys. Fluids	*July 2015*	Vortex flow structures and interactions for the optimum thrust efficiency of a heaving airfoil at different mean angles of attack

Research on the characterization of the fluid elements contributing to thrust or drag in a flapping wing, and identification of the optimal propulsion locus.
Authors: A. Martín-Alcántara, R. Fernandez-Feria and E. Sanmiguel-Rojas.

J. Fluid. Struct.	*March 2015*	On the development of lift and drag in a rotating and translating cylinder

Research on the flow structures that contribute to drag and lift forces in a rotating cylinder.
Authors: A. Martín-Alcántara, E. Sanmiguel-Rojas and R. Fernandez-Feria.

OTHER PUBLICATIONS

Mech. Mach. Theory	*Nov. 2015*	Analytical approaches to oscillators with nonlinear springs in parallel and series connections

Authors: E. Sanmiguel-Rojas, M. Hidalgo Martínez, J.I. textscJiménez-González and A. Martín-Alcántara.

J. Fluid. Struct.	*July 2014*	Drag reduction induced by the addition of a multi-cavity at the base of a bluff body

Authors: A. Martín-Alcántara, E. Sanmiguel-Rojas, C. Gutiérrez-Montes and C. Martínez-Bazán.

Int. J. Numer. Methods in Biom. Eng.	*March 2014*	Effects of the ambient temperature on the airflow into a Caucasian nasal cavity

Authors: M.A. Burgos, E. Sanmiguel-Rojas, A. textscMartín-Alcántara and M. Hidalgo-Martínez.

CONFERENCE CONTRIBUTIONS

Workshop on Fluid Mechanics

Vortex flow structures and interactions for the optimum thrust efficiency of a heaving airfoil at different mean angles of attack

Authors: A. Martín-Alcántara, R. Fernandez-Feria and E. Sanmiguel-Rojas.
Involvement: Oral presentation.
Location: Jaén (SPAIN).
Date: July 2015.

HELIX 2015

Vortex flow structures and interactions for the optimum thrust efficiency of a heaving airfoil at different mean angles of attack.

Authors: A. Martín-Alcántara, R. Fernandez-Feria and E. Sanmiguel-Rojas.
Involvement: Oral presentation.
Location: Porquerolles (FRANCE).
Date: June-July 2015.

67th APS

On the development of lift and drag in a rotating and translating cylinder.

Authors: A. Martín-Alcántara, E. Sanmiguel-Rojas and R. Fernandez-Feria.
Involvement: Publication.
Location: San Francisco, CA (USA).
Date: Nov. 2014.

10th ERCOFTAC

Mechanism to reduce the drag based on a multi-cavity at the afterbody.

Authors: E. Sanmiguel-Rojas, C. Gutiérrez-Montes, A. Martín-Alcántara, J.I. Jiménez-González and C. Martínez-Bazán.
Involvement: Poster.
Location: Marbella (SPAIN).
Date: Sept. 2014.

66th APS

Drag reduction using a multi-cavity at the afterbody.

Authors: E. Sanmiguel-Rojas, A. Martín-Alcántara, C. Gutiérrez-Montes, C. Martínez-Bazán, M.A. Burgos and M. Hidalgo-Martínez.
Involvement: Oral presentation and publication.
Location: Pittsburgh, PA (USA).
Date: Nov. 2013.

OTHER INFORMATION

2015 · Attendance to an OpenFOAM® training

2014 · Assistant in the 10th ERCOFTAC conference.

Awards

2011 · Best Master thesis in the University of Jaén.

Languages

SPANISH · Mothertongue.

ENGLISH · Intermediate.

French · Intermediate.

Italian · Basic (simple words and phrases only)

Interests Guitar · Ukulele · Travelling · Sport

January 25, 2016